Titre: Title:	Study of ion bombardment characteristics in high frequency plasmas
Auteur: Author:	Oleg Vasilyevich Zabeida
Date:	2000
Type:	Mémoire ou thèse / Dissertation or Thesis
Référence: Citation:	Zabeida, O. V. (2000). Study of ion bombardment characteristics in high frequency plasmas [Ph.D. thesis, École Polytechnique de Montréal]. PolyPublie. https://publications.polymtl.ca/8885/

URL de PolyPublie: PolyPublie URL:	https://publications.polymtl.ca/8885/
Directeurs de recherche: Advisors:	Ludvik Martinu
Programme: Program:	Unspecified

UNIVERSITÉ DE MONTRÉAL

STUDY OF ION BOMBARDMENT CHARACTERISTICS IN HIGH FREQUENCY PLASMAS

OLEG VASILYEVICH ZABEIDA
DÉPARTEMENT DE GÉNIE PHYSIQUE ET DE GÉNIE DES MATÉRIAUX
ÉCOLE POLYTECHNIQUE DE MONTRÉAL

THÈSE PRÉSENTÉE EN VUE DE L'OBTENTION
DU DIPLÔME DE PHILOSOPHIÆ DOCTOR (Ph.D.)
(GÉNIE PHYSIQUE)
14 JANVIER 2000

UNIVERSITÉ DE MONTRÉAL

ÉCOLE POLYTECHNIQUE DE MONTRÉAL

Cette thèse intitulée:

STUDY OF ION BOMBARDMENT CHARACTERISTICS IN HIGH FREQUENCY PLASMAS

présentée par: ZABEIDA Oleg

en vue de l'obtention du diplôme de: Philosophiæ Doctor

a été dûment acceptée par le jury d'examen constitué de:

M. WERTHEIMER Michael R. , D.Sc.A., président

M. MARTINU Ludvik , Ph.D., membre et directeur de recherche

Mme. MARGOT Joëlle, D.Sc., membre

M. STANSFIELD Barry L., Ph.D., membre

"To arrive at an option concerning the condition of a plasma by readings of instruments is as difficult as trying to establish a diagnosis of an illness by an inspection of a patient. Whereas an ordinary gas responds to the questions of the "doctor" willingly, a plasma only groans like a dumb animal so that the plasma researcher should, perhaps, be compared to a veterinarian."

D. A. Frank-Kamenetskii

À mes chers parents
Моим дорогим родителям

REMERCIEMENTS

Je voudrais remercier de tout coeur mon directeur de recherche, le professeur Ludvik Martinu, pour son support scientifique et moral tout au long de ce projet. Je lui suis très reconnaissant pour son soutien constant et pour la confiance et la liberté qu'il a su m'accorder lors de la conduite de ces travaux.

J'exprime ma profonde gratitude au professeur Michael R. Wertheimer pour son intérêt à mon travail, son aide préciese et nos discussions enrichissantes. Je le remercie également pour avoir accepté de présider le jury de cette thèse.

Je remercie beaucoup les Dr. Joëlle Margot et Dr. Barry Stansfield pour avoir bien voulu accepter d'évaluer la qualité scientifique de ce travail malgré les contraintes de temps.

Je suis très reconnaissant envers Mme Jolanta Sapieha pour son aide précieuse dans la caractérisation des surfaces et pour le grand service qu'elle m'a rendu en m'initiant au travail expérimental dans la Laboratoire des Procédés Plasmas. Merci pour son grand coeur et son caractère toujours actif et bon vivant.

Je remercie vivement le Dr. Abdelbasset Hallil, avec qui j'ai fait une partie de ce projet pour son acharnement au travail et pour les discussions profondes des problèmes physiques rencontrés dans le cadre de ce travail.

Je tiens à remercier Dale Morton et toutes les gens de "Denton Vacuum, LLC" que j'ai rencontrés lors de mon séjour dans cette compagnie, pour leur réception gentille et chaleureuse.

Un grand merci à Gilles Jalbert pour son soutien technique super-professionnel et son aide si précieuse tout au long de ces années.

Je voudrais aussi remercier tous mes collègues de laboratoire qui ont créé une ambiance fort chaleureuse et amicale : Daniel Poitras, Argemiro da Silva, Alexandru Fozza, Grzegorz Czeremuszkin, Mohamed Latrèche, Jiri Cerny, Dan Dalacu, Sigrid Dahl, Vladimir Nikonov, Adam Bergeron. J'ai beaucoup appris parmi eux, leur aide multiple me fut indispensable.

Je remercie ma femme Inna pour son amour, sa patience illimitée et son support sans conditions.

RÉSUMÉ

L'industrie et la recherche modernes utilisent d'avantage des techniques faisant appel aux ions dans des instruments de précision comme dans des systèmes pour les procédés de microfabrication, de modification de surfaces, et de dépôt de couches minces. Les caractéristiques les plus importantes déterminant les mécanismes d'interaction des ions avec la surface sont l'énergie et le flux d'ions. Par conséquent, la connaissance des fonctions de distribution d'énergie des ions (IEDFs) et des flux ioniques est nécessaire pour le contrôle de procédés et pour le design des propriétés des matériaux.

Les objectifs principaux de ce travail sont de développer une méthodologie de mesure d'IEDF dans différents systèmes de plasma à basse pression, et d'appliquer cette méthodologie pour faire le diagnostic de procédés dans des réacteurs à plasma double-fréquence micro-onde / radio fréquence (MW/rf) et dans un réacteur de dépôt assisté par faisceau d'ions (IBAD). Les conditions étudiées sont celles généralement utilisées pour la déposition chimique en phase vapeur assistée par plasma (PECVD) et le traitement de surfaces de polymères pour l'amélioration de l'adhérence.

Deux techniques de mesure d'énergie d'ions ont été utilisées dans ce travail. La première est l'analyseur d'énergie d'ions à grilles multiples, développée dans notre laboratoire pour ce projet. La seconde utilise un instrument commercial, le système EQP – 1000 (de Hiden Analytique Ltée), qui combine un filtre d'énergie d'ions et un spectromètre de masse. Cette dernière technique permet des mesures résolues dans le temps et dans la masse des IEDFs des espèces ioniques qui arrivent à la surface. Ces évaluations concordaient avec des mesures complémentaires d'impédance de plasma.

Les caractéristiques énergétiques du bombardement ionique ont été mesurées dans les plasmas micro-onde (MW, 2,45 GHz), radiofréquence (rf, de 13,56 MHz) et double-fréquences en utilisant un intervalle de pression de gaz de 20 à 200 mTorr. Nous avons

plus particulièrement étudié les caractéristiques de deux types de décharge, soient : (i) la décharge MW pulsée, et (ii) la décharge à fréquence mixte MW-pulsée / rf-continue.

L'utilisation d'un plasma MW pulsé avec des fréquences d'impulsion variant entre 60 Hz et 10 kHz donne naissance à une IEDF bimodale, dans laquelle la valeur moyenne d'énergie des ions varie entre 2 et 10 eV. On montre que la variation du rapport cyclique ("time-on/(time-on+time-off)") affecte aussi bien la proportion du nombre d'ions d'énergie élevée dans l'IEDF que le flux total d'ions. L'évolution des IEDFs est analysée en termes d'un modèle global du plasma pulsé, employé pour déduire les constantes caractérisant le temps d'initiation et d'extinction du plasma. Cette analyse est basée sur l'hypothèse que les ions dans la partie des basses énergies de l'IEDF proviennent de la période d'extinction ("time-off") de la puissance, tel que suggéré par l'augmentation du pic correspondant à la diminution du rapport cyclique. Cette hypothèse est clairement confirmée par des mesures détaillées résolues dans le temps. La pulsation contrôlée permet ainsi d'ajuster sélectivement l'énergie des ions, et de ce fait les phénomènes surfaciques participant dans le traitement de matériaux, et principalement influencés par le bombardement ionique.

Dans le deuxième type de plasma pulsé étudié dans ce travail, la décharge pulsée MW a été jumelée avec une excitation rf continue. Nous avons constaté que la valeur absolue du potentiel d'auto-polarisation sur l'électrode rf ("rf-powered") est fortement modulée par la pulsation de la puissance MW appliquée: le potentiel est faible pendant les périodes d'impulsion MW ("time-on"), et il est élevé entre les impulsions. Cet effet s'explique par une variation de l'impédance du plasma, et de l'efficacité du couplage de la puissance rf au plasma. Par conséquent, l'énergie de bombardement des ions est également modulée. Les mesures résolues dans le temps indiquent qu'un pic intense dans la portion de basse énergie dans la distribution d'énergie des ions se produit pendant l'intervalle "time-on". Cette crête a la même structure que l'IEDF dans le plasma continu à double fréquence, pour une même tension d'auto-polarisation. Pendant la période de "time-off", des IEDFs larges et multi-pics, identiques à celles observées en plasma rf continu, ont été mesurées. De ces mesures, les IEDFs moyennes ont été

calculées. Cette méthodologie permet d'évaluer exactement toute l'énergie fournie par des effets de bombardement ionique à la surface de l'électrode rf. Cette énergie représente un paramètre important qui peut être utilisé pour la quantification des phénomènes induits par bombardement ionique, tels que la densification, la rupture de liens, etc.

Dans le système d'IBAD, les IEDFs ont été évaluées pour l'argon, l'oxygène, et l'azote, et ceci à trois angles différents de l'axe de la source des ions. Nous avons étudié l'évolution de l'énergie des ions et du flux moyen des ions en fonction des paramètres de la source (le courant et la tension de décharge). On a constaté que la source des ions du type cathode froide fournit à ces ions une large distribution d'énergie, avec une valeur moyenne correspondant à environ la moitié de la tension de décharge. La bonne uniformité du faisceau des ions en termes de leur flux et énergie a été confirmée.

La corrélation des caractéristiques du bombardement ionique avec les propriétés des matériaux modifiés est illustrée par deux exemples. Le premier est le traitement de polymères (polycarbonate, polytéréphtalate d'éthylène) dans un plasma pulsé de MW, et par le faisceau d'ions d'azote. De tels traitements ont généralement pour but une amélioration de l'adhérence. La structure chimique de la surface analysée par la spectroscopie des photoélectrons produits par rayons X (XPS), indique une forte corrélation entre l'enrichissement de la surface en azote et l'ouverture des anneaux de benzène, en fonction de l'énergie des ions contrôlée par le rapport cyclique de pulsation. Le deuxième exemple est le dépôt assisté par faisceau d'ions de films optiques tels que l'oxyde de titane et l'oxyde de tantale. La densité des couches, leurs indices de réfraction et leurs contraintes mécaniques ont été mesurés, et corrélés avec les conditions de bombardement ionique.

En conclusion, les contributions principales du travail actuel sont les suivantes: (i) un analyseur d'énergie d'ions à grilles multiples a été développé et entièrement caractérisé; (ii) une méthodologie de mesures a été proposée, et étudiée, qui permet de

déterminer quantitativement les énergies de bombardement ionique dans des décharges complexes telles que des plasmas MW/rf utilisés pour le traitement de matériaux; et (iii) une corrélation directe entre les IEDFs et les paramètres de décharge tels que l'épaisseur de la gaine, la densité de plasma, et les potentiels de surface a été démontrée, faisant de cette approche un outil valable pour le diagnostic non perturbateur du plasma.

ABSTRACT

Modern industry and research widely use ions as part of the techniques in precise analytical instruments as well as in powerful processing tools for microfabrication, surface modification, and thin film deposition. The most important characteristics determining the mechanisms of ion-surface interactions are the ion energy and ion flux. Therefore, the knowledge of ion energy distribution functions (IEDFs) and fluxes is necessary for the control of the processes and for the design of materials properties.

The main objectives of this work are to develop the methodology of IEDF measurements in different low-pressure plasma systems, and to apply it for the process diagnostics in a dual-mode microwave / radio frequency (MW/rf) plasma reactor and an ion beam assisted deposition (IBAD) reactor. The investigated conditions include those generally used for plasma enhanced chemical vapor deposition (PECVD) and surface treatment of polymers for improved adhesion.

Two measurement techniques of ion energy are described in this work. The first is the retarding field multi-grid ion energy analyzer, developed for this project in our laboratory. The second is a commercial plasma probe instrument (Hiden Analytical Ltd. EQP - 1000 system), consisting of a sector ion energy filter and a quadrupole mass spectrometer. The probe permitted detailed time- and mass- resolved IEDF measurements of the arriving ionic species. These evaluations were complemented by the plasma impedance measurements.

Ion bombardment characteristics of continuous wave (cw) microwave (MW, 2.45 GHz), radio frequency (rf, 13.56 MHz) and dual-mode microwave/radio frequency plasmas were measured in the range of gas pressures from 20 to 200 mTorr. Special attention was paid to the characterization of two types of power modulated (pulsed) plasmas; these are a *pulsed MW* discharge and a dual-mode *pulsed MW / cw-rf* discharge. In the first case, the plasma is excited by pulsed MW power with pulse frequency between 60 Hz and 10 kHz, that was found to give rise to a structured, strongly bi-modal

IEDFs in which the mean ion energy values vary between 2 and 10 eV. Varying the duty cycle is shown to change the proportion between the high and low energy parts in the IEDF, as well as the total ion flux. Evolution of the IEDFs is analyzed in terms of the pulsed plasma global model, used to derive the characteristic time constants of plasma ignition and plasma decay This analysis was based on an assumption that the ions in the low energy portion of the IEDF originate from the time period between the individual power pulses, since their relative contribution increases with decreasing the duty cycle. This hypothesis was clearly confirmed by detailed time-resolved measurements. Controlled pulsing thus allows one to selectively adjust the ion energy, and thereby such surface phenomena in materials processing which are primarily influenced by ion bombardment.

In the second type of pulsed plasma investigated in this work, namely the pulsed MW / cw-rf dual frequency discharge, we found that the absolute value of the self-bias potential on the rf-powered electrode is strongly modulated by the pulsing MW power: it is low during the time-on period of the MW pulse, and high between the individual pulses. This effect was explained as a result of changes in the plasma impedance and in the effectiveness of rf power coupling to the plasma. As a result, the ion bombardment energy is also modulated. Time-resolved measurements reveal an intense low-energy peak in the energy distribution of ions arriving during the time-on interval. This peak has the same structure as the IEDF in cw dual-frequency plasma with the same self-bias voltage. During the time-off period, broad multi-peak IEDFs, identical to those in cw-rf plasma, were measured. From these measurements, the time-averaged IEDFs were reconstructed. This methodology enables one to accurately evaluate the total energy delivered by the bombarding ions to the surface of the rf electrode. This energy represents a valuable parameter which can be used for the quantification of ion-induced phenomena such as densification, bond breakage etc.

In the IBAD system, the IEDFs for argon, oxygen, and nitrogen at three different angles from the ion source axis were evaluated. We studied the evolution of the mean ion

energy and ion flux as a function of the ion source drive current and the drive voltage. It was found that the cold cathode ion source provides ions with a broad energy distribution, with a value of the mean ion energy corresponding roughly to one half of the drive voltage. Good uniformity of the ion beam in terms of ion flux and energy was confirmed.

The correlation of ion bombardment characteristics with the properties of modified materials is illustrated by two examples. The first one is the treatment of polymers (polycarbonate, polyethylene terephthalate) in pulsed MW plasma, and by nitrogen ion beam. Such treatments are generally aimed at adhesion improvement. The surface chemical structure, analyzed by X-ray photoelectron spectroscopy, reveals a close correlation between the total nitrogen uptake and benzene ring opening, as a function of ion energy controlled by the duty cycle. The second example deals with the ion assisted deposition of optical films such as titanium oxide and tantalum oxide. Film density, refractive index and stress were found to correlate closely with the ion bombardment conditions.

In conclusion, the main contributions of the present work are the following: (i) a versatile multigrid ion energy analyzer has been developed and fully characterized; (ii) a methodology has been proposed and investigated which allows one to determine quantitatively the ion bombardment energies in complex discharges such as the MW/rf plasmas used for materials processing; and (iii) a close correlation between the IEDFs and the discharge parameters such as the sheath thickness, plasma density, and plasma and surface potentials has been demonstrated, thus making this approach a valuable tool for non-perturbing plasma diagnostics.

CONDENSÉ EN FRANÇAIS

Les ions sont les particules atomiques ou moléculaires possédant une charge électrique; ceci permet de contrôler leur énergie cinétique en utilisant les champs électriques d'accélération ou de ralentissement. Des ions avec des énergies allant de moins de 1 eV à des centaines de GeV sont employés dans la science et la technologie moderne pour étudier les interactions particule-particule et particule-matériau. Les ions agissant l'un sur l'autre peuvent produire les particules subatomiques, autrement indisponibles pour les physiciens, ainsi que des réactions nucléaires pouvant libérer d'immenses énergies, Ils peuvent être également utilisés pour la fabrication de nouveaux matériaux avec des propriétés spécifiques. En traitement de matériaux, l'utilisation des ions peut être divisée selon leur énergie, E_i, et l'application.

Les ions avec $E_i < 1$ keV agissent sur les atomes et les molécules de surface d'une façon complexe selon leur énergie et leur masse. Les principaux processus d'action selon les applications sont:

a) la pulvérisation des matériaux métalliques ou diélectriques appliquée au dépôt de couches minces;
b) la gravure réactive par les ions pour le transfert de motif menant à une forte anisotropie de la gravure;
c) les techniques de dépôt à l'aide d'ions comprenant la déposition chimique en phase vapeur assistée par plasma (PECVD), le dépôt assisté par faisceau d'ions (IBAD), le dépôt par un faisceau d'agglomérats ionisés, et d'autres méthodes de dépôt. Les ions transfèrent tout ou une partie de leur énergie cinétique aux films lors de leur naissance, produisant des couches denses et stables de haute qualité;
d) les (pré)traietments de surface tels que le nettoyage, la modification de la rugosité de surface et sa composition chimique avant le dépôt, principalement pour améliorer l'adhérence d'un film.

Les applications c) et d) sont liées aux activités principales de notre laboratoire de procédés plasmas (PPL). La compréhension et le contrôle des processus cités en c) et d) représentent la motivation principale du travail actuel. Des ions pour le traitement de matériaux sont produits par l'ionisation des atomes ou des molécules neutres dans les décharges de gaz. Deux types principaux de processus assistés par ions peuvent être distingués, soient l'utilisation d'un faisceau d'ions et l'exposition directe à l'environnement plasma.

Quand un faisceau d'ions est utilisé, les ions sont produits par une source éloignée, et ensuite accélérés et guidés vers la surface au moyen d'un système optique d'ions (habituellement, composé de grilles ou de diaphragmes métalliques). Les principaux paramètres du faisceau d'ions sont: E_i, le flux, ϕ_i, et la nature de l'espèce; tous peuvent être bien contrôlés, faisant des faisceaux d'ions un outil très attrayant. Les inconvénients sont le choix limité des ions (quelques gaz mènent à la dégradation du système optique d'ions ou bien ils oxydent la cathode), le flux ionique relativement bas, particulièrement quand E_i est basse, et les impuretés possibles à cause de la pulvérisation des composants du système optique d'ions. Dans le cas de l'exposition directe au plasma n'importe quel gaz réactif ou non-réactif peut être utilisé, et le flux d'ions est élevé. D'ailleurs, des objets en trois dimensions de forme complexe peuvent être uniformément traités. D'autre part, les paramètres de processus sont étroitement liés; leur commande indépendante (par exemple E_i, ϕ_i, ou flux d'espèces réactives) est habituellement limitée ou impossible. La surface du matériau est soumise aux effets synergiques des différentes espèces énergétiques du plasma, telles que les ions, les photons et les radicaux chimiquement actifs. Le niveau de contrôle du processus, la compréhension, et la prévisibilité ne sont pas aussi élevés que pour les techniques de faisceau d'ions. L'étude sur les énergies de bombardement d'ions est un des objectifs principaux du travail actuel. Le PECVD est une technique commerciale établie pour le dépôt de films tels que le nitrure de silicium et l'oxyde de silicium. L'utilisation de matériaux diélectriques en PECVD exige l'application de décharges de haute fréquence [fréquence radio (rf) ou micro-onde (MW)]. On sait que

dans les plasmas rf de couplage capacitif, une tension négative d'autopolarisation, V_b, se développe, ce qui nous permet d'obtenir une énergie élevée de bombardement ionique du substrat (E_i = 100 - 1000 eV). L'excitation MW est fréquemment utilisée comme source de plasma haute densité et très réactif avec le bombardement ionique modéré (E_i ~ 10 eV) Dans un plasma excité à une seule fréquence tous les paramètres sont étroitement associés. Par exemple, dans un réacteur de diode rf n'importe quelle augmentation de puissance rf mène à une valeur plus élevée de V_b, et E_i augmente; en même temps les changements de la densité du plasma, n_e, et de la température des électrons ont comme conséquence des valeurs plus élevées de ϕ_i, et de flux d'espèces réactives. Dans un tel réacteur le E_i et ϕ_i ne peuvent pas être découplés.

Une possibilité pour dépasser de telles limitations est une approche de fréquence mixte. Dans ce cas-ci, deux générateurs, MW et rf, sont simultanément utilisés pour soutenir le plasma. L'excitation MW est utilisée comme source principale de plasma actif, alors que n_e et ϕ_i sont contrôlés par la puissance micro-onde. L'excitation rf, appliquée au porte-échantillon , donne naissance à V_b qui contrôle E_i, mais n'affecte presque pas la densité du plasma. Une autre approche pour découpler E_i et ϕ_i est une pulsation de la source rf ou MW avec une fréquence d'impulsion dans l'intervalle de 10 Hz à 100 kHz. Il a été prouvé qu'une telle pulsation réduit la formation de particules de poussière et les dommages à la surface. Elle peut également mener à une augmentation de n_e et du taux de gravure. L'application d'un potentiel positif sur le substrat entre deux impulsions permet de tirer profit du bombardement par les ions négatifs habituellement confinés dans le volume du plasma. Les plasmas pulsés de MW et de MW/rf ont été utilisés dans notre laboratoire pour le dépôt des couches minces et pour le traitement des polymères. Cependant, l'effet des paramètres de pulsation tels que la fréquence d'impulsion et le rapport cyclique, D, sur les propriétés de plasma et de film n'a pas été systématiquement étudié. Le travail actuel devrait combler cette lacune. Comme on a montré, le bombardement ionique permet d'obtenir des films de haute qualité à des températures de substrat beaucoup plus basses que pour les techniques conventionnelles de PVD ou de

CVD. Grâce au bombardement ionique, les phases normalement obtenues à T élevée peuvent se produire à basse T, ce qui est nécessaire pour les films nanocomposites. La connaissance précise des caractéristiques des ions est importante pour expliquer et, probablement, pour prévoir les propriétés des films déposés. L'étude pour corréler les propriétés des films avec les caractéristiques de bombardement ionique a été effectuée expérimentalement et théoriquement pour des matériaux déposés par PVD. Pour pouvoir utiliser ces résultats dans les procédés plasmas, les caractéristiques de bombardement d'ions dans des décharges complexes doivent être bien connues.

Le PECVD et les traitements de surface par plasma ont été utilisés pendant de nombreuses années. Pendant une longue période les caractéristiques des films déposés ont été corrélées avec les paramètres externes tels que la puissance fournie par le générateur, le débit du gaz etc... Cependant, ces paramètres dépendent de la géométrie du réacteur, de la fréquence d'excitation, de la vitesse de pompage etc., et ils ne fournissent pas d'informations directes sur les caractéristiques du plasma telles que les flux et les énergies des particules impliquées (les particules neutres, les radicaux, les ions et les photons). Par conséquence, il est difficile de comparer les résultats obtenues dans des réacteurs différents.

Le travail que nous présentons est le premier dans ce laboratoire à se concentrer spécifiquement sur l'analyse des énergies de bombardement dans les plasmas à haute fréquence pour d'applications technologiques. Les objectifs du travail actuel peuvent être récapitulés comme suit: L'objectif principal est d'étudier le bombardement d'ions dans des systèmes de plasma à basse pression utilisés pour le PECVD et l'IBAD. Ceci inclut trois objectifs séparés:

Objectif 1: Développer une méthodologie de mesure d'énergie et de flux des ions, appropriée pour différents réacteurs plasma;

Objectif 2: Étudier l'effet des paramètres externes tels que la pression, la puissance, le mode d'excitation, et la pulsation sur les caractéristiques de bombardement ionique;

Objectif 3: Analyser l'effet des ions énergétiques sur les propriétés des surfaces traitées par plasma et des films déposés.

Les bases théoriques nécessaires pour comprendre les résultats sont présentées au Chapitre 3. La méthodologie expérimentale, ainsi qu'une description du système plasma à double fréquence, du système IBAD, de l'analyseur d'énergie multi-grille, du spectromètre de masse, de la sonde RF et de l'analyse de surface sont présentées au Chapitre 4. Le travail expérimental et la discussion sont basés sur plusieurs articles publiés ou soumis à des revues internationales. Ces articles sont inclus entièrement dans le texte aux Chapitres 5, 6 et 7. Les deux premières sections expérimentales traitent des mesures sur les distributions en énergie des ions à différents modes d'excitation du plasma, c'est à dire MW (Chapitre 5) ainsi que Rf et MW/Rf (Chapitre 6). Dans ces deux chapitres les régimes pulsés et continus sont étudiés. Des exemples de la corrélation entre les énergies des ions et les propriétés des polymères traités ou des films déposés sont présentés au Chapitre 7. Les expériences décrites dans cette étude ont été réalisées avec trois systèmes différents. Deux d'entre eux sont des réacteurs très similaires au niveau design, et ils fonctionnent en régime MW/rf. Ils ont été entièrement développés et construits dans notre laboratoire. Les résultats obtenus dans ces réacteurs sont décrits aux Chapitres 5 et 6. Le troisième système est un réacteur commercial IBAD équipé avec une source d'ions à faisceau large, fabriqué et installé par Denton Vacuum, LLC, Moorestown, NJ. Les résultats obtenus avec ce dernier système sont décrits au Chapitre 7.

Dans le cadre de ce projet nous avons développé et construit un analyseur d'énergie des ions (IEA) (fig. 4.5). Il se compose de trois grilles parallèles de nickel, et d'un cylindre de Faraday qui sert de collecteur. Les potentiels négatifs V_1 et V_3 sont appliqués à la première et à la troisième grille, afin de former les barrières respectives pour les électrons du plasma et pour les électrons secondaires. Un potentiel positif V_s est appliqué à la grille centrale, permettant seulement à des ions ayant une énergie plus grande que ZeV_s d'être collectés, où Ze est la charge d'ion. Une source de tension /

picoampèremètre, contrôlée par ordinateur (Keithley 487), a été utilisée pour mesurer le courant de collecteur I. La première dérivée de la courbe $I(V_s)$ donne la distribution d'énergie des ions sur la surface. Un exemple de courbe I-V typique et d'IEDF correspondante est montré sur la fig. 4.6. Puisque la mesure de l'IEDF peut être affectée par des collisions à l'intérieur de IEA, nous avons procédé à l'évaluation soignée de la distribution de pression dans la chambre d'IEA. Le système de Hiden EQP-1000 (fig. 4.12) est un outil avancé de diagnostic du plasma. Il est composé d'un analyseur d'énergie d'ions de haute transmission combiné avec un spectromètre de masse quadripolaire. Cet appareillage permet l'acquisition de spectres de masse à énergie fixe d'ions ont. De plus, on peut mesurer les distributions d'énergie des ions résolue en masse. Deux modes de base d'exécution sont disponibles pour le système EQP: le mode plasma et le mode RGA (de l'analyse résiduelle de gaz). En mode plasma les ions produits par le plasma entrent par un orifice de 50 micromètres de diamètre, situé dans le centre de l'électrode rf. En mode RGA les espèces neutres ainsi que les radicaux arrivant de la zone plasma, sont ionisées dans l'ioniseur par impact électronique, puis analysées par le quadrupôle.

L'instrument est contrôlé par un ordinateur utilisant le logiciel MASsoft de Hiden Analytical Ltée sous Microsoft Windows™, qiu permet le contrôle et la mise au point de l'instrument; elle est également utilisée pour l'acquisition de données et leur analyse.

Des mesures résolues en temps ont été effectuées en utilisant un circuit de synchronisation d'impulsion délivrant des signaux dont la largeur et le retard sont contrôlés par l'opérateur (figs. 4.13 et 4.2). Ce signal "trigger" ainsi produit est synchronisé avec le signal MW, permettant le déclenchement d'un compteur. Seuls les ions qui arrivent pendant l'impulsion de déclenchement sont comptés dans ce mode de mesures. Afin d'obtenir le rapport signal/bruit adéquat, un comptage cumulatif a été effectué pendant environ 200 impulsions MW.

Dans ce travail une sonde combinée de courant et tension rf (ENI), insérée entre le circuit d'accord et le réacteur (voir la fig. 4.2), a été utilisée pour des mesures détaillées de dissipation de puissance rf et d'impédance du plasma. Une fibre optique est utilisée

entre la section d'analyse et le convertisseur. Les valeurs du courant, de la tension et de la phase à la fréquence principale (13,56 MHz) ont été mesurées. La puissance rf dissipée et l'impédance complexe du réacteur ont été calculées en utilisant le logiciel "V/I probe". Les harmoniques possibles n'ont pas été pris en considération.

L'électrode rf dans le système de plasma a également servi comme porte-échantillon pour les expériences de traitement des surfaces de polymère. Les polymères ont été soumis soit à une décharge MW de haute densité, soit à un bombardement ionique intense dans une décharge rf, soit à une décharge combinée de type MW/rf. Des traitements supplémentaires ont été effectués dans le système de IBAD en utilisant la source d'ions de type cathode froide. Après le traitement les échantillons ont été exposés à l'atmosphère ambiante avant d'être caractérisés. La structure chimique de la surface des polymères tels que le polycarbonate (PC) et le polyéthylène-téréphtalate (PET) a été déterminée par la spectroscopie de photoélectrons produits par rayons X (XPS).

Le chapitre 5 est consacré à l'étude des ions énergétiques dans une décharge MW en mode continu ou en mode pulsé. L'analyse des ions a été effectuée utilisant différents gaz (Ar, N_2, et He), dans une gamme de pression variant de 50 à 200 mTorr. L'utilisation d'un plasma pulsé produit une IEDF bi-modale dans laquelle les valeurs moyennes d'énergie des ions varient entre 2 et 10 eV. Il se trouve que la fréquence d'impulsion (f_p) et le rapport cyclique (D) affectent fortement l'IEDF et le flux ionique. L'évolution de IEDF est analysée en termes de modèle global de plasma pulsé, afin de déduire les constantes caractéristiques de temps d'allumage et d'extinction du plasma. On montre que les ions dans la partie de basse énergie de l'IEDF proviennent de la période de temps entre les impulsions de puissance (T_{off}), et leur contribution relative augmente avec la diminution du rapport cyclique. Le contrôle de la durée de l'impulsion MW (T_{on}) et de celle de l'extinction de la décharge permet d'ajuster sélectivement l'énergie des ions, et de ce fait les phénomènes sur la surface pendant le traitement des matériaux qui sont principalement influencés par le bombardement ionique.

Nous avons constaté qu'un mode pulsé les IEDFs se composent de trois pics distincts: (i) un pic central, dû aux ions provenant de la période T_{on} ; (ii) un pic à énergie réduite, dûe aux ions arrivant pendant la période T_{off}; et (iii) une contribution plus faible dans la partie des grandes énergies, due aux ions produits pendant la courte période transitoire au début de chaque impulsion. Les intensités relatives de ces différents pics dépendent de D et f_p. Les résultats prouvent que l'énergie moyenne augmente avec l'augmentation de D, et que le flux ionique normalisé à la puissance moyenne, est plus grand pour le mode pulsé que pour le mode continu. On a observé un comportement semblable pour différents gaz, tel que Ar, N_2, et He. L'approche du modèle global a été employée pour analyser les IEDFs mesurées, à partir de la quelle nous avons obtenu les temps caractéristiques d'allumage (τ_1 = 330 μs) et d'extinction (τ_2 = 410 μs) du plasma, pour une décharge en argon à 100 mTorr. Le contrôle des paramètres de pulsation (f_p et D) peut être utilisé pour un réglage fin de l'énergie moyenne des ions arrivant sur la surface exposée à la dicharge. Un tel contrôle peut mener à une modification sélective de la structure de surface de polymère, par exemple, pour améliorer l'adhérence.

Dans le chapitre 6, nous présentons une analyse complète de bombardement ionique dans des scénarios complexes tel que le plasma MW/rf pulsé. Dans ce mode en particulier les mesures résolues en temps sont indispensables pour évaluer l'énergie des ions (section 6.2). Avant d'aborder ce thème, nous discutons dans un premier temps des mesures de plasma rf en comparaison avec d'autres travaux publiés que nous utiliserons pour la compréhension des processus fondamentaux dans le plasma MW/rf continu (section 6.1). L'énergie maximale des ions observée dans le plasma MW/rf n'est pas simplement eV_b+eV_p, telle qu'elle est habituellement considéré en rf, mais contient un terme supplémentaire, $\Delta E/2$ déterminé par Eq. 3.29; cette valeur non négligable est dûe à la gaine plus étroite dans le plasma à haute densité de MW/rf (Eq. 3.21). L'énergie maximum d'ion, E_{max}, peut alors être exprimée comme suit: $E_{max} = eV_b + eV_p + \Delta E/2$. À titre de comparaison, dans un plasma rf d'argon à p = 20 mTorr et V_b = - 150 V, l'énergie maximale est de 170 eV alors que dans les mêmes conditions dans un plasma MW/rf cette

énergie est de 270 eV. De la forme observée d'IEDF, c'est clair que le plasma de MW/rf n'est pas une superposition simple des composantes du MW et du rf pris séparément, mais comporte de nouvelles propriétés décrite ci-dessus, avec les énergies élevées de bombardement ionique. Puisque les ions de N^+ subissent moins de collisions dans la gaine que des ions de N_2^+, le IEDF de N^+ est enrichie à haut énergie. À partir de l'IEDF mesurée nous avons obtenu des valeurs de ϕ_i par l'intégration directe d'IEDFs et de valeurs $<E>$ à partir d'Eq. (5.3). Dans le plasma rf, les valeurs mesurées de ϕ_i diminuent également avec la pression. Contrairement au plasma de MW ce n'est pas dû au changement du n_s. En fait nous avons constaté que le n_s augmente avec p, en effet la zone d'ionisation devient localisée près de l'électrode de rf. Nous considérons qu'une telle augmentation ne peut pas être compensée par des changements seuls de kT_e, pour expliquer la diminution observée du ϕ_i. Ainsi, la diminution de ϕ_i ne signifie pas la réduction de flux des ions, mais elle représente la tendance des ions avec angle d'incidence normal. Puisque dans le MW et les plasmas de MW/rf la gaine est presque sans collisions, cet effet est moins important. Le paramètre $<E>$ diminue avec p pour toutes les excitations de plasma, comme représenté dans fig. 6.4(b). Dans les modes rf et MW/rf c'est dû à l'augmentation des collisions de la gaine aux valeurs élevées de p, comme il est montré par les IEDFs, qui sont riches en ions de faible énergie. Pour les valeurs semblables de p et de V_b, $<E>$ est beaucoup plus élevée dans MW/rf, en raison de la diminution de l'épaisseur de gaine, résultant en moins d'énergie perdue par les ions pendant leur passage.

Dans ce travail nous étudions aussi les IEDFs dans des décharges d'argon produites par une combinaison de la micro-onde (1-2 kHz) pulsée et de l'excitation rf continue. Nous prouvons que les IEDFs pour les décharges pulsées de MW sont structurées, avec différents motifs provenant de différentes périodes de l'impulsion. Dans la décharge du mode doble MW/rf, on observe la modulation significative de la tension d'auto-polarisation pendant le cycle d'impulsion de MW, que nous attribuons aux changements de l'impédance du plasma: Nous démontrons que dans le mode pulsé MW

/rf l'impédance du plasma est fortement résistive quand le MW est allumé, alors qu'elle est principalement capacitive pendant la durée entre deux impulsions. On observe des valeurs basses de tension d'auto-polarisation (Vb) dans le plasma MW/rf pendant T_{on}, alors que V_b augmente instantanément entre les impulsions (T_{off}). En utilisant l'évolution mesurée de V_b, combinée avec des mesures résolues en temps de différentes espèces ioniques, les IEDFs à l'électrode rf à chaque instant de l'impulsion de MW ont été obtenues. Cette approche est alors employée pour reconstruire l'IEDF totale dans le plasma pulsé MW/rf, afin d'obtenir toute l'énergie fournie par les ions. Les IEDFs possèdent un pic étroit, de faible énergie (quelques dizaines d'eVs) pendant l'impulsion de MW (T_{on}), et elles sont beaucoup plus larges (plusieurs centaines d'eVs), avec des pics multiples, pendant la période de T_{off}, comme dans le mode rf continu. Les IEDFs moyennes (intégrées dans le temps) ont été obtenues, qui permettent d'évaluer tous les effets de bombardement ionique sur la surface d'une électrode rf.

Dans le cas du système commercial d'IBAD, discuté au chapitre 7, nous évaluons à l'aide de l'analyseur à grille l'effet des caractéristiques dérivées d'énergie des ions sur les propriétés des surfaces de polymères traités ou sur les couches optiques déposée. Ce travail a été exécuté à Denton Vacuum, LLC, Moorestown, NJ, sur leur réacteur Integrity-29. La connaissance des IEDFs à différents régimes de fonctionnement de cette source des ions est importante pour déterminer son utilité pour différents procédés. C'était une occasion de tester notre méthodologie de mesures d'IEDFs dans un environnement complètement différent. Puisque dans le réacteur IBAD les ions sont fournis par une source éloignée, on s'attend à ce que l'effet du bombardement ionique soit séparé des effets du rayonnement UV et des radicaux, contrairement aux expositions directes dans le plasma. La section 7.1 donne une comparaison des résultats du traitement de polymères dans le plasma et dans le réacteur IBAD, alors que la section 7.2 décrit le dépôt des films optiques et la variation de leurs propriétés avec le bombardement ionique énergétique.

On avait constaté dans un plasma MW pulsé, que l'énergie moyenne d'ion augmante avec l'augmentation de D, et que cela contribue à une restructuration plus prononcée du polymère exposé, le flux ionique étant gardé constant. On a également observé des effets semblables de restructuration de surfaces quand les polymères ont été traités par un faisceau d'ion provenant d'un source d'ions de type cathode froide. Dans le travail actuel, l'énergie et le flux des ions sont évalués dans le contexte du dépôt assisté par les ions des films optiques et de la modification des surfaces de polymère pour l'amélioration de l'adhérence. Les fonctions de distribution d'énergie d'ion ont été mesurées dans différents gaz tels que O_2, Ar, et N_2. Les caractéristiques de faisceau des ions, comme l'énergie maximum, l'énergie moyenne, et le flux ionique, ont été corrélées avec les propriétés des couches de TaO_5 et de TiO_2 déposées par l'évaporation en faisceau d'électrons assistée par un faisceau d'ions d'oxygène. Ces différents matériaux ont été analysés par ellipsométrie spectroscopique, par spectrophotométrie, et par profilométrie. Leur comportement optique et mécanique, tel que l'indice de réfraction et les contraintes mécaniques, est corrélé avec l'évolution de la microstructure du film. Nous avons déterminé un paramètre de procèdes important, nommé l'énergie ionique par atome déposé, qui devrait être optimisé afin d'obtenir les propriétés désirées des films déposés.

En réponse aux objectifs de ce travail décrits ci-dessus les conclusions principales peuvent être récapitulées comme suit: Une méthodologie pour l'évaluation du bombardement énergétique des ions a été développée, qui convient pour différents systèmes de traitement par plasma. Deux instruments, l'analyseur d'énergie des ions de type multi-grilles et la sonde de plasma EQP-1000 de Hiden ont été appliqués pour l'analyse des fonctions de distribution d'énergie des ions dans les environnements plasmas complexes tels que, les décharges rf, MW et MW/rf dans les modes continus et pulsés. L'IEA a été construit et utilisé dans différents réacteurs plasmas comprenant le système IBAD. L'analyse détaillée des IEDFs, basée sur les mesures d'IEA, nous a permis de caractériser les décharges pulsées en utilisant une approche de modèle globale. Ces résultats ont été confirmés par l'évaluation d'IEDFs résolues en temps et en masse.

Nous avons systématiquement étudié l'effet des paramètres externes tels que la pression, la puissance, le mode d'excitation, et la pulsation sur les caractéristiques de bombardement ionique sous les conditions généralement utilisées pour le traitement de matériaux. L'attention principale a été donnée aux régimes double fréquences et pulsés. On a trouvé, en utilisant des mesures résolues en temps, que dans le plasma MW/rf pulsé les énergies des ions sont fortement affectées par la modulation de V_b. On a confirmé que le plasma MW/rf n'est pas une simple superposition des décharges rf et MW. Cet effet est très important pour produire la microstructure désirable de matériaux déposés ou traités. On a observé deux pics distincts dans l'IEDF provenant de plasmas MW pulsés. Nous avons associé le pic d'énergie élevée aux ions arrivant pendant la période T_{on}, alors que le pic à faible énergie était liée à l'intervalle d'extinction du cycle de l'impulsion. Nous avons prouvé que les paramètres de pulsation tels que le rapport cyclique et la fréquence d'impulsion dans le plasma MW peuvent être utilisés pour contrôler les caractéristiques de bombardement ionique. Des mesures de sonde rf ont été employées comme technique complémentaire pour caractériser l'impédance du plasma et la dissipation de puissance rf. Ces mesures nous ont permis d'expliquer l'effet de la modulation de V_b dans le plasma MW/rf pulsé, c'est à dire de démontrer son caractère capacitif pendant la période de T_{off}, et un caractère partiellement résistif quand l'impulsion de MW est allumée. Les conclusions au sujet de la densité de plasma et de l'épaisseur de la gaine obtenues à partir des mesures d'impédance plasma sont en bon accord avec les données produites a partir des IEDFs. Cette approche est une technique essentielle afin de déterminer les paramètres de bombardement ionique, par exemple l'énergie fournie par un atome déposé dans les expériences de croissance de films.

Les effets de bombardement ionique sur les propriétés des surfaces traitées et des films déposés ont été étudiés. Les mesures sémi-quantitatives préliminaires sur des polymères exposés directement à un plasma ou à un faisceau d'ions ont montré les effets de restructuration de surface semblables, comme l'ouverture de cycle de benzène et l'incorporation d'azote. On a constaté que dans le plasma MW pulsé les paramètres

d'impulsion tels que le rapport cyclique affectent le niveau de la réorganisation de la surface. Ceci a été corrélé avec l'énergie de bombardement ionique qui dans de telles expériences est comparable à l'énergie de liaison des molécules organiques.

Le bombardement ionique représente seulement une partie des procédés plasmas. Les autres caractéristiques importantes sont le flux et l'énergie des particules neutres, des radicaux et des photons. Ils sont tous des fonctions complexes de la composition du gaz, de la densité du plasma, de la distribution en énergie des électrons et d'autres paramètres. Vu l'interdépendance de tous ces paramètres, une étude profonde et multi-techniques est nécessaire. La spectrométrie de masse, les mesures par les sondes de Langmuir, la spectroscopie d'émission optique (y compris VUV), la fluorescence induite par laser, sont des techniques complémentaires à envisager.

Mentionnons que les résultats obtenus tout au long de cette étude seront des paramètres expérimentaux dans les études théoriques de la croissance de films, comme par exemple dans les simulations de la croissance de films de silice par la dynamique moléculaire.

CONTENTS

LIST OF FIGURES

LIST OF ABBREVIATIONS AND SYMBOLS

Abbreviations

ac - alternative current

CVD - chemical vapor deposition

dc - direct curent

ECR - electron cyclotron resonance

ERD - elastic recoil detection

IAD - ion assisted deposition

IBAD - ion beam assisted deposition

IC - integrated circuit

IEA - ion energy analyzer

IEDF - ion energy distribution function

MW - microwave

MW/rf - microwave / radio frequency (dual frequency)

PECVD - plasma enhanced chemical vapor deposition

PIXE - particle induced X-ray emission

PVD - physical vapor deposition

RBS - Rutherford backscattering

RIE - reactive ion etching

rf - radio frequency

SIMS - secondary ion mass spectroscopy

SNMS - secondary neutral mass spectroscopy

VLSI - very large scale integration

Latin letters

A - area

A_a - entrance orifice area

C - capacitance, gas conductance

D - duty cycle, diffusion coefficient

D_a - ambipolar diffusion coefficient

D_e - electron diffusion coefficient

D_f - (free) diffusion coefficient

D_i - ion diffusion coefficient

e - electron charge

E_i - ion energy

$<E_i>$ - mean ion energy

E_n - ion energy per arrived (metal) atom

E_p - ion energy per deposited particle

f_p - pulse frequency

$f(E)$ - energy distribution function

I - current, collector current

I_{cw} - saturated ion current

I_{max} - maximum ion current

I_s - substrate current

J - current density

J_0 - space-charge-limited curent density

J_i - ion current density

k - Boltzmann constant

K - coefficient

L - distance

m - electron mass

M_i - ion mass

n - density

n_e - electron density, plasma density

n_g - neutral gas density

n_{i+} - positive ion density

n_{i-} - negative ion density

n_s - plasma density at the sheath edge

p, p_0 - gas pressure

p_b - beam pressure

p_s - static pressure

P_{av} - average MW power (over a MW pulse cycle)

P_{on} - microwave power during the time-on

r_D - deposition rate

S - pumping speed

S_{eff} - effective pumping speed

s - sheath thickness

T - temperature

T_a - total transparency of the analyzer

T_{eff} - effective electron temperature

T_m - melting point temperature

T_{on} - time-on

T_{off} - time-off

T_p - pulse period

T_e - electron temperature

T_i - ion temperature

V - voltage

V_b - self-bias potential

V_f, V_{float} - floating potential

V_s - scanning potential

V_p - plasma potential

V_1, V_3 - potentials on the first and third grids of the IEA

$<V>$ - time-average sheath voltage

u_B - Bohm velocity

U_s - substrate voltage

Z - ion charge

Greek letters

α - degree of ionization

Γ - voltage reflection coefficient

ε_0 - dielectric constant

λ - mean free path

λ_i - ion mean free path

λ_D - Debye shielding length

ν - frequency (of excitation)

σ - cross section

τ_1 - plasma creation time constant

τ_2 - plasma decay time constant

Φ - particle flux

ϕ_i - ion flux

ϕ_n - flux of neutrals

ϕ_m - flux of condensing particles

ϕ_r - flux of (trapped) inert gas

ω - angular frequency

ω_e - electron plasma frequency

ω_i - ion plasma frequency

LIST OF TABLES

CHAPTER 1. Introduction

1.1. Categories of ions according to their energy

Ions are atomic or molecular particles possessing an electric charge; this allows one to control their kinetic energy by using accelerating or decelerating electric fields. Ions with energies in the range from less than 1 eV to hundreds of GeV are used in modern science and technology to study particle-particle and particle-material interactions. Interacting ions may produce subatomic particles, otherwise unavailable for physicists, nuclear reactions releasing immense energy, or they may be used for the fabrication of new materials with specific properties. In materials processing the use of ions can be divided in three large groups, depending on their energy, E_i, and application:

A) $E_i > 1$ MeV: Ions are used for compositional depth analysis of materials such as in elastic recoil detection (ERD), Rutherford backscattering (RBS), particle-induced X-ray emission (PIXE) and others[1-3]. In this case the penetration depth typically ranges from one to several micrometers depending on the material.

B) 1 keV$< E_i <$ 1 MeV: Ions are used for ion implantation and ion-beam mixing[4,5]. The most common application is implantation of dopants such as B, P and As in Si matrices for components used in VLSI technology[6]. Implantation depth usually ranges from 10 to 100 nm. Ions with energies less than 20 keV can also be applied for the analysis of surface composition by secondary ion (or neutral) mass spectrometry (SIMS or SNMS)[7,8].

C) $E_i <\sim$ 1 keV: Ions interact with the surface atoms and molecules in a complex way depending on their precise energy and nature. The principal application-driven processes are the following:

a) momentum transfer sputtering of metal or dielectric materials applied for thin film deposition[9];

b) reactive ion etching for pattern transfer leading to etch anisotropy[10];

c) ion assisted deposition techniques including plasma enhanced chemical vapor

deposition (PECVD)[11], ion beam assisted deposition (IBAD)[12], ion plating[13], ionized cluster beam deposition[14], and other energetic deposition methods. The impacting ions transfer all or part of their kinetic energy to the growing films, giving rise to high-quality dense and stable layers;

d) surface (pre)treatments such as cleaning, modification of the surface roughness and chemical composition prior to deposition, mainly aimed at enhanced film adhesion[15].

The applications c) and d) are related to the main activities in our Plasma Processing Laboratory (PPL)[15-17]. Understanding and control of the processes under c) and d) represents the main motivation of the present work.

Ions for materials processing are produced by ionization of neutral atoms or molecules in the gas discharges. Two main types of ion assisted processes can be distinguished, namely the use of an ion beam and a direct exposure to plasma environment.

When an ion beam is used, ions are generated in a remote ion source, then they are accelerated and guided toward the surface by means of ion optics[18]. Principal parameters of the ion beam are: E_i, the flux, ϕ_i, and the nature of the species; all of them can be well controlled, making ion beams a very attractive tool. Disadvantages are the limited choice of ions (some gases lead to malfunction of the ion optics or they oxidize the cathode), the relatively low ion flux, especially at low energies, and possible impurities as a result of sputtering of ion optics components (usually, they consist of metal grids or diaphragms).

In the case of direct plasma exposure any reactive and non-reactive gas may be used, and the ion flux is high. Moreover, 3-dimensional objects of complex shape can be uniformly treated[15]. On the other hand, the process parameters are tightly inter-linked; their independent control (e.g. E_i, ϕ_i, or flux of reactive species) is usually limited or impossible. The materials surface is subjected to synergetic effects of the simultaneous action of different energetic plasma species, such as ions, photons and chemically active radicals. The level of process control, understanding, and predictability is not as high as

for the ion beam techniques. Investigation of ion bombardment energies is one of the main objectives of the present work.

1.2. Surface phenomena induced by low-energy ions

Depending on the nature of the impinging ions, and their E_i and ϕ_i characteristics, the important effects on the surfaces include partial sputter removal of loosely bound surface material, sub-surface incorporation, and other forms of energy dissipation[16,19-21]. In thin film deposition, the impinging ions influence the film growth rate, its physical and microstructural properties such as density and void concentration, chemical composition, internal stress, hardness, refractive index, etc.

The E_i value is the most important parameter in the consideration of a single ion-surface interaction. As E_i becomes comparable with the various characteristic energies of the substrate, a variety of effects can be observed, as illustrated in Fig. 1.1. Chemical reactions may occur between the surface and an arriving ion (or atom) with a very low activation energy, while the ion has a finite residence time at the surface. Surface mobility of adatoms may be affected when the energy of impinging particles is less than 1 eV. Higher arrival energies may lead to removal of surface contaminants and atoms near the surface. Typical desorption energies are reported to be on the order of 1 to 10 eV[22]. Sputtering of the target material, an important effect in ion-assisted processing, takes place at $E_i > 10$ eV ; its yield rises rapidly up to an incident energy of a few hundreds of eV, and it has a maximum between 1 and 5 keV. During film deposition, the ions with $E_i \gtrsim 10$ eV produce knock-in effects, surface atom displacement, and ion mixing. When E_i exceeds 100 eV, ion incorporation rapidly increases due to trapping and implantation mechanisms[19] (see Fig.1.2).

The ϕ_i value is another important characteristic when the total effect of ion bombardment is considered. It determines the number of surface atoms involved in the interactions with ions, the total energy delivered by ions to the surface, and it controls

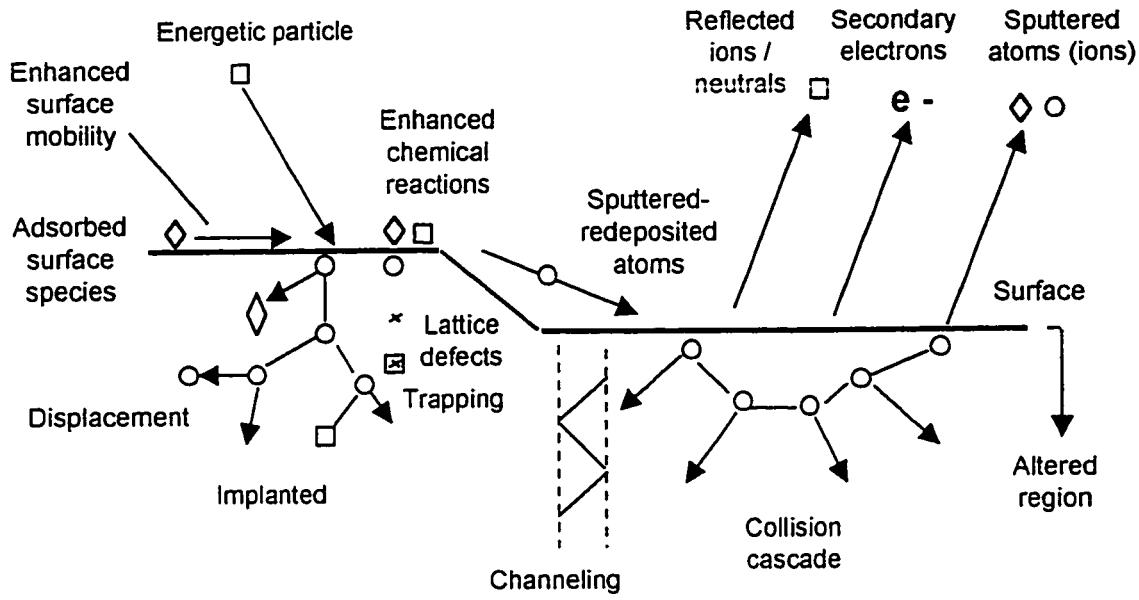

Figure 1.1. Schematic illustration of the energetic particle (ion or neutral) bombardment effects on surfaces and growing films. (After D. Mattox[13])

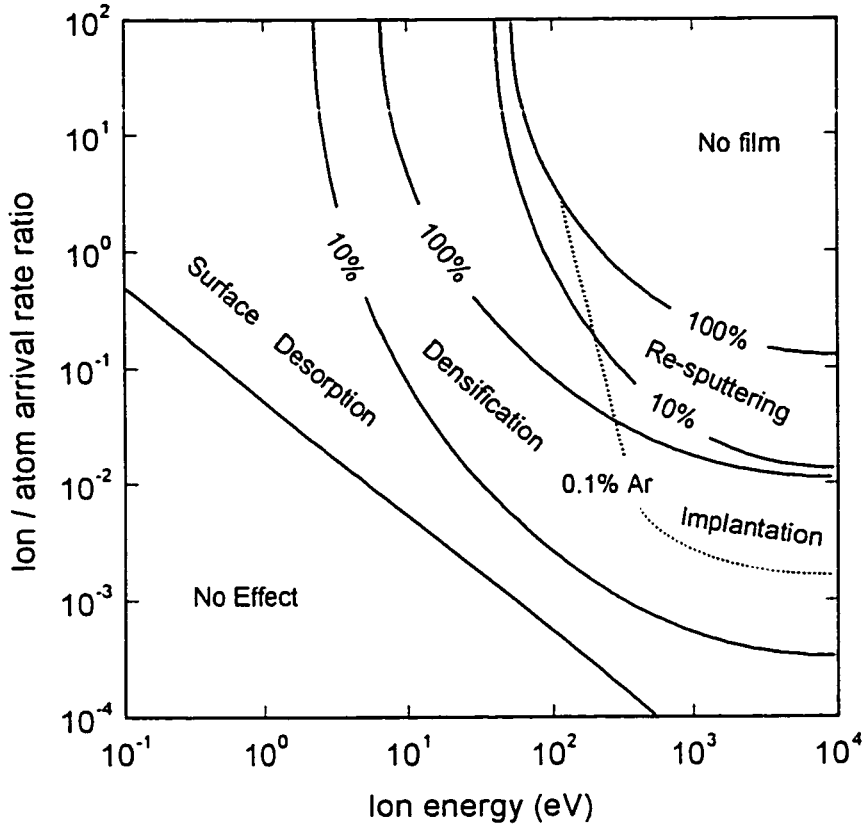

Figure 1.2 Schematic presentation of various ion bombardment processes shown as a function of relative ion flux and ion energy (After Ref.23, adapted from Ref. 20 for IAD of metals).

(together with E_i) the modification of surface or film properties. During film deposition the surface is continuously recreated by the flux of neutral atoms (molecules), ϕ_n. The ratio ϕ_i/ϕ_n is frequently used to characterize the deposition process[20,23]. Multiplying this ratio by the mean ion energy, $<E_i>$, one obtains the average ion energy per arrived atom, E_p. This parameter was employed, for example, by Kay and coworkers to characterize IBAD of Pd and Ag films[24,25]. Musil and Kadlec[26] related the deposition of TiN to E_p when using unbalanced magnetron sputtering. In a later paper[27], E_p was defined as the energy delivered to the growing film per deposited particle:

$$E_p = \frac{E_i\phi_i + E_n\phi_n}{\phi_m + \phi_r} \tag{1.1}$$

where E denotes the energy, ϕ the particle flux, and the indices i, m, n, and r indicate ions, neutrals, condensing precursor species and trapped inert gas, respectively. Modifying equation 1.1, E_p can be expressed by means of readily measured parameters, namely the substrate voltage, U_s, the substrate current, I_s, and the deposition rate, r_D:

$$E_p \approx E_i \frac{\phi_i}{\phi_m} \sim \frac{U_s I_s}{r_D}. \tag{1.2}$$

Other researchers have suggested that the above-mentioned approach is rather simplistic and that E_p cannot be considered a universal parameter[23,28-30]. For example, Ino et al.[29] showed that the physical properties and crystalline structure of sputter deposited Ta films depend on E_i and ϕ_i values in a manner which is contradictory to that predicted by E_p. Operating at the same value of E_p, a high flux of low energy ($E_i \approx 10$eV) Ar^+ ions was found to produce low resistivity bcc-Ta films, while a low flux of higher energy ($E_i \approx$ 30-60 eV) ions produced high resistivity β-Ta films. Therefore, E_i and ϕ_i should be considered separately when describing the processes responsible for microstructure of coatings. Independent control of E_i and ϕ_i is one of the main advantages of the dual-mode microwave/radio frequency plasma studied in this thesis.

1.3. Structure zone models

A frequently applied approach to describe the dependence of film microstructure on deposition parameters is the structure zone model introduced in the late 1960s by Movchan and Demchishin[31] for the case of PVD thick metal and oxide deposits. The model proposed that the film structure can be divided into three structural zones, each of which is characterized by the substrate temperature, T, and the film material melting point, T_m (Fig. 1.3a). Zone I ($T/T_m < 0.25$-0.3) contains tapered columns with domed tops which form due to low adatom mobility and shadowing effects. The second region, Zone II (0.25-$0.3 < T/T_m < 0.45$) comprises a region of smooth-topped granular structures controlled by surface diffusion. Zone III ($T/T_m > 0.45$) contains equiaxial crystallites possesing a polyhedral structure due to bulk diffusion. This simple zone model has been used for classifying the main structural features of evaporated films.

The above model has been extended to include sputtering conditions by Thornton[32], who added a third axis to accommodate variations in working gas pressure. The model of Thornton (Fig. 1.3b) shows schematically the interplay between the microstructure, the gas pressure, p, and T values. Thornton postulated the transitional Zone T between Zones 1 and 2. Zone T is characterized by densely packed fibrous grain structure, suitable for many applications.

In their extended model, Messier et al.[33] accounted for the evolutionary growth stages of structure development as well as the separate effect of thermal- and ion bombardment-induced mobility. They showed that the Zone 1-T boundary depends on U_s (Figure 1.3c) due to a specific contribution of ion bombardment to adatom mobility. This means that a densely packed microstructure usually obtained at high T values can be achieved at lower T values if sufficient ion bombardment is introduced. More recently, Kelly and Arnell[30] proposed a modified structure zone model while interpreting their results on closed-field unbalanced magnetron sputtering. They have shown that E_i and ϕ_i are the fundamental parameters in the ion-assisted PVD process, and the effects of E_i and

(a)

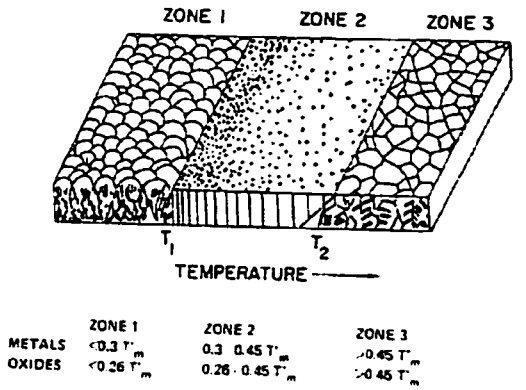

(b)

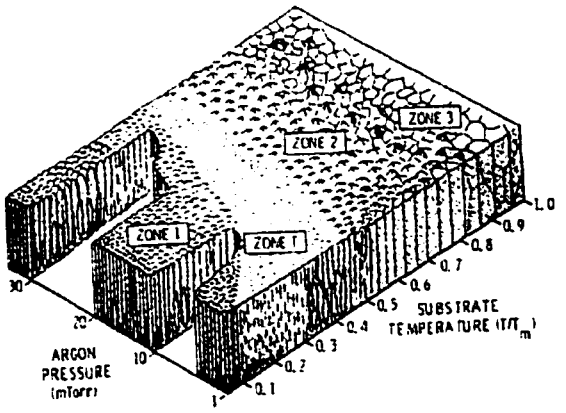

Figure 1.3 Structure zone models after different authors: (a)-Movchan and Demchshin;[31] (b) Thornton.[32]

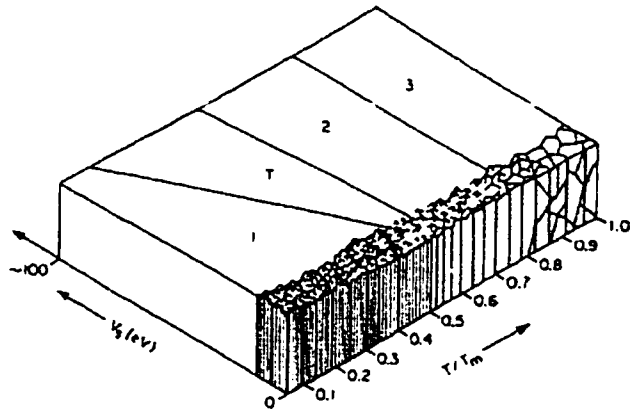

(c)

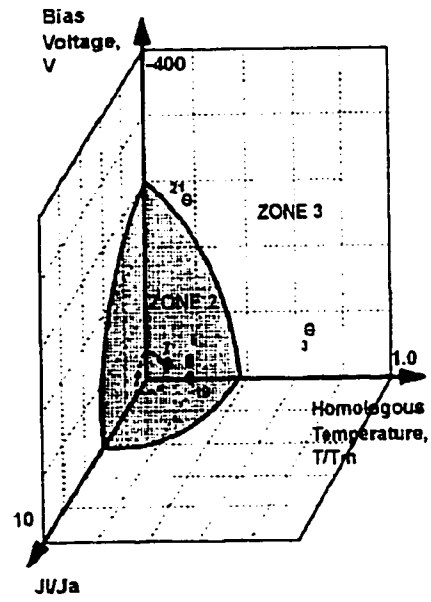

(d)

Figure 1.3 (continued) Structure zone models after different authors: (c) Messier, Giri, and Roy;[33] (d) Kelly and Arnell.[30]

ϕ_i must be considered separately when describing the detailed microstructure of coatings. As a result, a new dimension, namely the ratio ϕ_i / ϕ_n was added to the model (Figure 1.3d).

1.4. Ion bombardment in high frequency plasmas

PECVD is an established commercial technique for the deposition of insulating films such as silicon nitride and silicon dioxide[11]. The use of dielectric materials in PECVD requires application of high frequency [radio frequency (rf) or microwave (MW)] discharges. It is known that in capacitively coupled rf plasmas a negative self-bias voltage, V_b, develops, which allows one to obtain high ion energy bombardment (E_i = 100 - 1000 eV) of the substrate. MW excitation is frequently used as a source of high-density, very reactive plasma with moderate ion bombardment ($E_i \approx 10$ eV)[11,16].

In a plasma excited at a single frequency all parameters in Eq. 1.1 are tightly related. For example, in an rf diode reactor any increase of rf power leads to a higher V_b value, and E_i increases; at the same time the changes in plasma density, n_e, and in electron temperature result in higher values of ϕ_i and ϕ_n. In such a reactor the control of the E_p value is very limited, and E_i and ϕ_i cannot be decoupled. One possibility to override such limitations is the dual-frequency approach[34,35]. In this case two generators - MW and rf are simultaneously employed to sustain the plasma. The MW excitation is used as the main source of active plasma, while the n_e and ϕ_i are controlled by the MW power. The rf power, applied to the substrate holder, leads to the appearance of V_b, which controls E_i, but it almost does not affect the plasma density[36].

Another approach to decouple E_i and ϕ_i is pulsing of rf or MW power with a pulse frequency in the range from 10 Hz to 100 kHz. Such pulsing was proved effective to reduce dust particle formation[37] and surface damage[38]. It can also lead to an enhancement of n_e and r_D[39]. Positive biasing of the substrate between two pulses allows one to take advantage of bombardment by negative ions usually confined in the plasma volume[40]. Pulsed MW and MW/rf plasmas have been used in our laboratory for thin film deposition

and polymer treatment. However, the effect of pulsing parameters such as pulse frequency, f_p, and duty cycle, D, on the plasma and film properties has not been systematically studied. The present work should fill this gap.

Dual-frequency PECVD is being used in our laboratory for the deposition of different thin films including silicon dioxide, silicon nitride, titanium oxide, amorphous hydrogenated silicon and carbon (a-Si:H and a-C:H), and diamond-like carbon (DLC) for various applications such as protective, optical, and gas permeation barrier coatings[34,35,41-44]. It was shown that for each material at a fixed substrate temperature the specific critical values of mean ion energy $(\langle E_i \rangle)_C$ and $(\phi_r \phi_m)_C$ must be surpassed to obtain the dense films with desired mechanical and electrical properties[35]. This observation is in agreement with the structure zone models discussed above and the results of other authors[20,23,30,33]. In Fig. 1.4 the $(\langle E_i \rangle)_C$ and $(\phi_r \phi_m)_C$ values for three MW/rf PECVD materials[35] are plotted together with a schematic summary of various regimes in which similar mechanisms occur in different PVD (mostly IBAD) films[20,23]. Evidently, the boundary between individual regimes may vary for different materials and for different ions involved in the deposition. In this graph the optimum deposition regimes are near the "100% Densification" line, where dense, stable coatings are produced at high r_D (no significant resputtering occurs, see Fig. 1.2). It appears that PECVD data points for the critical values of ion bombardment are located in such an optimum region. For SiO_2 direct comparison with IBAD data[20] reveals a very good agreement for the E_i and ϕ_i/ϕ_m, values needed to obtain transparent, dense coatings. We see that, independently of the deposition technique (at the same T), the film quality is determined by ion bombardment parameters, making their control a very important issue.

As it was shown, the ion bombardment during the thin film deposition allows one to obtain high-quality coatings at much lower substrate temperatures than when conventional PVD or CVD techniques are used. Due to ion bombardment, high T phases may occur at low T, such as is necessary in nanocomposite films[45]. Precise knowledge of ion characteristics is important to explain and, possibly, to predict the results of the film

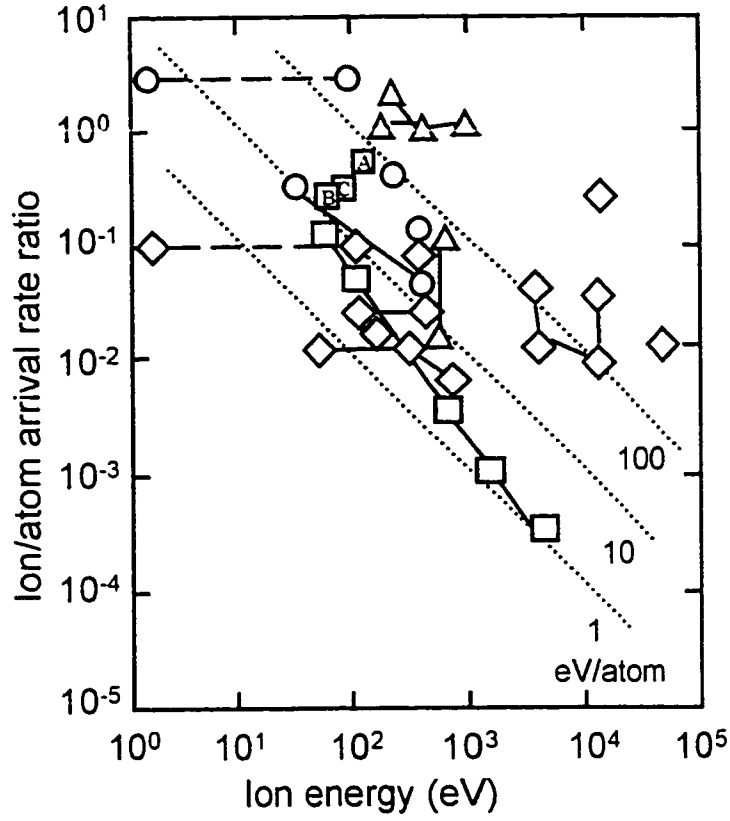

Figure 1.4 Plot of critical ion /condensing particle arrival ratios vs critical ion energy, required for film structural modification, particularly densification: A: $SiN_{1.3}$, B: SiO_2, and C: *a*-C:H obtained from MW/rf plasma.[35] Other data points are from Ref. 20 for different materials obtained by PVD techniques: circles - SiO_2, triangles - other dielectrics, diamonds-semiconductors, and squares - metals.

deposition process. Extensive work to correlate ion bombardment characteristics with surface or film properties was done both experimentally and theoretically for PVD materials[20,23,46,47]. In order to be able to use these previous results based on well-defined ion beams also in plasma processing, the ion bombardment characteristics in complex discharges must be known.

CHAPTER 2. Objectives and organization

2.1 Objectives

Plasma processing of materials such as PECVD and surface modification has been used for many decades. For a long period of time the deposited film or treated surface characteristics have been correlated with externally controlled parameters such as U_s, the power delivered from the generator, gas flow etc. However, the external parameters depend on the reactor geometry, excitation frequency, pumping speed etc., and they do not give any direct information about the internal process characteristics on the substrate surface such as the fluxes and energies of the involved particles (neutrals, radicals, ions and photons). As a result, it is difficult to compare such processes or scale them up. Major work in this direction has been accomplished in this laboratory since the MW/rf plasma has been first applied. The present project is the first one in this laboratory which specifically focuses on the analysis of ion bombardment energies in high frequency plasma in a technologically motivated context. At the same time, the approaches developed in this work intimately respond to the general driving forces described in Chapter 1.

The objectives of the present work can be summarized as follows:

The main objective is to investigate ion bombardment in low pressure plasma systems used for PECVD and IBAD. This includes three separate objectives:

Objective 1: To develop a methodology of ion energy and ion flux measurements, suitable for processing reactors;

Objective 2: To study the effect of external parameters such as pressure, power, excitation mode, and pulsing on the ion bombardment characteristics;

Objective 3: To analyze the effect of energetic ions on the properties of plasma treated surfaces and deposited films.

2.2 Thesis organization

The theoretical background needed to understand the discussed issues is presented in Chapter 3. Experimental methodology, including a description of the dual-frequency plasma system, IBAD system, multi-grid ion energy analyzer, plasma probe, rf probe, and surface analysis is presented in Chapter 4.

The experimental work and the discussion are based on several articles published or submitted to peer reviewed journals. These articles are included in the text in full in Chapters 5, 6, and 7. The first two experimental sections deal with the measurements of ion energy distributions in the different plasma excitation modes, namely the MW plasma (Chapter 5), and the rf and MW/rf plasma (Chapter 6). In both chapters the cw and pulsed regimes are investigated. Examples of a correlation between the ion energy characteristics and the properties of treated polymer surfaces or deposited thin films are presented in Chapter 7.

The experiments described in this work were performed in three different vacuum systems. Two of them are the dual mode MW/rf plasma reactors, very similar in design, assigned here as reactors I and II. These systems were developed, constructed and installed in our laboratory. The results obtained in these reactors are described in Chapters 5 and 6. The third system was a commercial ion plating reactor equipped with a broad beam ion source, fabricated by and installed at Denton Vacuum, LLC, Moorestown, NJ. The results obtained in the latter system are described in Chapter 7.

2.3 Publications and presentations by the candidate

Publications included in the present work:

1. O. Zabeida and L. Martinu, *Ion energy distributions in pulsed large area microwave plasma*, J. Appl. Phys. **85**(9), 6366-6372, (1999).
2. O. Zabeida, A. Hallil, M. R. Wertheimer, and L. Martinu, *Time-resolved measurements of ion energy distributions in dual-mode pulsed-microwave/radio frequency plasma*, submitted to J. Appl. Phys. in August 1999.
3. O. Zabeida, J. E. Klemberg-Sapieha, L. Martinu and D. Morton, *Effect of ion bombardment in polymer surface modification: comparison of pulsed high frequency plasma and ion beam*, in "Plasma deposition and treatment of polymers", Mat. Res. Soc. Symp. Proc. Vol. **544**, (Materials research Society, Warrendale, PA, 1999), pp. 233-238.
4. O. Zabeida, J. E. Klemberg-Sapieha, L. Martinu and D. Morton, *Ion bombardment characteristics during the growth of optical films using a cold cathode ion source*, 42nd Annual Technical Conference Proceedings (Society of Vacuum Coaters, Chicago), 267-272 (1999).

Other publications:

1. P. Reinke, O. Zabeida, B. Andreani, S. Bureau, and L. Martinu, *Ion energy distribution functions in microwave and radio frequency plasmas*, Proceedings of the 12th International Symposium on Plasma Chemistry, Vol. 1, Minneapolis, University of Minnesota, 499-504 (1995).
2. O. Zabeida, J. E. Klemberg-Sapieha, and L. Martinu, *Effect of pulse mode on the plasma characteristics and on the treatment of polymers*, 41st Annual Technical Conference Proceedings (Society of Vacuum Coaters, Boston), 336-341 (1998).
3. A. Hallil, O. Zabeida, J. E. Klemberg-Sapieha, M. R. Wertheimer, and L. Martinu, *Mass-resolved ion energy distributions in dual-mode microwave/radio frequency*

plasma, 42nd Annual Technical Conference Proceedings (Society of Vacuum Coaters, Chicago), (1999)

4. A. Hallil, O. Zabeida, M. R. Wertheimer, and L. Martinu , *Mass-resolved ion energy distributions in dual-mode microwave / radio frequency plasma*, prepared for J. Vac. Sci. Technol.

Presentations:

1. O. Zabeida, *Role of ions in plasma processing*, Canadian-German workshop on dielectrics, Jouvance, QC, 1996.
2. O. Zabeida and L. Martinu, *Ion bombardment energies in high frequency plasma for materials processing*, Gordon Research Conference "Plasma processing", New Hampton, NH, 1996.
3. O. Zabeida, J. E. Klemberg-Sapieha, and L. Martinu, *Ion bombardment energies in continuous and pulsed high frequency plasma for materials processing*, American Vacuum Society, San Jose, CA, 1997.
4. O. Zabeida and L. Martinu, *Ion bombardment characteristics of large area pulsed MW and MW/RF discharges*, Gordon Research Conference "Plasma processing", Tilton, NH, 1998.
5. O. Zabeida, J. E. Klemberg-Sapieha, and L. Martinu, *Characterization of ion bombardment in large area pulsed MW and MW/RF discharges*, American Vacuum Society, Upstate New York Chapter, Albany, NY, 1998.
6. O. Zabeida, A. Hallil, J. E. Klemberg-Sapieha, M. R. Wertheimer, and L. Martinu, *Ion energy distributions in pulsed microwave and dual-mode microwave/radio frequency plasmas*, 14th International Symposium on Plasma Chemistry, Prague, Czech Republic, 1999.

CHAPTER 3. Theoretical background

3.1 Plasma basics

This chapter summarizes the basic definitions and relationships necessary for the understanding of the experimental results and for the discussions presented in the subsequent sections.

3.1.1 Plasma definition

Plasma was identified as the *forth state of matter* by Sir William Crookes in 1879[48]. In this view, as one adds heat to matter starting at low temperatures, it starts out as a solid, melts to form a liquid, then vaporizes to become a gas. Finally, if still more heat is added, the temperature rises, and individual atoms break apart into electrons and positively charged ions, thus forming fourth state of matter. Often plasma is referred to also as *ionized gas*. According to Chen[49], *plasma is a quasineutral gas of charged and neutral particles which exhibits a collective behavior*. This collective behavior is possible due to the long-range Coulomb forces acting between charged particles; it means motions that depend not only on local conditions but on the state of the plasma in remote regions. The name "plasma" was introduced by the American chemist Irving Langmuir in 1928; it comes from Greek πλασμα, which means something molded or something that fills up. The terminology was derived from a belief that ions act like a rigid jelly through which the electrons are free to move[50], a concept that still describes adequately the bulk region of low-pressure plasmas studied in this work. The characteristic light radiating from plasmas of our interest led to the name "*glow discharge*". This radiation, especially in the ultraviolet region, is another important component of plasma.

3.1.2 Plasma density and degree of ionization

On average plasma is electrically neutral, because any charge imbalance would result in electric fields that would tend to move the charges in such a way as to eliminate

the imbalance. As a result, the density of electrons, n_e, and of negative ions, n_{i-} are balanced by the density of positive ions, n_{i+} :

$$n_e + \sum_i Z_i n_{i-} = \sum_i Z_i n_{i+}, \tag{3.1}$$

where Z_i is the charge of the corresponding ion. For most plasmas studied in this work (except for that in oxygen), n_{i-} is negligible, and positive ions are considered to be single-charged; then:

$$n_e = \sum_i n_{i+}. \tag{3.2}$$

The n_e value is also referred to as *plasma density*. The plasmas of interest here have electron densities in the range of $1\text{x}10^9$ to $1\text{x}10^{11}$ cm^{-3} (Ref. 36).

An important parameter of a plasma is the *degree of ionisation*, α, that represents the ratio of the ion density to the density of neutral gas molecules, n_g. The n_g value can be obtained from the known gas pressure, p, and gas temperature, T:

$$n_g \equiv p/kT, \tag{3.3}$$

where $k = 1.381\text{x}10^{-23}$ J/K is the Boltzmann constant. If we consider a gas in the reactor at a room temperature (300 K) and a minimum working pressure of 20 mTorr, the corresponding n_g value is $6\text{x}10^{14}$ cm^{-3}. Therefore, the degree of ionization in our plasma is less than $1\text{x}10^{11}/6\text{x}10^{14} = 1.7\text{x}10^{-4}$; such plasma is considered *weakly ionized*. Charged particles collide more frequently with neutrals than with other charged particles.

3.1.3 Electron and ion temperatures

It is known from the gas theory that the energy, E, of individual particles in a thermodynamic equilibrium obeys the Maxwell-Boltzmann distribution:

$$f(E) = 2n\sqrt{\frac{E}{\pi(kT)^3}}\exp\left(-\frac{E}{kT}\right), \tag{3.4}$$

where n is the particle density. The most probable kinetic energy, E_m, (energy at the maximum) is given as $kT/2$, and the mean energy, $\langle E \rangle$, is

$$\langle E \rangle \equiv \frac{\int Ef(E)dE}{\int f(E)dE} = \frac{1}{n}\int Ef(E)dE = \frac{3}{2}kT. \tag{3.5}$$

Thus, the temperature is a measure of the average energy of the particles. In weakly ionized plasmas the *f(E)* for electrons usually deviates from the Maxwellian distribution[51]. Nevertheless, the term electron temperature is frequently used for such discharges in the sense of an effective temperature, T_{eff}, defined as:

$$T_{eff} \equiv \frac{2}{3kn}\int_0^\infty Ef(E)dE. \tag{3.6}$$

The fact that collisions of electrons with ions are rare compared to collisions with neutral gas species leads to the existence of different energy distributions and hence different temperatures for electrons and ions. Electrons are easily heated (accelerated) by an external electric field, and their elastic collisions with much heavier neutrals are inefficient in the energy transfer. As a result their average energy is substantially higher than the energy of ions, which are rapidly thermalised in collisions with the same (or comparable) mass neutrals possessing essentially room temperature. This kind of plasma is called "cold" reflecting the fact that the heat capacity of the system is determined by the most abundant species - here, the neutral gas. The elevated electron temperature leads to the creation of chemically highly reactive environment; the level of molecular dissociation may be very high while the gas temperature remains low. Sometimes this situation is referred to as "high-temperature chemistry at low temperatures"[52].

If α rises to values higher than 0.01, the long-distance Coulomb interactions between electrons and ions start to outweigh the interactions of charged particles with neutrals[53]. The electron and ion energy distributions approach each other rapidly as α increases. Since the ions continue to transfer their kinetic energy to the neutrals, the overall gas temperature will also rise. These systems are called "hot" or thermal plasmas, and they are beyond the scope of this work.

In plasma physics it is customary to express temperature in electronvolt units (eV) rather than in the degree kelvin (K):

$$T(\text{eV}) = (e/k)T(\text{K}) = 11\,604\ T(\text{K}). \quad (3.7)$$

The electron temperature in our plasmas is about 2 eV, or 2.3×10^4 K; it corresponds to an average electron energy of 3 eV (Eq. 3.5).

3.1.4 Elastic and inelastic collisions

In elastic collisions the total kinetic energy of the system does not change and the particles remain in the same state as before the collision. In contrast, during the inelastic collisions part of the kinetic energy is used to change the internal energy of the colliding particles; this gives rise to the creation of new charged, excited and chemically active plasma species[54]. Different inelastic collision patterns are summarized in Table 3.1.

Table 3.1 Principal kinds of inelastic collisions in low-pressure plasmas.

$e + A \rightarrow A^+ + 2\,e$	Ionization
$e + A \rightarrow A^* + e$	Excitation
$e + AB \rightarrow e + A + B$	Dissociation
$e + AB \rightarrow 2\,e + A^+ + B$	Dissociative ionization
$e + AB \rightarrow A^- + B$	Dissociative attachment
$e + A^+ + B \rightarrow A + B$	Three-body recombination
$e + A^+ \rightarrow A + h\nu$	Radiative recombination
$A^+ + B \rightarrow A + B^+$	Charge exchange
$A^* + B \rightarrow A + B^+$	Penning ionization

Collisions are characterized by a *cross section*, σ, which has a dimension of area. For an inelastic collision to occur, a minimum energy, called *threshold energy*, is necessary. The *mean free path*, λ, determined as the average distance between two successive collisions can be expressed as:

$$\lambda = (\sigma n_g)^{-1} \quad (3.8)$$

Hence, it appears that λ is inversely proportional to the gas pressure.

3.1.5 Debye length

A fundamental characteristic of the behavior of plasma is its ability to shield out the applied electric potentials by the charge density rearrangement. This shielding is not absolute, but has a form of an exponential decay with a characteristic length, λ_D, named the *Debye length* or the Debye radius. Since the shielding is accomplished by more mobile electrons, λ_D does not depend on the characteristics of ions or neutrals[55]:

$$\lambda_D = \sqrt{\frac{\varepsilon_0 k T_e}{n_e e^2}}, \tag{3.9}$$

where ε_0 is the vacuum permittivity. Equation 3.9 predicts a Debye length of approximately 0.1 mm for plasma with T_e = 2 eV and $n_e = 10^{10}$ cm^{-3}.

Plasma frequency

Another parameter that describes the plasma shielding effect, but now in the time scale, is the *electron plasma frequency* (or simply plasma frequency), ω_e, defined as a characteristic angular frequency with which electrons oscillate between heavier, immobile ions when the electron population is perturbed:

$$\omega_e = \sqrt{\frac{e^2 n_e}{m\varepsilon_0}}. \tag{3.10}$$

where m is the electron mass. ω_e is critical to the propagation of electromagnetic radiation in plasmas. An electromagnetic wave with a frequency $\omega < \omega_e$ will be effectively shielded and reflected, while for $\omega > \omega_e$ it will propagate in the plasma due to electron inertia.

Analogically to ω_e , ion plasma frequency is defined as:

$$\omega_i = \sqrt{\frac{e^2 n_i}{M_i \varepsilon_0}}, \tag{3.11}$$

where M_i is the ion mass. ω_i does not describe any real oscillations in the absence of a strong magnetic field, but it is rather used to characterize the ability of ions to respond to

oscillations of the electric field. For an argon plasma with $n_e = 10^{10}$ cm^{-3} the values for $\omega_e/2\pi$ and $\omega_i/2\pi$ are 0.9 GHz and 3.3 MHz, respectively.

3.1.7 Ambipolar diffusion

As in ordinary fluids and neutral gases the diffusion flux, Φ, of electrons and ions in the absence of electromagnetic field is described by Fick's law:

$$\boldsymbol{\Phi} = - D_f \nabla n. \tag{3.12}$$

Here the bold symbols stand for the vectors and D_f is the diffusion coefficient given as[56]:

$$D_f = (1/3)\langle v\rangle \lambda, \tag{3.13}$$

where $\langle v\rangle$ is the mean velocity of a particle. In the presence of the electric field, E, however, the mobility, μ, of the particle must be taken into account:

$$\boldsymbol{\Phi} = \mu n \boldsymbol{E} - D_f \nabla n \tag{3.14}$$

In order to maintain plasma neutrality the fluxes of electrons and ions out of any region must be equal. Since the electrons are lighter and tend to flow out faster, an electric field must appear to maintain the local flux balance. As a result, both species diffuse at the same rate, characterized by the *ambipolar diffusion* coefficient, D_a:

$$D_a = \frac{\mu_i D_e + \mu_e D_i}{\mu_i + \mu_e} \approx D_i\left(1 + \frac{T_e}{T_i}\right) \tag{3.15}$$

For a weakly ionized plasma ($T_e >> T_i$) D_a greatly exceeds the ion free-diffusion rate.

Substituting Eq. (3.14) in the continuity equation ($dn/dt + \nabla\boldsymbol{\Phi} = G - L$, where G and L are the particle generation and loss terms) results in the diffusion equation. Solutions of such equation can be obtained for spatial variation in one dimension. If no source terms are introduced, this solution will decay in time. Fig. 3.1 shows a solution of the diffusion equation for a high-pressure approximation for a slab geometry of width l.

3.2 Plasma sheath and ion bombardment energy

3.2.1 Sheath definition

In the previous section we dealt with the properties of the plasma bulk, which is neutral (or quasi-neutral). However, this plasma is surrounded by walls or electrode surfaces, which "communicate" with the plasma bulk across a thin (usually 1-10 mm) positively charged layer, the *sheath*. This layer is always formed between the surface and the plasma in order to balance the flux of electrons and ions and, hence, to maintain the plasma neutrality. Since in unmagnetized plasma electrons are far more mobile than ions, plasma must be charged positively in order to retain the electrons and to accelerate the ions. The sheath electron density is greatly reduced compared to those in the bulk. As a result, the electron excitation of gas molecules in this region is almost absent; this leads to another name of this region, namely the "*dark space*". The volume of sheath may be very small, compared with the volume of plasma, but this region is very important for the subject of the present work since it controls the energy of ions arriving on the surface. As

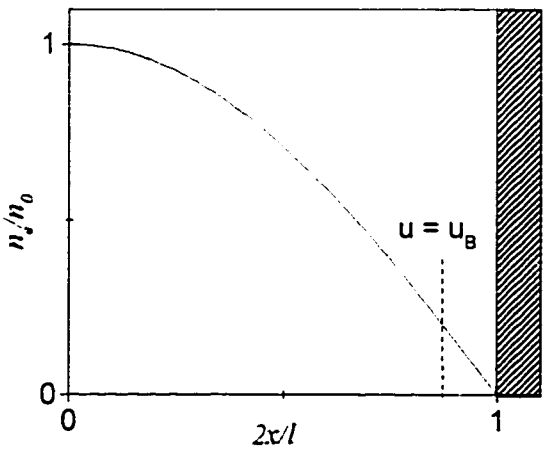

Figure 3.1 High pressure diffusion solution for normalized plasma density versus normalized position (After Ref. 55).

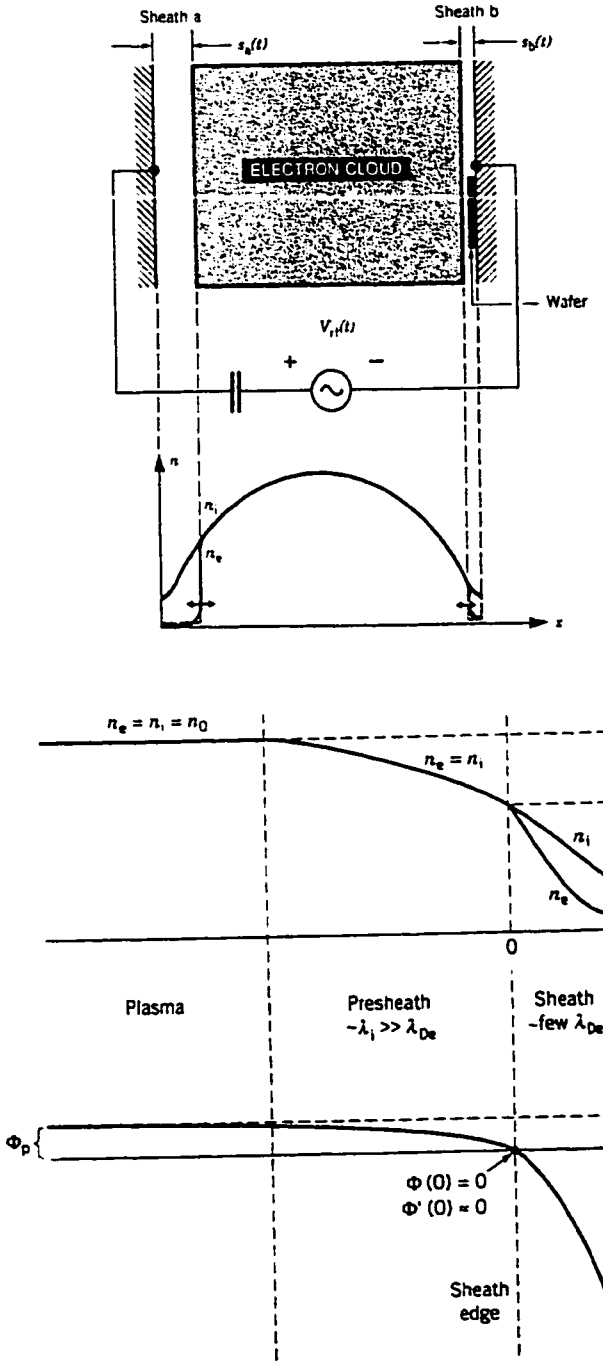

Figure 3.2 Physical model of an rf diode. Qualitative behavior of sheath and presheath in contact with a wall (FromRef.55).

it was mentioned, the bulk ions have an energy close to the thermal energy of the neutral gas, but they bombard the surface with energies hundreds and thousands times higher. They gain this energy in the sheath, hence their energy distributions almost completely depend on the properties of this relatively thin dark space.

3.2.2 Collisionless dc sheath and the Child-Langmuir law

Despite a fact that the discharges studied in this work are excited by the rf or MW power, the sheath characteristics in such discharges are the same or similar to those of a direct current (dc) discharge, described in this section. This is particularly true for the MW plasma, where $\omega > \omega_e >> \omega_i$ and neither electrons nor ions are able to follow the electric field oscillations, and they respond only to the created dc field. The sheath characteristics are stationary, and they obey dc sheath laws.

For simplicity we consider a planar electrode, an arrangement described by one-dimension geometry (Figure 3.2). We use the following assumptions: (1) Maxwellian electrons at temperature T_e; (2) cold ions ($T_i \approx 0$), and (3) $n_e = n_i$ at the plasma-sheath interface. The general sheath analysis (see for example Ref. 55) shows that a transition layer or *presheath* must exist between the neutral plasma and the nonneutral sheath in order to maintain the continuity of the ion flux. This gives rise to an ion velocity at the plasma-sheath edge, known as the Bohm velocity, u_B:

$$u_B = \sqrt{\frac{kT_e}{M_i}} \tag{3.16}$$

The value of u_B corresponds to the energy of an ion accelerated by a potential drop of $kT_e/2$ across the presheath. The plasma density, n_s, at the sheath-presheath edge is obtained from the Boltzmann relation:

$$n_s = n_e \exp\left(-\frac{kT_e/2}{kT_e}\right) \approx 0.61 \cdot n_e . \tag{3.17}$$

The current density, J, is assumed to be constant across the sheath, and it can be expressed as:

$$J = en_s u_B \approx 0.61 en_e (kT_e/M_i)^{1/2}. \quad (3.18)$$

The potential, V_f, of the floating electrode (i.e. the electrode with no net current) with respect to the sheath-presheath edge is:

$$V_f = -(kT_e/e)\ ln(M_i/2\pi m). \quad (3.19)$$

For argon the factor of proportionality between V_f and T_e in Eq. 3.19 is 4.7. Thus, argon ions with initial energy $kT_e/2$ at the sheath-presheath edge that fall through a collisionless dc sheath onto a floating wall would bombard the wall with an energy E_i (eV) $\approx 5.2T_e$ (eV). Equations 3.18 and 3.19 allow us to calculate T_e and n_e from the known (measured) ion flux and energy and vice versa. In argon, for example, the values of T_e = 2 eV and n_e = 10^{10} cm^{-3} lead to $E_i \approx 10$ eV and $J_- = J_+ \approx 200$ μA/cm^2. Numerical integration of Poisson's equation must be performed to find the sheath thickness, which has a value comparable to a few λ_D[55]. In the MW plasma (with no biasing) all wall sheaths are floating, and they can be described using Eqs. 3.18 and 3.19 [Ref. 53, p.33]

Let us now examine the case when the electrode is not floating, but it is negatively biased. If the difference of potentials between the plasma and the electrode, V_0, is much higher than $kT_e/2$, the current density at such electrode obeys the *Child-Langmuir law* (or simply Child law) of space-charge-limited current in a plane diode, J_0, can be expressed as:

$$J_0 = \frac{4}{9}\varepsilon_0 \left(\frac{2e}{M_i}\right)^{\frac{1}{2}} \frac{V_0^{\frac{3}{2}}}{s^2} \quad . \quad (3.20)$$

where s is the sheath thickness. Combination of Eqs. 3.18 and 3.20 allows one to calculate s:

$$s = \frac{\sqrt{2}}{3}\lambda_D \left(\frac{2eV_0}{kT_e}\right)^{\frac{3}{4}}. \quad (3.21)$$

For V_0 = 100 V, T_e = 2 eV, and $n_s = 0.6 \times 10^{10}$ cm^{-3}, Eq. 3.21 yelds $s \approx 14.9\lambda_D = 1.9$ mm; $s \approx 6.1$ mm if $n_e = 10^9$ cm^{-3}. Note the very weak dependence on electron temperature ($s \sim T_e^{-1/4}$).

All ions entering Child-Langmuir sheath gain the same energy eV_0, and they possess a narrow gaussian energy distribution with $dE \sim kT_e$ (developed in the presheath) when they strike the electrode.

3.2.3 Collisional sheath

When the mean free path for ion momentum transfer $\lambda_i < s$, the assumption of energy conservation, used to derive the Child law, fails. Two possible forms of the Child law are possible, depending on the assumptions discussed below[55]. The following equation:

$$J_0 = \frac{2}{3}\left(\frac{5}{3}\right)^{\frac{3}{2}} \varepsilon_0 \left(\frac{2e\lambda_i}{\pi M_i}\right)^{\frac{1}{2}} \frac{V_0^{\frac{3}{2}}}{s^{\frac{5}{2}}} \tag{3.22}$$

gives a collisional form of the Child law for the regime in which λ_i is independent of ion velocity. It can be considered true in argon and nitrogen[57] at pressures and with sheath voltages commonly used for plasma processing of materials.

Alternatively to Eq. 3.22, a higher pressure regime can be chosen, considering the ion mobility, μ_i, independent of velocity. In this case,

$$J_0 = \frac{9}{8}\varepsilon_0 \mu_i \frac{V_0^2}{s^3} \tag{3.23}$$

For the highly collisional case, the velocity at the sheath edge, u_s, is no longer equal to u_B, but it is given as[58]:

$$u_s \approx \frac{u_B}{\sqrt{1 + \frac{\pi\lambda_D}{2\lambda_i}}} \tag{3.24}$$

In all cases ionization and recombination in the sheath are considered negligible allowing to put $en_s u_s = J_0$. For T_e = 2eV and n_s =0.61x10^{10} cm^{-3}, Eq. 3.24 yields $u_s \approx 0.81 u_B$. This means that there is a 20% reduction of ion current to the electrode compared with the collisionless case (Fig. 3.3).

Values of s, resulting from different models for the sheath voltage drop of V_0 = 100 V, are compared in the Table 3.2. The following parameters were used in the calculations: T = 300 K, T_e = 2 eV, and $\sigma \approx 10^{-14}$ cm^2 (Ref. 57). To obtain the ion mobility we use the drift velocity values for the Ar^+ ion in argon gas[57] (see Appendix A). Note the very weak dependence of s values on T_e (due to the changes in λ_D; see Eq. 3.24) for collisional and highly collisional sheaths. To calculate n_e in the bulk corresponding to the chosen n_s value additional assumptions about electron collisions and ionization in the presheath must be made[59].

Table 3.2 Comparison of sheath thickness obtained by different models.

n_s 10^9cm^{-3}	λ_D mm	p mTorr	n_g 10^{15}cm^{-3}	λ_i mm	J_o μA/cm^2	μ_i m^2/Vs	$s_{C\text{-}L}$ mm (Eq. 3.20)	s_{col} mm (Eq. 3.22)	$s_{hi\text{-}col}$ mm (Eq. 3.23)
6.1	0.13	20	0.64	1.5	190	0.45	1.9	3.4	2.9
6.1	0.13	100	3.22	0.3	160	0.15	1.9	2.0	2.1
0.61	0.43	20	0.64	1.5	16.6	0.65	6.1	6.6	7.3
0.61	0.43	100	3.22	0.3	11.1	0.25	6.1	5.7	6.1

From the comparison of λ_i with s values, the case in the first line of Table 3.2 may be considered as collisionless, the last line as highly collisional, with two intermediate cases in-between. For all types of sheath the three approaches give similar s values. A difference appears at higher V_0 values where ions undergo several tens of collisions during their passage (see Fig. 3.4 and 3.5).

Since ions loose part of their energy in each elastic collision, the collisional sheath produces on average less energetic ions, compared with the collisionless one. The mean ion energy depends on the λ_i /s ratio; for λ_i /s <<1, it corresponds to the drift velocity.

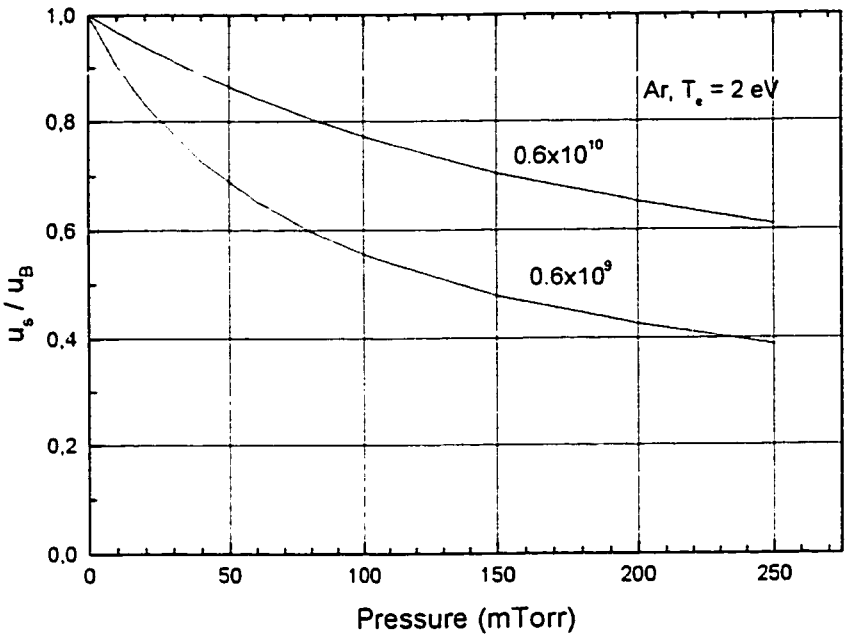

Figure 3.3 Reduction of the velocity of ions entering the sheath as a function of gas pressure for two values of plasma density at the sheath-presheath interface.

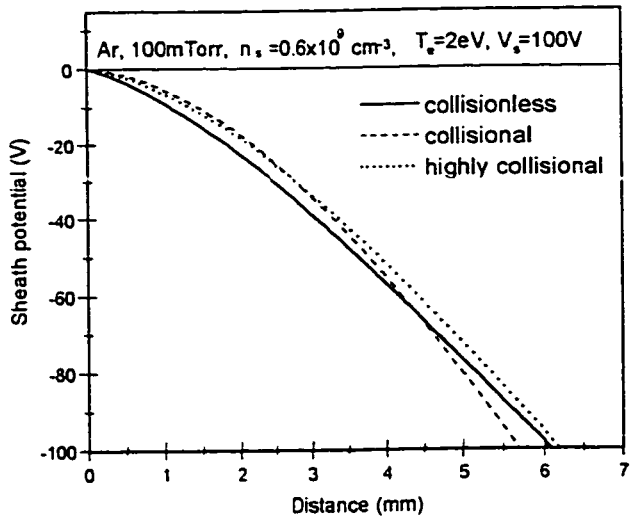

Figure 3.4 Potential distributions in the sheath calculated for three different models (Form the Eqs. 3.20, 3.22 and 3.23, $J_0 = en_s u_s$, s and V_0 was replaced by x and $V(x)$ respectively).

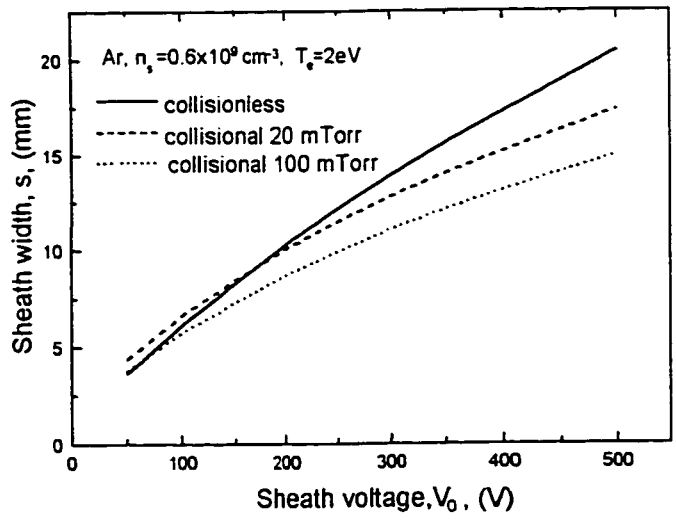

Figure3.5 Sheath width as a function of sheath voltage.

Momentum transfer and, especially, charge transfer collisions produce also fast neutrals, which may be responsible for an essential part of the bombardment energy[55,60].

3.3 Sheath in the radio frequency discharge

3.3.1 Capacitive rf discharge and potential distribution

One of the most widely used types of low-pressure discharges is sustained by radio-frequency currents and voltages, introduced through a capacitive sheath[50-55]. The currents in the main body of plasma lead to ohmic heating, while the voltage across the sheath leads to stochastic sheath heating. A typical schematic of electrode configuration for an rf glow discharge is shown in Fig. 3.6. The rf voltage $V = V_{rf}\sin(2\pi ft)$ (usually with a frequency f =13.56 MHz) is applied on one of the plate electrodes, separated by a distance d. A configuration when the areas of the two electrodes are equal is called *symmetric*, otherwise it is *asymmetric*. The latter one is the case of our reactors when the powered electrode is substantially smaller than the grounded one. In the asymmetric rf discharge the sheath potentials at the electrodes 1 (V_1) and 2 (V_2) in are not equal, but they depend on the ratio of the electrode surface areas A_1 and A_2:

$$V_1 / V_2 = (A_2 / A_1)^{\eta}, \tag{3.25}$$

where $1 < \eta < 4$. A usual experimental value for collisional sheaths is $\eta \approx 2.5$ (Ref. 55). One of the electrodes is usually grounded (or absent) and hence the metal reactor walls play the role of the large electrode. The effective area of such an electrode is not well defined and it depends on the discharge parameters (for example, the dissipated power or the gas pressure). From Eq. 3.25 we observe that $V_1 > V_2$ when $A_1 < A_2$. This is the consequence of the discharge current continuity, resulting in a higher current density and, therefore, in a higher voltage at the smaller electrode.

3.3.2 Rf sheath model (after Ref. 55)

In contrast to the dc discharge, the rf sheath parameters such as V_0 , J_0 , s, and n_e are oscillating (see Fig. 3.7 and 3.8). Due to the nonlinearity of electrical parameters of

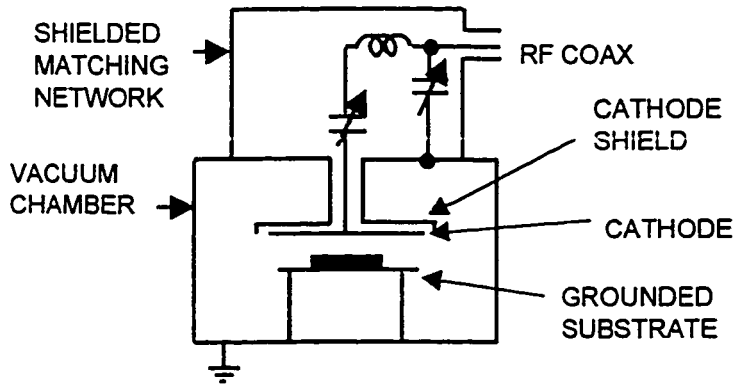

Figure 3.6. Scematic of electrode configuration for an rf glow discharge. The rf power supply is capacitively coupled to the electrodes. (From Ref. 75).

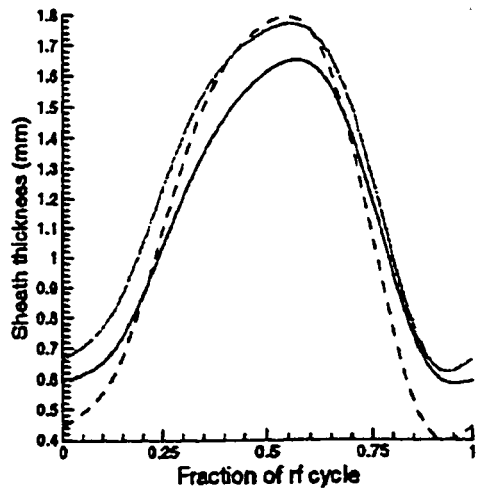

Figure 3.7 Sheath thickness as a function of time calculated from different models. $f = 10$ MHz, $T_e = 3$ eV, $n_s = 6\text{x}10^{10}$ cm^{-3} (From Ref. 64).

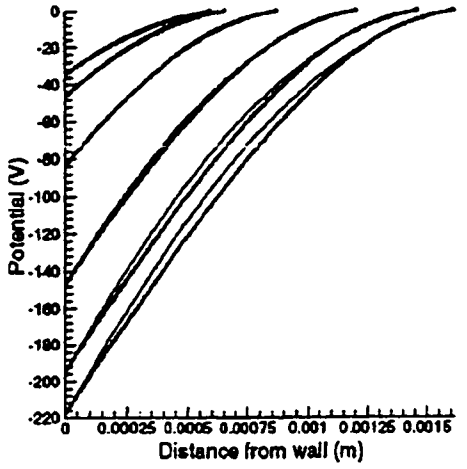

(a)

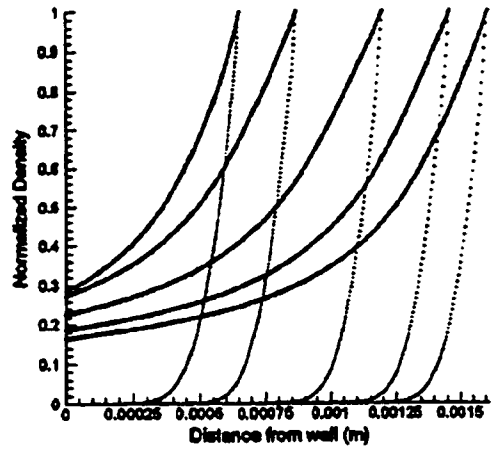

(b)

Figure 3.8 Sheath parameters as a function of space and time: (a) sheath potential distribution; (b) normalized ion (solid lines) and electron (dotted lines) densities with respect to their value at the sheath-presheath boundary. $f = 10$ MHz, $T_e = 3$ eV, $n_s = 6 \times 10^{10}$ cm^{-3} (From Ref. 64).

plasma, these oscillations are not necessarily sinusoidal, and higher harmonics of the driving frequency are usually present. These peculiarities must be taken into account, for example, when deriving plasma parameters from the probe measurements. Oscillations of the sheath edge lead to nonzero time-average electron density in the sheath that partially shields the positive space charge The Child law is now given as[55]:

$$J_i = en_s u_B = K\varepsilon_0\left(\frac{2e}{M_i}\right)^{\frac{1}{2}} \frac{<V>^{\frac{3}{2}}}{s_m^{\ 2}}, \tag{3.26}$$

where $<V_0>$ is the time-averaged sheath voltage, s_m is a maximum sheath width (see Fig. 3.8) and K = 200/243 (instead of 4/9 as in Eq. 3.20). For a fixed current density and sheath voltage, s_m is larger than s in Eq. 3.20 by a factor ≈1.36. In the case of collisional sheath, we have:

$$J_i = en_s u_s \approx 1.68\varepsilon_0\left(\frac{2e}{M_i}\right)^{\frac{1}{2}} \frac{<V>^{\frac{3}{2}}\lambda_i^{\frac{1}{2}}}{s_m^{\ 2}}, \tag{3.27}$$

same as Eq. 3.22 with a coefficient of 1.68 instead of 1.43.

The total kinetic energy gained by an ion transiting the sheath is still $e<V>$, same as for the collisionless sheath. However, the $<E_i>$ value on the electrode is reduced below $e<V>$ because part of the ion energy is lost during charge transfer and elastic collisions in the sheath, leading to the creation of fast neutrals. The mean ion bombardment energy is found to be[55]:

$$<E_i> = 0.62\lambda_i<V>s_m^{-1} \tag{3.28}$$

Thus, the consequence of collisions in the sheath is the reduced ion bombardment energy, accompanied by a proportionally increased total energetic particle flux (ions + fast neutrals) to the electrode[61].

3.3.4 Other rf sheath models

The theory of rf sheath is still an area of intensive research. Godyak and Sternberg[58] treated the regimes from $eV_{rf} << kT_e$ to $eV_{rf} >> kT_e$ in a unified manner,

including numerical solutions for the collisionless sheath, two different collisional sheath regimes, and transitions between them. They found, for example, that s_m is almost independent of V_{rf} for moderate rf voltage values. (Lieberman's theory[55] gives $s_m \sim V_{rf}^{1/4}$).

The theory of Godyak and Sternberg is developed for the high frequency sheath when the product of the frequency of applied field, $\omega = 2\pi f$, and of the ion transit time through the sheath, τ_i, is small ($\omega\tau_i << 1$). Metze et al.[62] proposed another sheath model which is applicable to the low frequency regime ($\omega\tau_i >> 1$) for which ions are able to respond to the instantaneous voltage across the sheath.

A sheath model developed by Miller and Riley[63] bridges the gap between the low and high frequency regimes. The main feature of this model is introducing a damped (or effective) potential to which the ions respond; this allows one to calculate time-dependent ion motion within the sheath. The authors were able to connect the sheath model and the bulk plasma model with an rf-circuit model, and compare the calculated and measured electrical characteristics in an inductively coupled plasma (ICP) reactor.

Panagopoulos and Economou[64] in their work, based on the Miller-Riley model, obtained spatial and temporal profiles of the sheath thickness and capacitance, electron and ion densities, potential and currents. They also derived an analytic expression for the energy split of the IED function, which we will discuss in the next section. Figs. 3.7 and 3.8 present their results for the temporal evolution of the sheath potential and the sheath thickness during the rf cycle.

3.3.5 Ion energy modulation in the rf sheath

Oscillation of the sheath potential in rf discharges leads to a dependence of bombardment energy of individual ions on the phase of the rf voltage, i.e. on the instantaneous voltage at the moment of entrance of the ion to the sheath. In a collisionless sheath this effect gives rise to a saddle-shaped IED[65-67] [Fig.3.9(a)], while in the collisional one it produces a multi-peak structure[68,69] [Fig.3.9(b)].

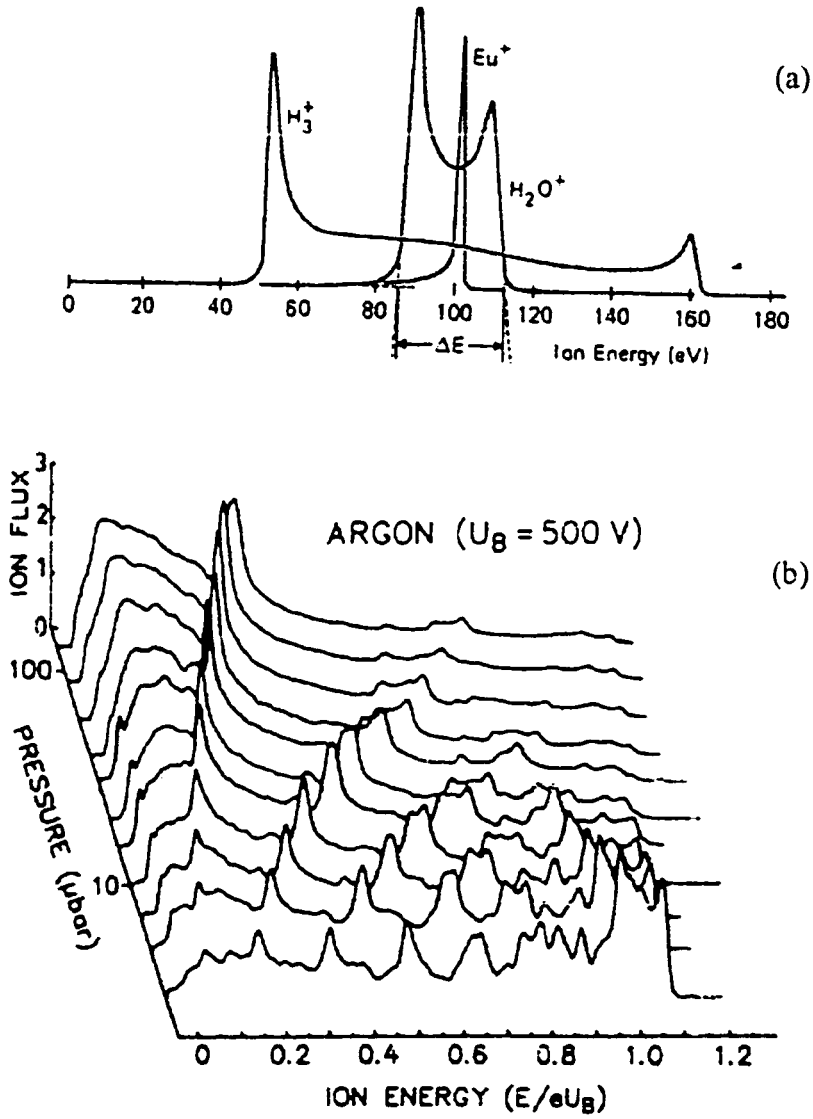

Figure 3.9 IEDFs in collisionless[67] (a) and collisional[69] (b) sheaths.

The analysis of the energy split, ΔE, [see Fig. 3.9(a)] in the saddle-shape peak was first performed by Benoit-Cattin and Bernard[66]. They assumed a constant sheath width, s, uniform space charge within the sheath, a sinusoidal sheath voltage, $V_{sh} = V_{dc} + V_{ac}sin(\omega t)$, where $V_{ac}/V_{dc} << 1$, and a zero initial velocity at the plasma-sheath boundary. ΔE can then be expressed as:

$$\Delta E = \left(\frac{8eV_{ac}}{3\omega s}\right)\left(\frac{2eV_{dc}}{M_i}\right)^{\frac{1}{2}}. \tag{3.29}$$

Eq. 3.29 may be rewritten in the following form:

$$\Delta E = \frac{8eV_{ac}}{\omega\tau_i}, \tag{3.30}$$

where

$$\tau_i = 3s\sqrt{\frac{M_i}{2eV_{dc}}} \tag{3.31}$$

is the ion transit time through the Child-Langmuir dc sheath[70]. In his work, Perrin[71] used Eq. 3.30, but he defined τ_i as the time an ion with thermal velocity needs to pass the distance λ_D. In such case $\tau_i = 2\pi/\omega_i$, and ΔE can be expressed, using Eq. 3.11, as:

$$\Delta E = \frac{4}{\pi}eV_{ac}\frac{\omega_i}{\omega} = \frac{4}{\pi}\frac{eV_{ac}}{\omega}\sqrt{\frac{e^2n}{\varepsilon_0 M_i}}. \tag{3.32}$$

The latter definition of τ_i was also used by Panagopoulos and Economou[64]:

$$\tau_i = 1/\omega_i. \tag{3.33}$$

They obtained the following expression:

$$\Delta E = \frac{2eV_{ac}}{1+(\omega t_i)^2}\{\cos\chi + \omega\tau_i \sin\chi, \tag{3.34}$$

where $\chi = \arctan\left(-\frac{1}{\omega\tau_i}\right) + \frac{3\pi}{2}$. For the low-frequency regime, $\omega\tau_i << 1$, Eq. 3.34 reduces to $\Delta E \approx 2eV_{ac}$. In the high-frequency regime one obtains $\Delta E = 2eV_{ac} / \omega\tau_i$, which is identical to Eq. 3.30 multiplied by $\pi/2$. In all cases, when the high-frequency

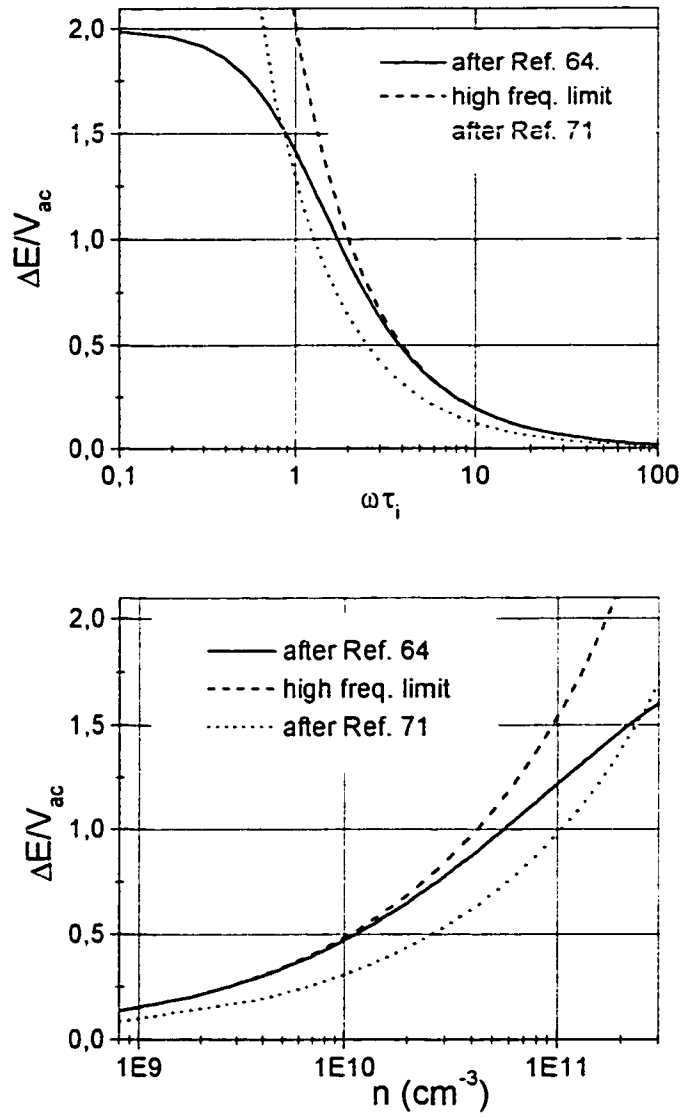

Figure 3.10 Energy split, ΔE, of IEDFs in collisionless sheath as a function of (a) transit time and (b) plasma density, assuming Ar^+ ions and f = 13.56 MHz .

regime is considered ΔE is inversely proportional to ω and to the square root of M_i, a behavior also demonstrated experimentally[67,72,73]. Eqs. 3.30 and 3.34 may be used to obtain τ_i from the measured ΔE value, as it is shown plotted in Fig. 3.10 (a). The values of n_s (Figure 3.10 (b)) and s can be then estimated using Eqs. 3.33 and 3.31, respectively.

3.4 Equivalent circuit model of the rf plasma

A simple and useful approach to describe the rf discharge is the use of an electrical equivalent circuit. The electrical model of a diode-type system shown in Fig. 3.11(a) was first proposed by Koenig and Maissel[74]. It is based on the representation of each sheath boundary as a simple capacitor in parallel with a diode and a resistor. The diode carries the large electron current during positive excursions, the resistor represents the energy consumed by the ions falling through the boundary potential, and the capacitor represents the storage of charge (unscreened positive ions) at the boundary in response to the rf voltage difference[75]. In Lieberman's circuit model[55] [Fig. 3.11 (b)] ion heating is represented by an equivalent dc current source across the dc sheath. The stochastic heating leads to equivalent sheath resistances, R_a and R_b, in series with the sheath capacitances. Although the voltage drops across the resistors are small for an electropositive plasma, the power dissipation due to the flow of current through these resistors is important, especially in low-pressure discharges. The admittance, Y_p, of a bulk plasma slab of thickness d and cross-sectional area A is represented as:

$$Y_p = j\omega C_0 + (j\omega L_p + R_p)^{-1} \tag{3.35}$$

where $C_0 = \varepsilon_0 A/d$ is the vacuum capacitance, $L_p = \omega_p^{-2} C_0^{-1}$ is the plasma inductance, and $R_p = \nu_m L_p$ is the plasma resistance. ν_m is the electron-neutral collision frequency. For the discharges used in this work, $\omega C_0 << 1/R_p$ (since $\nu_m \omega << \omega_p^2$), and $R_p \geq \omega L_p$ (since $\nu_m \approx \omega$ at 20 mTorr, and $\nu_m >> \omega$ at 200 mTorr). This means that C_0 can be neglected in Eq. 3.35.

For a symmetrical rf discharge the sheath capacitance, C_{ab} may be calculated as[55]:

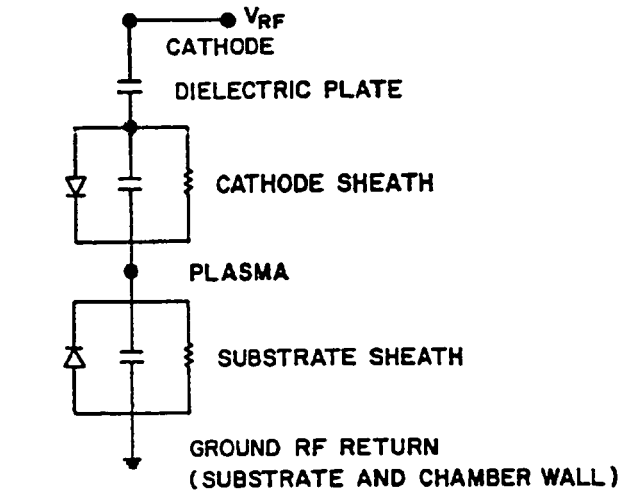

(a)

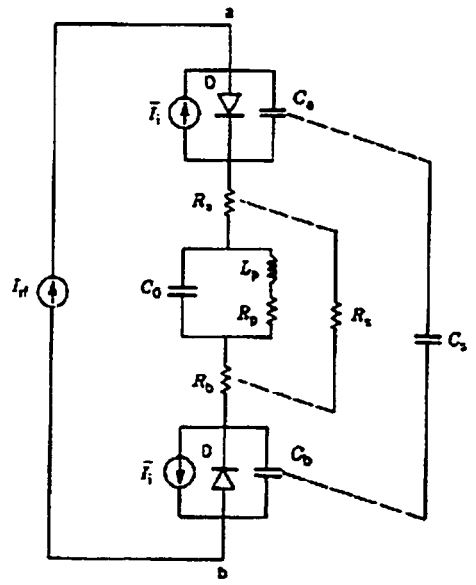

(b)

Figure 3.11 Nonlinear circuit models of the rf plasma discharge proposed by Koenig and Maissel[75] (a), and by Lieberman[55] (b).

$$C_{ab} \approx K_I \varepsilon_0 A s_m^{-1} \tag{3.36}$$

where A is the area of each electrode, and K_I is a factor equal to 0.61 and 0.76 for collisionless and collisional sheaths, respectively. Physically, C_{ab} is a series combination of two nonlinear capacitances, $C_a(t)$ and $C_b(t)$, each representing a sheath in front of the respective electrode. In highly asymmetrical reactors ($A_b >> A_a$) $C_b >> C_a$, and hence $C_{ab} \approx C_a$. This offers a method to estimate the sheath thickness when the sheath capacitance is known. For example, when a circular electrode 12 cm in diameter is used, A = 113 cm^2, Eq. 3.36 yields $C_{ab} \approx$ 60 pF and 75 pF for s_m = 1 mm for collisionless and collisional sheaths, respectively.

CHAPTER 4. Experimental methodology

The ion energy diagnostics experiments have been performed in three different vacuum systems. In this section, we describe these reactors, following which we give a detailed descrption of the multigrid ion energy analyzer, of the mass spectrometer / ion energy analyzer, and of the complete methodology used to evaluate the ion bombardment energetics.

4.1 Plasma systems

4.1.1 Reactor with a multigrid ion energy analyzer - system I

The plasma reactor I (Fig. 4.1) consists of a cylindrical stainless steel vacuum chamber (30 cm in diameter), equipped with an aluminum rf electrode (18 cm in diameter) facing a fused silica window (30 cm in diameter) at a distance of 5 cm. MW (2.45 GHz) power was applied from a periodic slow-wave structure (25 cm long), using one of the two different MW power supplies: (i) a Muegge (model M1200) generator, operating in continuous wave (cw) or pulsed modes, with the pulse frequency, f_p, varied from 1 to 10 kHz; (ii) a Hüttinger (IGM1/2450) "high-ripple" generator, with a fixed f_p = 60 Hz. The rf (13.56 MHz) power was coupled to the discharge using a tunable L-type matching network (ATX-800, Advanced Energy), connected to the rf electrode. The rf generator (RFX600, Advanced Energy) supplied stabilized cw power in a range from 0 to 100 W. Incorporated indicators allowed one to monitor the values of the forward and reflected power, as well as the self-bias voltage, V_b. Prior to the experiments, the vacuum chamber was turbo-molecularly pumped to 1×10^{-4} Torr, following which a

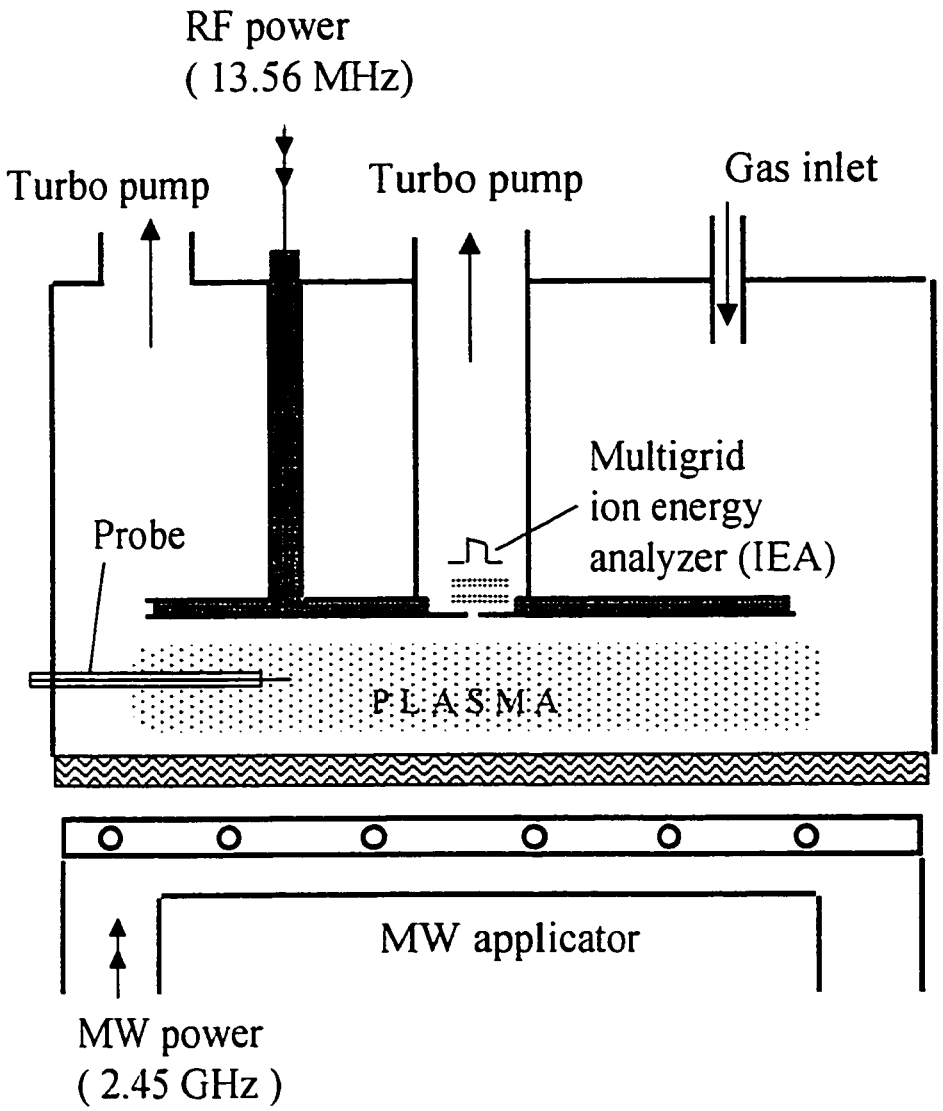

Figure 4.1 Schematic of the dual frequency MW/rf reactor with a mutigrid ion energy analyser (reactor I).

working gas flow of 5 – 20 sccm was introduced, and a pressure between 50 and 200 mTorr was adjusted. Differentially pumped ion energy analyzer (IEA) was installed at the center of the rf-electrode.

4.1.2 Reactor with a mass spectrometer / ion energy analyzer - system II

The plasma reactor II (Fig. 4.2) consists of a cylindrical aluminum chamber (30 cm in diameter and 30 cm high). Four flanges on each side (20 cm in diameter) ensured an easy access to the plasma zone; they were also used for gas inlet and electrical feed-throughs. The same quartz window and slow-wave applicator as in reactor I were used to apply the MW power. The stainless steel rf electrode is part of the Hiden EQP-1000 plasma probe mass spectrometer (see below); it has a diameter of 12 cm, and it is mounted at a distance of 10 cm from the MW window.

4.1.3 Ion assisted deposition reactor with a cold cathode ion source - system III

The ion assisted deposition (IAD) system ("Integrity-29"[76,77], Denton Vacuum, LLC) (Fig. 4.3) has a diameter of 75 cm and a height of 80 cm. It is used for the deposition of thin films by an electron beam or thermal evaporation for ophthalmic applications. The deposition is assisted by an intense bombardment by positive (usually O_2^+) ions produced by a cold cathode broad beam ion source[78] (CC-105, Denton Vacuum, LLC) (Fig. 4.4). The reactor has water-cooled stainless steel walls, it is equipped with an E-beam gun, a thermal evaporation source, and a quartz crystal micro-balance for precise deposition rate and film thickness control. Substrates (48 lenses) are

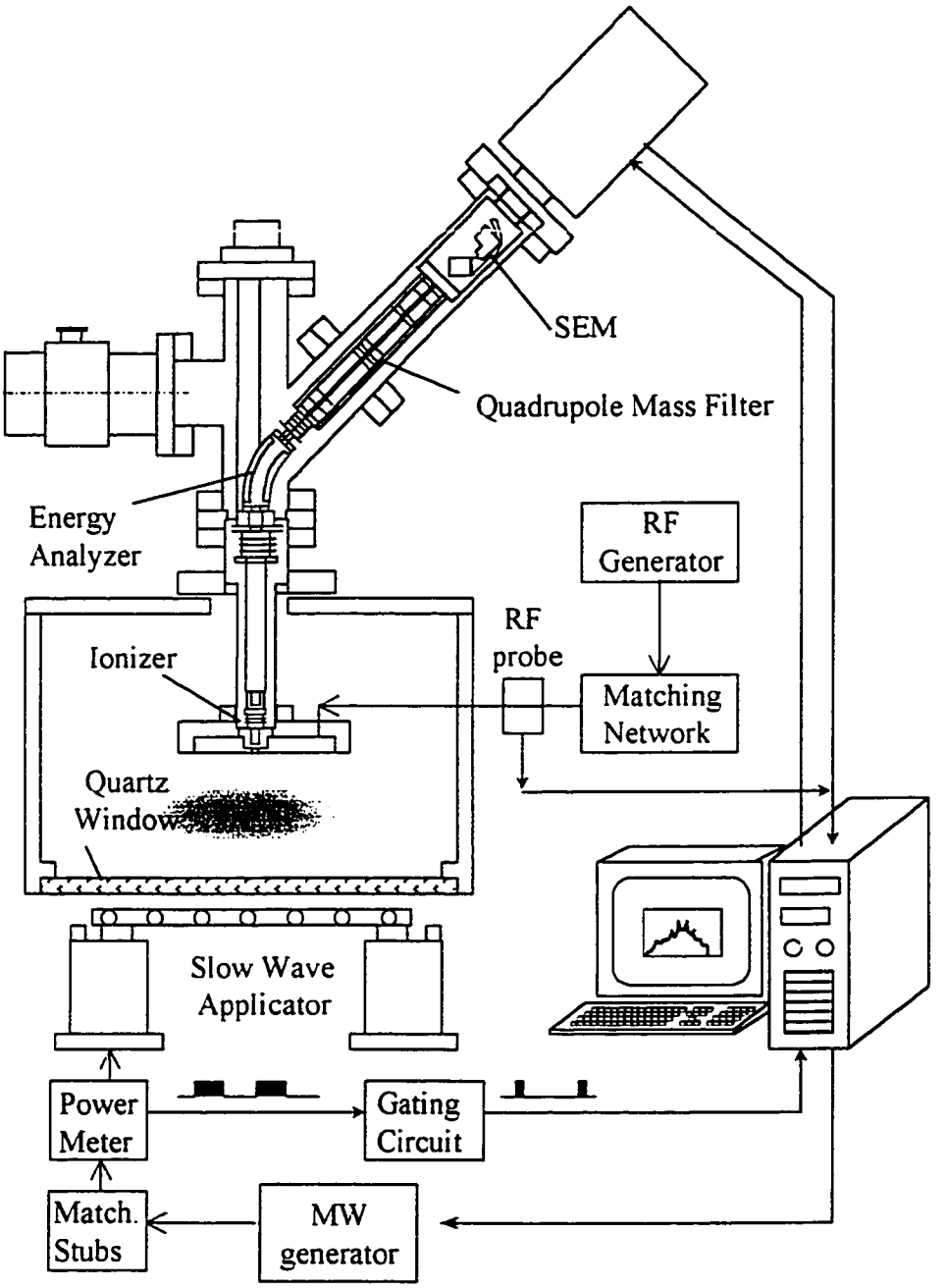

Figure 4.2 Schematic of the dual frequency reactor with the Hiden EQP-1000 mass spectrometer system (reactor II).

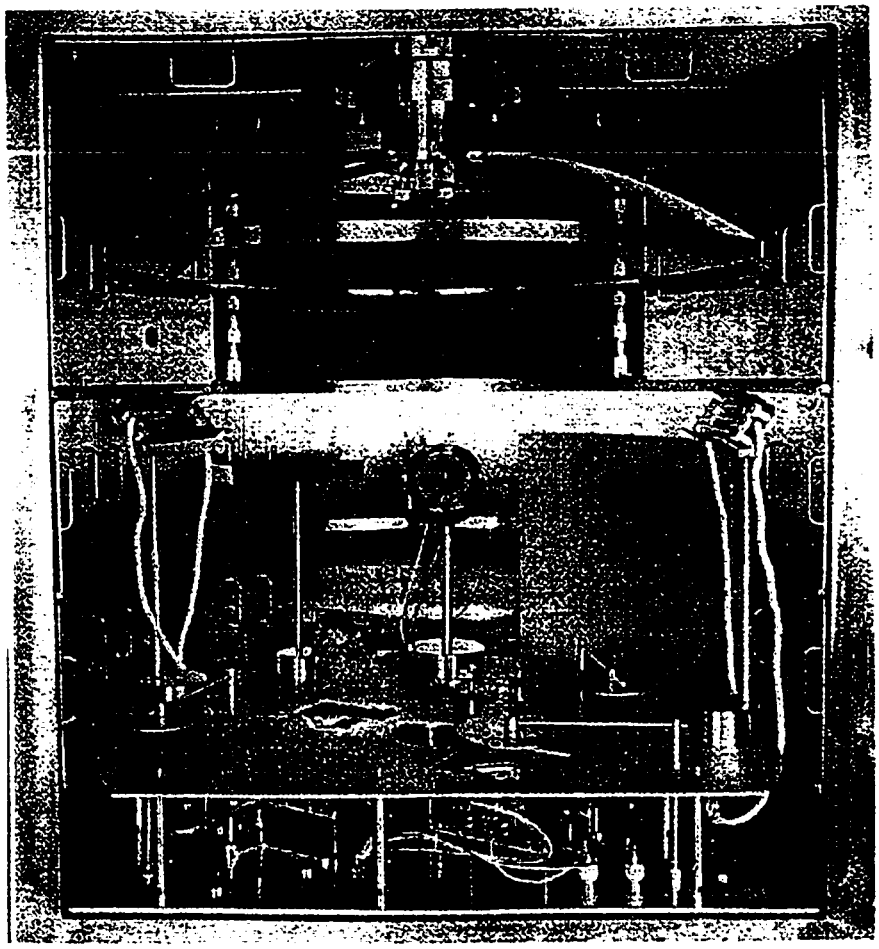

Figure 4.3 IAD reactor with the cold cathode ion source (Denton LLC Integrity-29 system).

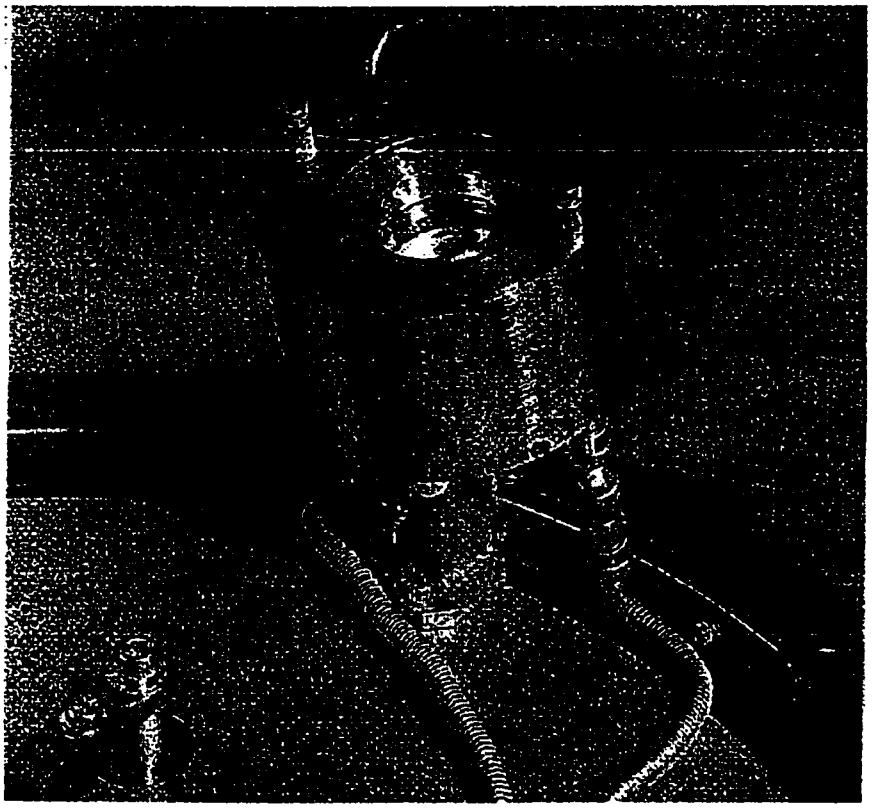

Figure 4.4(a) Cold cathode ion source, model CC-105, Denton Vacuum LLC.

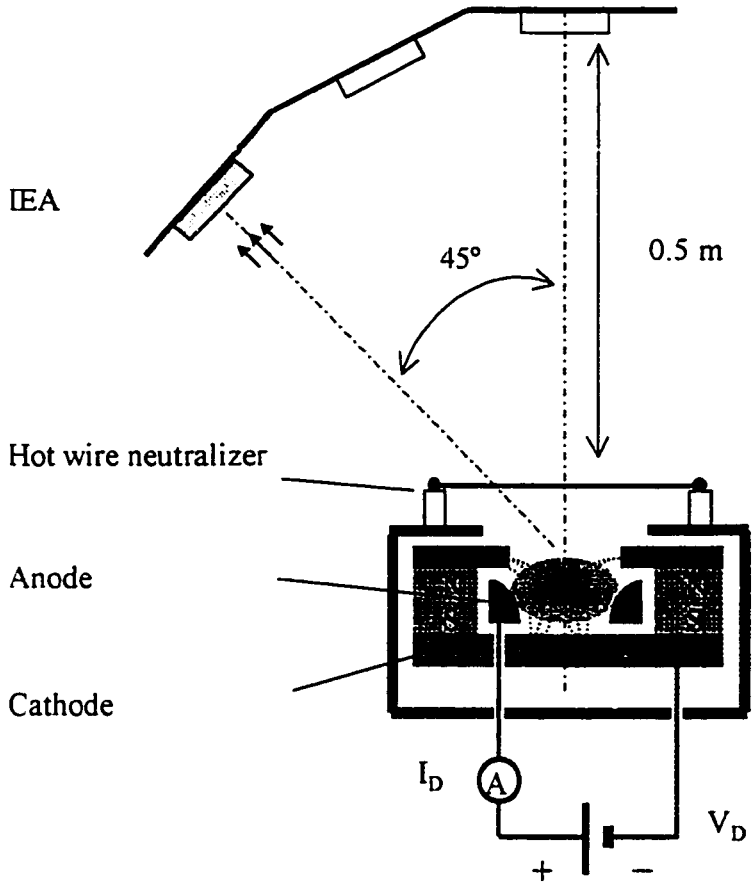

Figure 4.4(b) Schematic of the cold cathode ion source CC-105, Denton Vacuum, LLC.

fixed on the rotating calotte. The deposition cycle is typically 45-50 minutes and it is fully automated.

The ion source consists of a disc-shaped cathode, a ring anode, a set of permanent magnets, a shield, and a wire neutralizer (Fig. 4.4b). The working gas is introduced through the thin space between the cathode and the shield. Positive dc voltage, V_D, (150 - 300 V) is applied to the anode to sustain the gas discharge. This voltage determines the maximum ion energy when the cathode is grounded; when a higher ion energy is required, the whole source can be additionally electrically biased (1-2 kV). The magnetic field in the discharge zone is normal to the lines of electric field, which leads to an electron drift in the azimuthal direction. This highly improves the electron confinement and gas ionization and hence the ion current. A tungsten hot filament neutralizer was used as a source of electrons to avoid surface charging by the positive ion beam; it also served as an additional source of electrons to stabilize the discharge.

The reactor is pumped by a 3000 l/s cryopump, allowing one to maintain the reactor pressure less than $4x10^{-4}$ Torr, while using gas flow rates of 10 - 50 sccm, required for proper functioning of the ion source.

4.2 Multigrid Ion Energy Analyzer

4.2.1 Design and working principle

For this project a retarding field ion energy analyzer (IEA) (Fig. 4.5) was developed and constructed in our laboratory, adopting a three-grid design described in

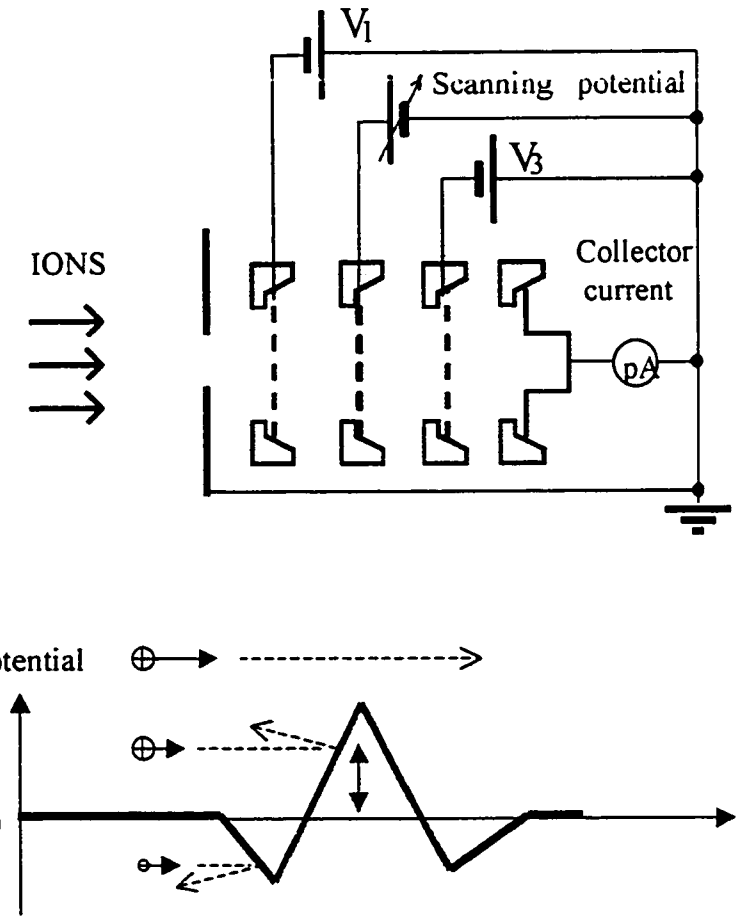

Figure 4.5 Schematic of multigrid ion energy analyzer (a) and the potential distribution inside the analyzer (b).

the literature[68,79,80]. The analyzer consists of three parallel nickel grids, and a Faraday cup as a collector. The first and the third grids have single mesh layers while the second grid was constructed from two meshes, separated by a space of 1 mm. The double-mesh arrangement reduces electric field penetration between the mesh wires, greatly increasing the ion energy resolution[79,81]. Each mesh comprises 90 lines per inch, and has a transparency of 88%. All analyzer electrodes are separated by 2 mm gaps. Negative potentials, V_1, applied to the first grid, and V_3, applied to the third grid, form potential barriers for plasma electrons and for secondary electrons, respectively. A positive scanning potential, V_s, is applied to the central grid, allowing only ions with energy higher than ZeV_s to be collected, where Ze is the ion charge. A computer-controlled voltage source / picoammeter (Keithley 487) was used to measure the collector current I. First derivative of the $I(V_s)$ dependence gives the ion energy distribution on the surface[80]:

$$f(E) = \frac{-1}{A_a T_a (Ze)^2} \frac{dI(V_s)}{dV_s} \tag{4.1}$$

where A_a is the entrance orifice area, and T_a is the total transparency of the analyzer. The integration time of the picoammeter was 16.7 ms for each reading. 12 measurements were averaged to obtain one I-V curve in order to maintain a low signal-to-noise ratio. An example of a typical I-V curve and a corresponding IEDF is shown in Fig. 4.6.

4.2.2 Pressure in the IEA chamber

The IEA was differentially pumped using a 50 l/s Balzers turbomolecular pump

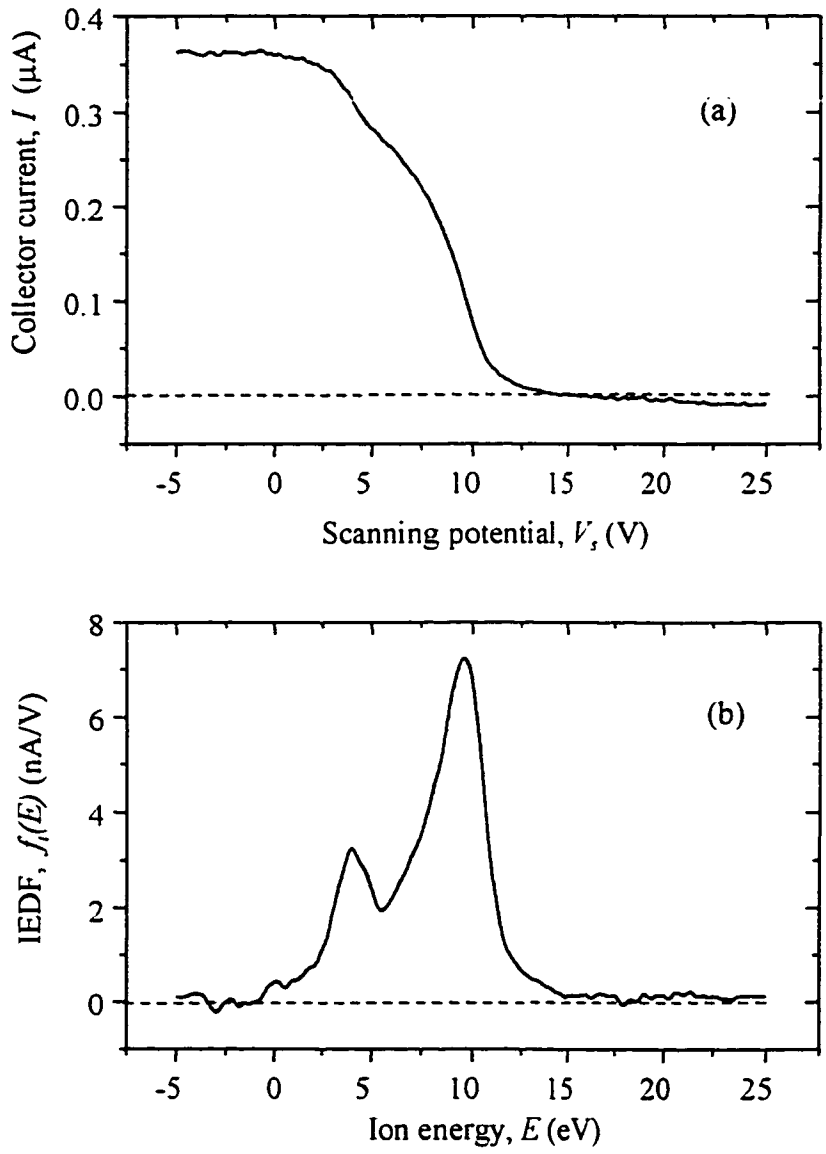

Figure 4.6 I-V curve measured with the IEA (a) and the corresponding IEDF (b). This measurement was performed in pulsed MW plasma (Huttinger generator), in argon at 60 mTorr.

backed by a 2 l/s rotary pump. Since the measurement of the IEDF may be affected by collisions inside the IEA, we made a careful estimation of the pressure distribution in the IEA chamber. The vacuum line consists of several elements outside the reactor (adapters, valve, electric feed-throughs, etc., see Fig. 4.7) with the same inner diameter of 40 mm and the total length of 30 cm, and the tube inside the reactor with a diameter of 12 cm and a length of 16 cm.

The conductance, C, of a tube of circular cross section with diameter D(cm) and length L(cm) in a molecular flow regime for air at 20 °C is expressed as[82]:

$$C(l/s) = 12.1\, D^3/L. \tag{4.2}$$

Eq. 4.2 gives $C \approx 26$ l/s for the external part and $C \approx 1300$ l/s for the internal part. The resistance of the latter part can be neglected and it can be considered as a volume with the same static pressure, p_s. The effective pumping speed, S_{eff}, is then calculated as[82]:

$$S_{eff} = SC/(S+C) \approx 17 \text{ l/s} \tag{4.3}$$

where S = 50 l/s is the nominal pumping speed of our turbomolecular pump. The p_s value can now be determined:

$$p_s = pC_a/(C_a + S_{eff}). \tag{4.4}$$

Here, C_a (l/s) = 11.6 A_a (cm^2) is the conductance of an aperture of area A_a in a molecular flow regime. For our orifice (R=125 μm) $C_a \approx 6\text{x}10^{-3}$ l/s and $p_a \approx 3\text{x}10^{-4}p$. Limiting the maximum working pressure in the reactor to 200 mTorr, we obtain $p_{smax} \approx 6\text{x}10^{-5}$ Torr.

At the end we check the choice of the flow regime. The condition for the molecular flow is $Dp_{av} < 5\text{x}10^{-3}$ cmTorr, where p_{av} is the average pressure in the tube.

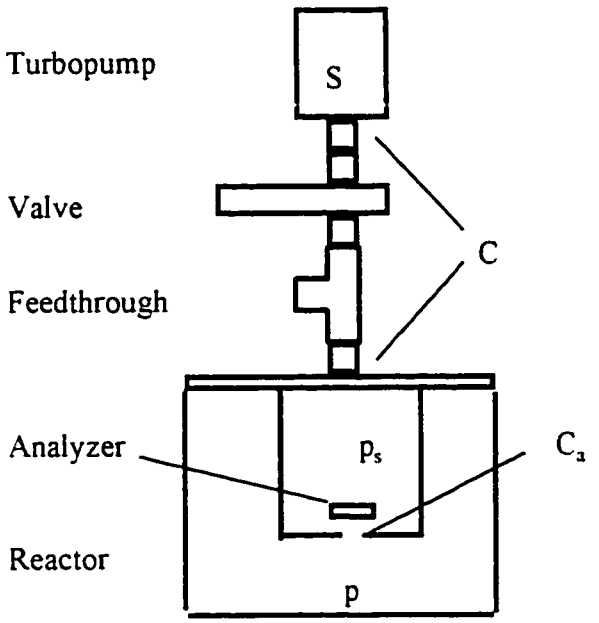

Figure 4.7 Schematic of vacuum connections in the differentially pumped IEA. See text for the explanation of symbols.

For the pumping line we have Dp_{av} = 4x(1/2)x6x10^{-5} cmTorr = 1.2x10^{-4} cmTorr, and for the orifice Dp_{av} = 2.5x10^{-2}x(1/2)x0.2 cmTorr = 2.5x10^{-3} cmTorr. Therefore, both cases correspond to the molecular flow regime.

4.2.3 Ion flux attenuation

To calculate the ion flux attenuation in the analyzer due to ion-neutral collisions, two components of the effective pressure must be considered[83]. The first one is the static pressure determined from the pumping speed, S_{eff}, and the orifice conductance, C (see previous section). The ion current attenuated by p_s at a distance L from the orifice is:

$$I_s(L) = I_0 \exp\left(-\sigma n_0 L \frac{C}{C + S_{eff}}\right) \tag{4.5}$$

where I_0 is the ion current at the level of the orifice, σ is ion-neutral collision cross-section, and n_0 is the gas concentration in the reactor. The second component is the local pressure of the effusing gas (beam pressure, p_b) determined by the orifice radius, R, resulting in an additional attenuation[68,83]:

$$I_b(L) = I_0 \exp\left(-\sigma n_0 \frac{R}{2} \arctan\left[\frac{L}{R}\right]\right). \tag{4.6}$$

Figures 4.8 and 4.9 illustrate the behavior of each of these attenuation mechanisms (σ was considered equal 10^{-14} cm^2 [Ref.55]). In our case (R=125 μm, S_{eff} = 17 l/s, L = 20 mm >>R) p_b is more important than p_s for all p values used. At p = 200 mTorr p_s leads to the losses less than 5%, while about 45% of ions collide with neutrals due to the beam pressure. These losses must be considered when ion fluxes are to be

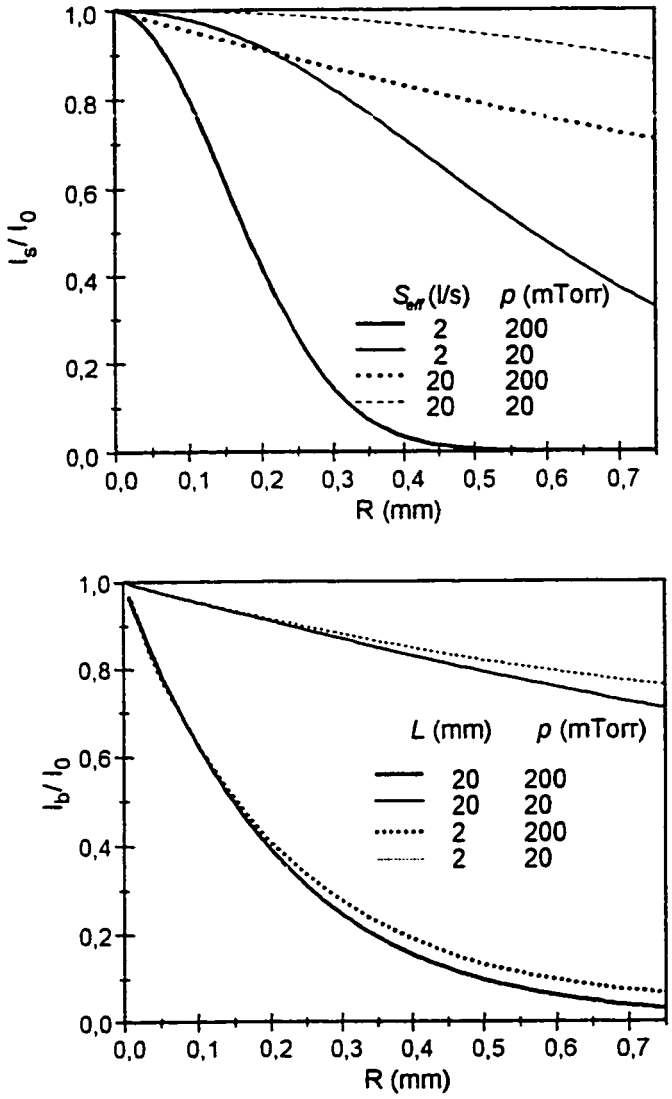

Figure4.8 Relative intensity of the ion beam attenuated by the static pressure (a) and by the beam pressure (b) for different values of pressure in the reactor, *p*.

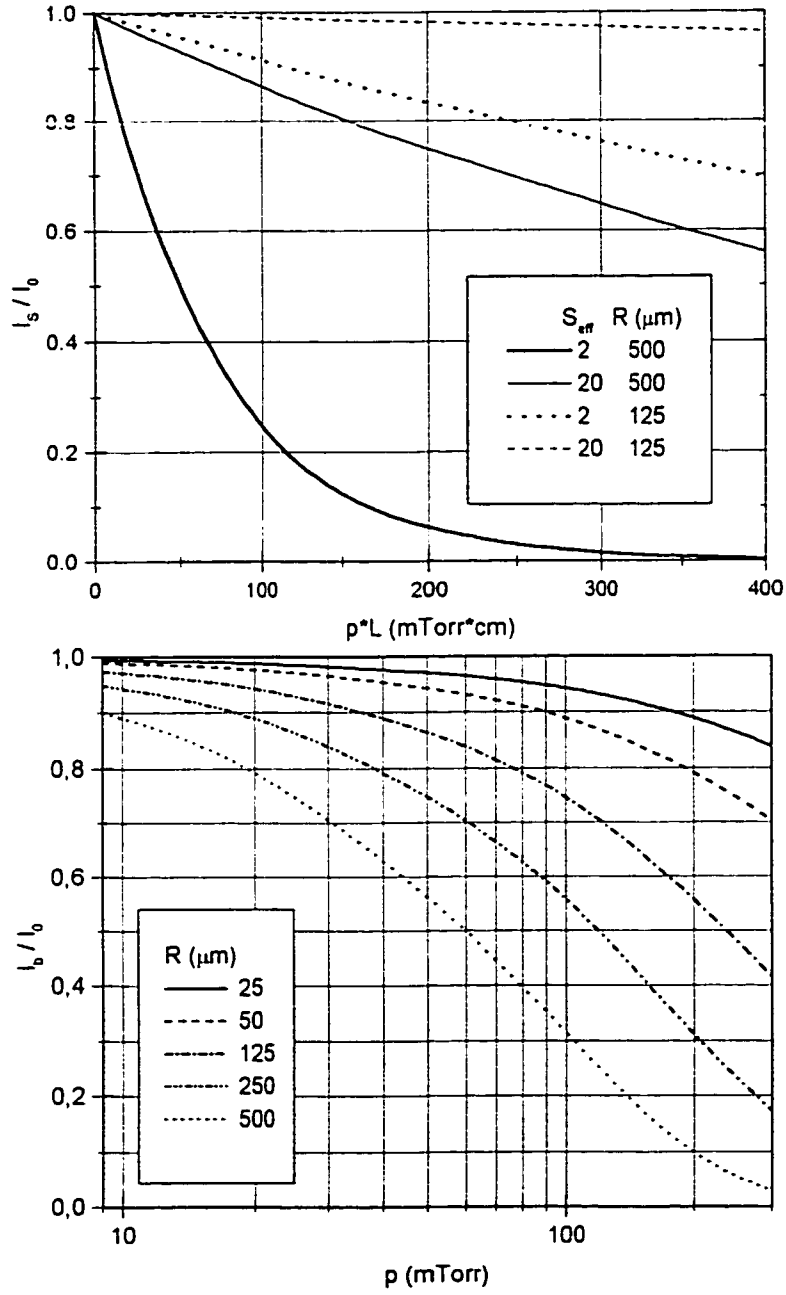

Figure 4.9 Relative intensity of the ion beam attenuated by the static pressure p_s for the different orifice radii and pumping speeds (a) by the beam pressure p_b at $L = 20$ mm for different orifice radii (b).

quantitatively determined. Note that for $L>>R$ (our case for L > 2-3 mm) I_b does not vary with L, hence the position and the dimensions of the analyzer are not critical until a large L is used when the static pressure becomes important.

4.2.4 Attenuation by grids

Four independent (not aligned) sequential grids with an individual geometrical transparency of 0.88 give a total transparency of $0.88^4 \approx 0.6$. This value was considered as maximum possible for ions which undergo additional losses related to deflection due to grid potentials. Only a proper calibration procedure with well-defined ion beam can give the exact value of the analyzer transparency for each ion energy. This experiment has not been performed with our IEA; however, our work with the cold cathode ion source (Chapter VII) allowed us to obtain a reasonable value of ~ 0.4 for the effective transparency for a broad IEDF (0-200 eV). For example, in the case of O_2^+ ions using I_D = 2A, p = 2 mTorr, and R = 0.93 mm the measured ion current was I = 1.4 μA, corresponding to a current density J = 52 μA/cm^2. Comparative measurements with a Faraday cup at the same conditions gave J = 120 μA/cm^2 [Ref. 77] thus yielding a ratio 52/120 = 0.43.

4.2.5 Acceptance angle

The radius of the opening in all diaphragms was 3 mm, the most distant one was about 25 mm from the orifice. Only ions with an angle of incidence less than α = arctan(3/25) ≈ 7° could be collected, while neglecting the effect of applied voltages on

ion trajectories. At low pressures ($s/\lambda_i < 1$) ions have a very narrow angle distribution, and hence most of the ions passing the orifice enter the analyzer. At higher pressures ($s/\lambda_i>1$) collisions in the sheath lead to a considerable broadening of the ion angle distribution[60,68,84,85] (Fig. 4.10), and only part of the total ion flux is analyzed. Such effects complicate the determination of absolute ϕ_i values in our measurements.

Monte-Carlo simulations were used to evaluate such effects[86,87]. In the work of Thompson et al.[87] it was shown that for $s/\lambda_i > 6$ the average ion angle, φ, saturates at $\varphi \approx 25°$. This allows one to consider that the measured-to-total ion flux ratio for highly collisional sheaths is constant, and approximately equal to 0.2, assuming a gaussian distribution. Since for Ar^+ ions λ_i (mm) $\approx 30/p$(mTorr) (see Eq. 3.8), the latter condition can be rewritten as $p*s > 180$ mTorr mm; this is almost always the case for the rf sheath at the powered electrode. However, the measurements made by Liu et. al.[68] do not support this conclusion, showing no saturation of φ until $p = 500$ mTorr ($\varphi \approx 18°$) in argon rf plasma.

4.2.6 Signal-to-noise ratio

Let us estimate the collector current for the worst scenario such as low density plasma at a high pressure. For $n_e = 10^9$ cm^{-3} we can expect $J_i \approx 20$ μA/cm^2 at the rf electrode (Eq. 3.18) which leads to the total current through the orifice $I = A_o J_i = 3.14*(0.0125)^2*20 \approx 10$ nA. This current is reduced by half due to p_b; according to the above, about one fifth of the rest will possess angles small enough to enter the analyzer,

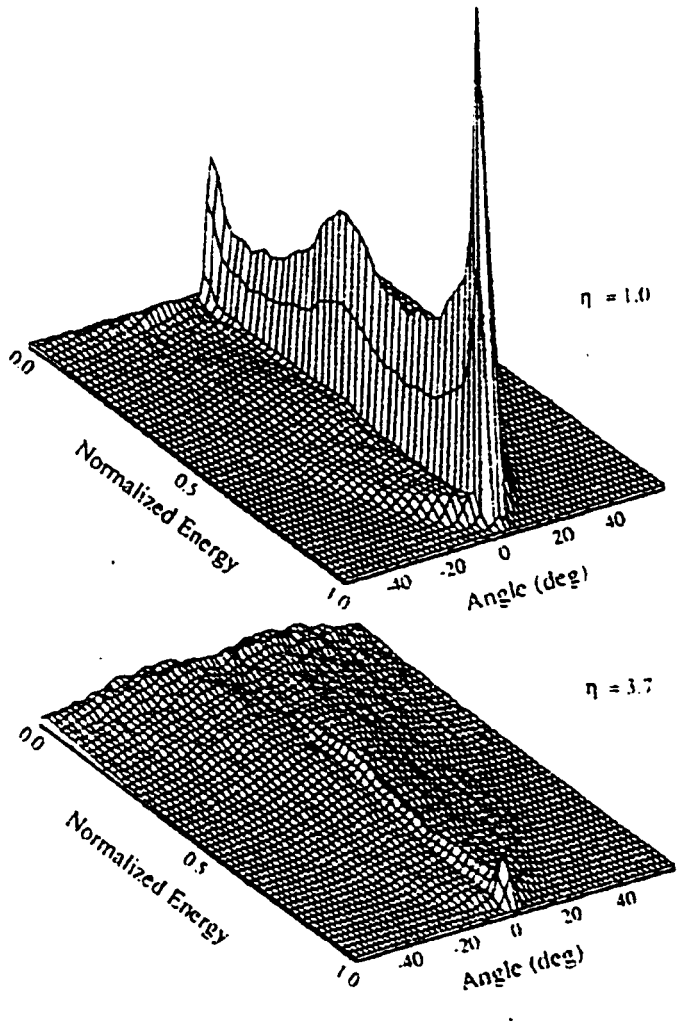

Figure 4.10 Calculated IEDFs at s/λ_i ratio 1.0 and 3.7 for SF_5^+ ions in SF_6 gas (After Ulacia and McVittie[86]).

where a half of the arriving ions is lost on the grids. As a result, $I \approx 500$ pA is collected. For a reliable evaluation of the energy distribution, a current of at least one tenth of the latter value, i.e. 50 pA, should be measured with confidence. This estimate represents a challenge for the experimentator since electrical noise in cables can become significant, especially in rf and pulsed MW regimes.

In our work we used a relatively large aperture (compared with R = 1 - 5 μm used by Woodworth et. al.[85]) to obtain measurable ion currents with an acceptable signal-to-noise ratio. It is shown in Fig. 4.11 that for small aperture radii the collected current increases as R^2. In addition, we systematically used averaging of multiple (usually 12) measurements for each experimental point in order to reduce the noise at the expense of the total measurement time.

4.2.7 Energy resolution

. The dimensions and the construction (doubled second grid) of our IEA are very similar to the analyzer of Liu et. al.[68], who obtained an energy resolution of 5% using a commercial ion gun as source of ions. In spite of a spherical geometry in their case we expect a comparable resolution for our IEA. Kortshagen and Zethoff[80] describe a parallel grid analyzer of the same design, with about the same mesh characteristics as ours, but larger distances between individual grids (7 mm) and a single second grid. From experimental observations of fine structures and from a numerical simulation of the analyzer performance they estimate the energy broadening, ΔE_R, of about 1 eV for the E_t values in the range from 15 to 20 eV. Sharp drops and resolved peaks measured with our

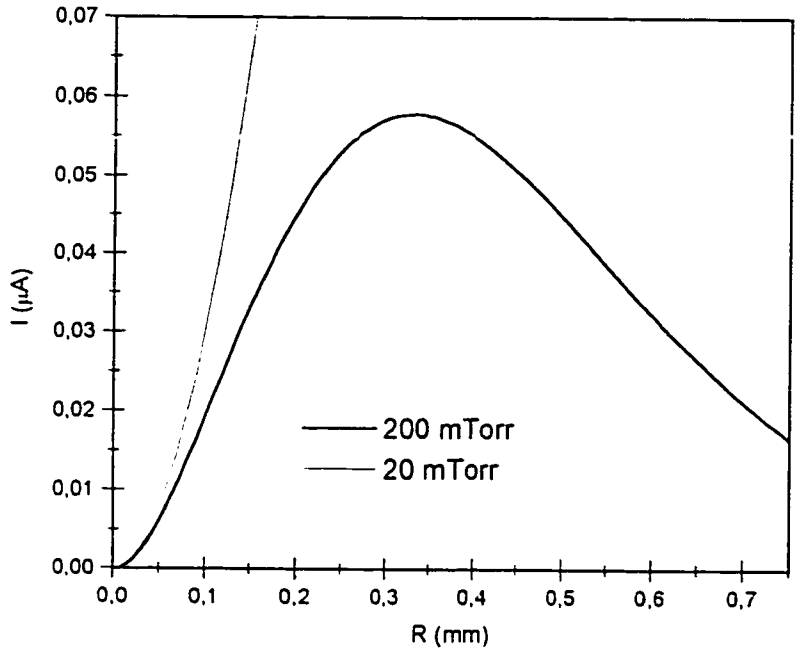

Figure 4.11 Current of Ar^+ ions collected at the distance L = 20 mm from the orifice as a function of orifice radius at different pressures of argon in the plasma zone. Conditions: J_0 = 1 μA/mm², S_{eff} = 20 l/s.

analyzer (for example for a MW plasma in He at 100 mTorr, Fig. 5.11) allow us to estimate that ΔE_R is 1-2 eV for E_i values below 20 eV, and about 5% of E_i for higher energies.

As a rule, the quality of the IEDFs was limited not by the resolution of the analyzer but rather by the electric noise and plasma instability. Another factor, rarely discussed in literature, namely the grid contamination, was found to negatively affect the signal quality. Thin dielectric films, presumably a product of contaminants such as desorbed molecules or cracked oil vapors, were depositing on the grids and they perturbed the potential distribution. This leads to an additional noise and energy shift, thus causing a dependence on the direction of potential scanning (hysteresis). All grids were immediately replaced when such phenomena were observed.

4.3 Hiden EQP-1000 plasma probe

The Hiden EQP-1000 System (Fig. 4.12) is an advanced plasma diagnostic tool with combined high transmission ion energy analyzer and quadrupole mass spectrometer, acquiring both mass spectra at specified ion energies and ion energy distributions of selected plasma ions. Two basic operation modes are available for the EQP system - the plasma mode (sometimes called SIMS mode in the manual) and the RGA mode (from the residual gas analysis). In the plasma mode the ions produced in the plasma enter through an orifice of 50 μm in diameter, located in the center of the rf electrode. In the RGA mode the neutral and radical species arriving from the plasma zone are ionized in the incorporated electron impact ionizer, and then they are analyzed.

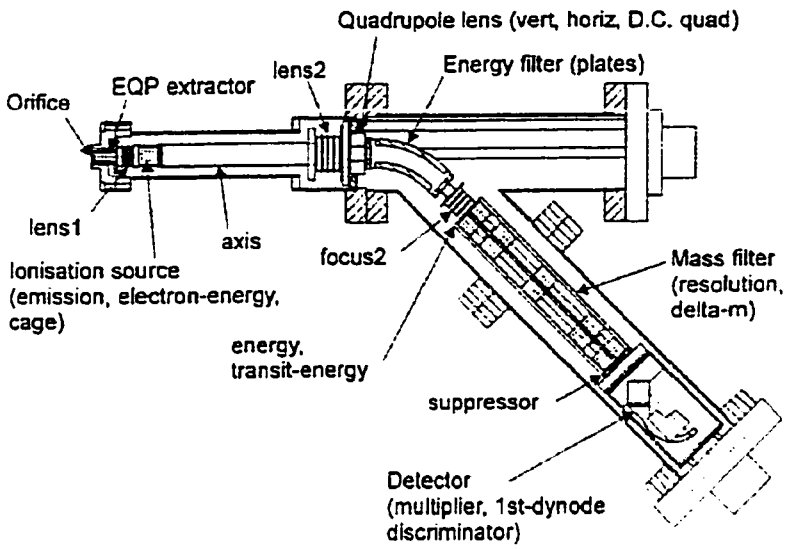

Figure 4.12 Schematic diagram of Hiden EQP probe ion optics (After Ref.88).

The system is differentially pumped by a 60 l/s turbomolecular pump, allowing one to maintain the pressure inside the spectrometer (p_s) below 10^{-6} Torr during all experiments; this ensures a collision-free transit of ions, as well as a proper function of the secondary electron multiplier. Attenuation by p_b is also quite low [~5% for p = 100 mTorr, see Fig. 4.9(b)] and we neglected it in this work.

The instrument is operated via an IBM-compatible personal computer running Hiden Analytical Limited's MASsoft application under Microsoft® Windows™. The MASsoft application provides complete control and tuning of the instrument; it is also used for data acquisition, storage, recall and analysis within Microsoft's Windows Interface.

4.3.1 Energy analyzer

A 45 degree sector field energy analyzer (radius = 75 mm) is used in the EQP system for maximum transmission and to provide minimum perturbation to the ion flight path within the analyzer for optimum energy resolution. The analyzer provides constant transmission and constant energy resolution functions throughout the ion energy range from -1000 eV (negative ions) to +1000 eV. ΔE_R of the analyzer is 0.25 eV FWHM[89]. The potentials on two sector plates are always kept constant (7.27 V), selecting ions with an E_r/Z ratio of 40 eV. The ion energy scan is thus achieved by accelerating or decelerating ions entering the probe. Two modes of scanning the ion energy are available for the EQP-1000 system: (i) "energy potential" mode with a limited range from -90 to +90 V and a minimum increment of 0.05 V; and (ii) "reference potential"

mode with a range of ± 1000 V, but with a minimum step of 1 V. We used the mode (i) in our measurements in pure MW plasma, while the mode (ii) was used when the rf power was applied and the ion energies were considerably higher.

4.3.2 Quadrupole mass filter

On leaving the energy filter, the ions are slowed down to an energy of 3 eV for the transit through the quadrupole mass filter. A triple filter mass analyzer construction is used in the EQP system. It includes short 'rf only' pre- and post-filters which minimize the fringe field effects at the primary mass filter, thus enhancing peak separation and transmission, particularly for high mass species. Each filter consists of four cylindrical rods 9 mm in diameter; the total mass filter length is 254 mm. The main mass filter is driven by the superposition of rf and dc potentials. Ions with a stable trajectory (corresponding to a given M/Z ratio) pass through the mass filter. Mass resolution of the filter can be controlled by software. The standard resolution, preset by the manufacturer, is 1 a.m.u. at 5% peak height. A selected mass range (up to 510 a.m.u.) can be scanned with a minimum increment of 0.01 a.m.u.

4.3.3 Detector

The detector is an off-axis-mounted continuous dynode secondary electron multiplier (SEM) which operates in a pulse counting mode. Ions passed through the mass filter are accelerated toward the front of the detector (first dynode), where electrons are produced as a result of ion impact on the wall. These electrons are directed into the

multiplier to produce an electric pulse of intensity sufficient for counting by a 24 bit counter. The first dynode voltage is varied to suit the ion type (positive or negative), but the multiplier always detects electrons, and its voltage is normally independent of acquisition mode. The detector's counting range is from 1 to 10^7 counts per second. Averaging or accumulating counts over repeated mass and energy scans by software is used to increase signal to noise ratio in the analysis of minor components. A signal gating input is included to provide for time resolved plasma studies with a resolution of 1 μs. The maximum working pressure for SEM is $5x10^{-6}$ Torr; at a higher pressure possible gas discharges may burn the detector.

4.3.4 Internal ionizer (ion source)

The EQP system is equipped with an internal electron impact ionizer for high sensitivity analysis of plasma gas neutrals and radicals. The ionizer includes two oxide coated iridium filaments, with a radially symmetric cage assembled in a close coupled configuration to the plasma sampling orifice. The selected filament, heated by dc (~3.5 A) current, emits electrons which enter the source cage with a defined energy. The filament current is controlled by the measured electron emission current. For an emission of 400 μA, the required filament current almost does not change for the values of electron energy from 18 to 70 eV; higher filament currents are necessary for lower electron energies due to changes in the ionizer discharge. Running the filaments in this region may lead to filament damage; therefore, a minimum electron energy of 4 eV is set to protect the filaments. A key feature of the ionizer design is the confinement of

electrons within the ion cage vicinity, ensuring a high degree of control of the ionizing environment necessary for detailed measurements of the appearance potentials used in the analysis of radicals.

4.3.5 Ion optics

In addition to the analytical elements, EQP possesses three electrostatic lenses (lens1, lens2 and focus2) and one quadrupole lens used to guide the extracted ion beam throughout the system with minimum losses (Fig. 4.12). The transfer lens1 is used to refocus the ion beam from the sampling orifice onto the exit aperture of the electron-impact ion source. This lens is not used when working in the RGA mode. From the ion source, the ions are accelerated into the drift space, which they pass with a constant energy. Lens2 matches the ion source to the energy filter for efficient ion transfer. The quadrupole lens is used for the beam alignment control and to correct for the beam astigmatism. Finally, decelerating lens (focus2) reduces the kinetic energy of the ions and focuses the beam before its injection into the quadrupole mass filter.

4.3.6 Time-resolved measurements

Time-resolved measurements were accomplished by introducing a home-made pulse gating circuit which supplies pulses of controlled width and delay with respect to the MW pulse front (Figs. 4.13 and 4.2). Only ions which arrive during the gating pulse are counted in this regime. In order to obtain adequate signal-to-noise ratio, counts were accumulated over a period of about 200 MW pulses. The time required for an ion to pass

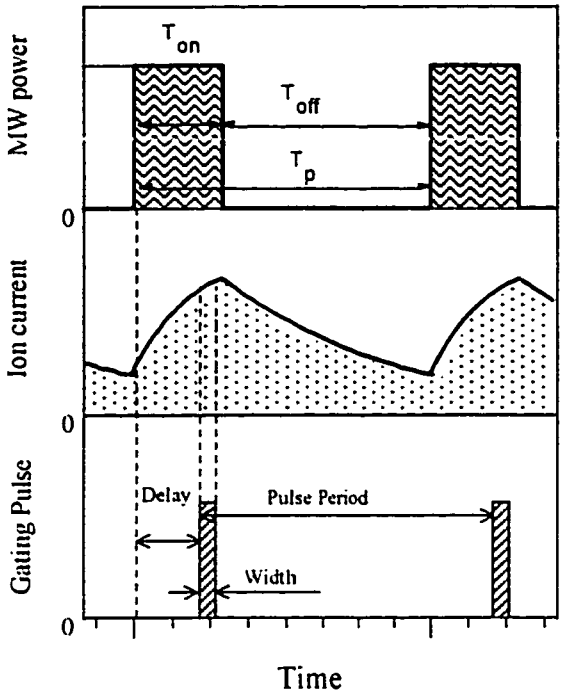

Figure 4.13 Schematic illustration of pulse gating.

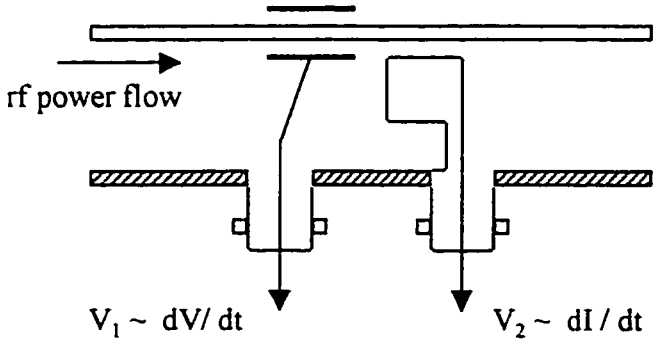

Figure 4.14 Schematic diagram of typical derivative probes used to measure voltage and current wave forms (From Ref. 90).

all the way from the entrance orifice to the SEM (about 100 μs for Ar^+ ions) was taken into account when analyzing the ion distributions with respect to the MW pulse front.

4.4 Rf-probe

In most rf plasma reactors the losses in cables and matching networks represent a significant part (up to 90%) of the total dissipated power. In order to gain information about the power dissipated in the discharge itself, proper measurements of current and voltage waveforms on the rf electrode (or at least in its close vicinity) must be performed[55,90,91].

Capacitive and inductive probes can be used for measuring the rf voltage, V_{rf}, and current, I_{rf} (Fig. 4.14). If these probes are small and located close to each other, they provide full information at a common point. The probe signals are proportional to the derivatives of V_{rf} and I_{rf}. This turns into an advantage since the signals at higher frequencies are larger than the V and I values measured directly, thus improving the signal-to-noise ratio at higher harmonics[90].

In this work a combined current- and voltage-rf-probe (ENI), inserted between the matching unit and the vacuum feed-through (see Fig. 4.2), was used for detailed plasma impedance and power dissipation measurements. The instrument consists of three modules, namely the sensor head, analysis section, and RS-232 converter block, which provides a link with a computer. The design of the probe assures a very low insertion loss (~ 0.5%) and a low voltage/current channel cross-talk (<-55 dB). The frequency range for the current and voltage measurements is from 1 MHz to 60 MHz, maximum

working voltage is 10 kV and maximum working current is 70 A. An rf noise-immune fiber optic link is used between the analysis section and the converter. The values of rf current, voltage and phase at the main frequency (13.56 MHz) were measured. The dissipated rf power and the complex reactor impedance were calculated using the "V/I Probe" software. The possible harmonics were not taken into account. The error of measurements is less than 4% for current and voltage values, and less than 0.2° for the phase.

4.5 Surface treatment of polymers and complementary analyses

The rf electrodes in both plasma systems I and II served as a sample holder for the experiments aimed at plasma treatment of polymer surfaces, in order to elucidate the role of participating ions. In this case the polymer surface was facing the high-density MW discharge, or it was exposed to intense ion bombardment in an rf discharge, or both. Additional treatments were performed in the IAD system (III) using the cold cathode ion source. After treatment the samples were exposed to the ambient atmosphere before being further characterized.

The surface chemical structure of model polymers such as polycarbonate (PC) and polyethylene-terephthalate (PET) was determined in the VG-ESCALAB MK II surface analytical instrument by X-ray photoelectron spectroscopy (XPS), using Mg-K_α radiation. The pressure in the analytical system was below $5x10^{-9}$ Torr, and the take-off angle was 45°. The measured XPS spectra were not smoothed prior to deconvolution. The inelastic background was subtracted using Shirley's method[92]. A curve-fitting

SURSOFT program has been used, which allows one to vary the fitting parameters such as the Gaussian/Lorentzian ratio (60%/40% used here), the full width at half maximum (FWHM), and the peak position. The curve-fitting quality was evaluated by the chi-square convergence. The peak assignment was based on the data available in literature.

CHAPTER 5. IEDFs in continuous and pulsed MW plasmas

In this section we present the results on the ion energetics in MW plasma excited in cw or pulsed modes. We first reveal the basic behaviour of cw plasma (section 5.1) as an introduction to the analysis of pulsed plasma using the IEA, presented in a form of a published article (section 5.2).

5.1 Continuous wave MW plasma

We start the description of experimental results from the simplest configuration possible in our reactor, when only the cw MW power is applied to sustain the discharge. In this case the excitation frequency is much higher than ω_i for any achievable plasma density, hence the sheath characteristics can be treated as in a dc sheath (see Chapter 3.2). In this case, V_p is solely controlled by the electron temperature (Eq. 3.19).

In this section we present the results obtained with the EQP system. The IEDFs of Ar^+ ions from MW plasma are shown in Fig. 5.1, and they exhibit single peaks. The amplitude of the IEDFs and the peak energies decrease with increasing p. The peak shape symmetry at 20 mTorr is an indication of a non-collisional sheath, while at higher pressures a low energy tail is developed due to collisions during the sheath transit. IEDFs with shapes similar to those obtained here for our MW plasma have also been reported by Charles and Boswell[93] for the case of high-density helicon rf plasma in oxygen, but with higher peak energies (30 eV). The peak energy corresponds to V_p, which for MW plasma was found to vary between 6 and 9 V. Differences in V_p values between the 20-200 mTorr MW plasma and the 2 mTorr helicon RF plasma is due to a higher kT_e of the latter, in comparison with our lower kT_e values. Here, the maximum ion energy is found to be < 12 eV, resulting in mild ion bombardment at the target electrode, very suitable for polymer processing.[94,95]

The possibility of mass-resolved measurements with the Hiden plasma probe allowed us to measure the IEDFs for each kind of ion species arriving from the plasma.

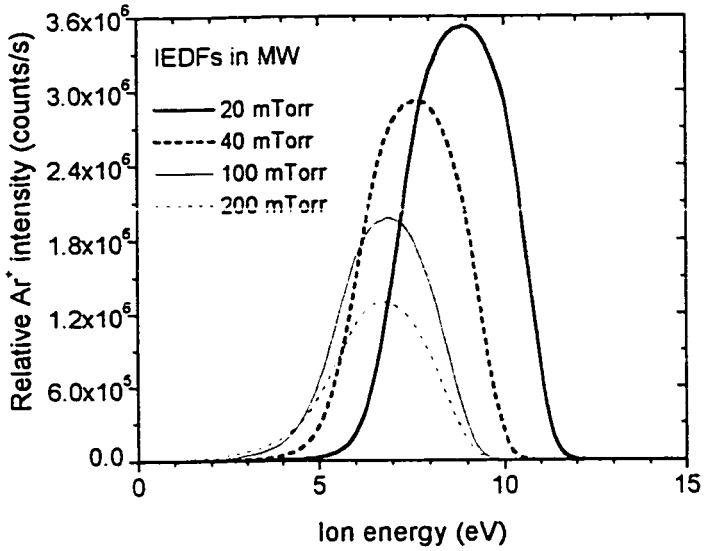

Figure 5.1 IEDFs of Ar^+ ions in cw MW discharge in Ar at different pressures for a MW power of 300 W.

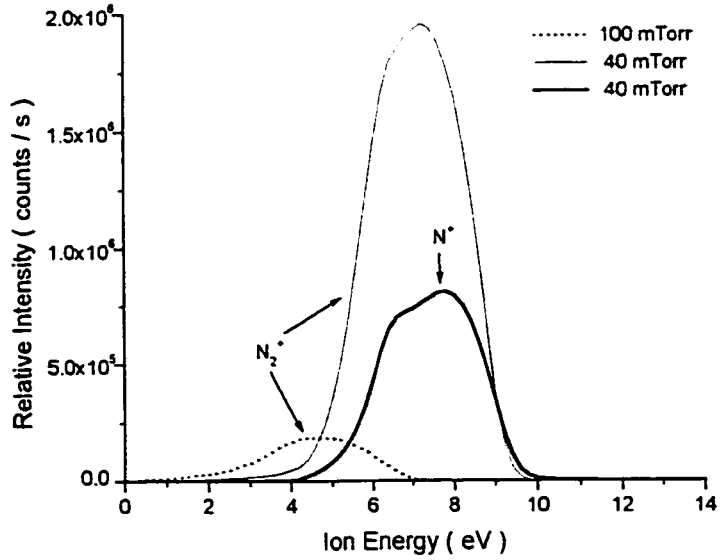

Figure 5.2 IEDFs of N^+ and N_2^+ ions in MW discharge in nitrogen at different pressures for a MW power of 300 W.

The N_2^+ and N^+ IEDFs shown in Fig. 5.2, are seen to be single peaks and similar to those observed for Ar^+ ions, indicating V_p values in the 5 to 10 V range. We can compare MW plasma IEDFs with the distributions that are usually observed at the grounded electrode of capacitively coupled rf plasmas (see Fig. 6.3 in section 6.1.2).

The peak position for N_2^+ and N^+ distributions, taken at the same plasma pressure (40 mTorr in Fig. 5.2), correspond to the same ion energy since the ions are accelerated by the same potential difference. We will see further that the shape of distribution may vary for different species depending on σ values.

The following section presents an article published in the Journal of Applied Physics, where we examined the effect of MW pulsing on the ion energy characteristics using IEA measurements. Similarity of the distributions obtained by two techniques, namely the EPQ-1000 and IEA for cw MW plasma will become clearly visible (compare Figs. 5.1 and 5.5). The more apparent tail in the latter figure is presumably due to a higher acceptance angle of the IEA which allows one to collect more ions scattered by collisions in the sheath. These results, together with the distributions measured in pulsed MW and MW/rf plasmas by these two independent techniques (Chapters 6 and 7) convinced us about the reliability of our IEA measurements.

5.2 Ion energy distributions in pulsed large area microwave plasma

Oleg Zabeida and Ludvik Martinu[a)]

Department of Engineering Physics and Materials Engineering,
Ecole Polytechnique, Montreal, H3C 3A7, Quebec, Canada

Article is published in

Journal of Applied Physics **85**(9), 6366-6372

1 May 1999

Received 4 November 1998; accepted for publication 28 January 1999

a) E-mail: lmartinu@mail.polymtl.ca

Abstract

The energy and the flux of ions impinging on surfaces exposed to low pressure plasmas are important factors which determine the chemical structure and the physical properties of the surfaces and of the thin films. In the present work, we use a large area microwave (MW) plasma reactor in which a grounded sample holder is exposed to a MW (2.45 GHz) discharge excited in different gases, such as Ar, N_2, and He, at a pressure ranging from 50 to 200 mTorr. A three-grid, differentially pumped ion energy analyzer is used to measure the ion energy distribution functions (IEDF). The use of a pulsed plasma gives rise to a structured IEDF in which the mean ion energy values vary between 2 and 10 eV. The pulse frequency and the duty cycle were found to strongly affect the IEDF and the ion flux. The evolution of the IEDF is analyzed in terms of the pulsed plasma global model, used to derive the characteristic time constants of plasma ignition and plasma decay. It is shown that the ions in the low energy portion of the IEDF originate from the time period between the individual power pulses, and their relative contribution increases with decreasing the duty time. Controlled pulsing thus allows one to selectively adjust the ion energy, and thereby the surface phenomena in materials processing which are primarily influenced by ion bombardment.

5.2.1 Introduction

High frequency plasma has been extensively used for materials processing such as plasma-enhanced chemical vapor deposition, etching, and surface modification. Plasma interacts with exposed surfaces via energetic particles (electrons, ions, fast neutrals), free radicals and photons, which control, in synergy, the surface effects.[94,95] Bombardment by ions is of particular importance: it leads to densification, due to resputtering and knock-in effects in deposition, to reactive ion etching, and to significant surface modification of materials such as metals and polymers.

In a plasma excited continuously at a single discharge frequency, the energy and flux of the individual species cannot be decoupled. Two approaches may be used to allow

one to control them separately: (i) dual-mode microwave / radiofrequency (MW/RF) plasma, in which RF-powered substrate holder-electrode is exposed to the principal MW discharge;[35,36,96,97] and (ii) a pulsed regime, where the power is applied only for a fraction of time. Pulsed discharges have been employed to obtain selectivity of SiO_2 etching on Si, or by controlling the duty cycle of CHF_3 plasma generated by an electron cyclotron resonance (ECR) source.[98] Samukawa and Mieno[38] also reported highly selective, anisotropic, notch- and charge-free polycrystalline silicon etching by using the pulsed discharge. Charles and Boswell[93] used pulsed helicon diffusion plasma to control the deposition rate of SiO_2.

Various diagnostic methods have been applied to characterize pulsed RF and ECR discharges; they include mass spectrometry[99], optical emission spectroscopy,[100] ion energy analysis,[80,101] and Langmuir probe techniques.[102-104] A global model approach[105] was employed in order to determine the time constants of plasma ignition and decay associated with pulsed RF discharges.

Ion energy distribution functions (IEDF) have mostly been evaluated in RF plasmas in the context of reactive ion etching and the reduction of device damage in microelectronics.[98] However, little attention has so far been paid to the analysis of IEDF in MW discharges used for other types of materials processing.[97,55,106-108] Furthermore, many laboratories routinely use commercially available MW power supplies working in continuous wave (*cw*) or pulsed modes, but the effect of power delivery mode on the ion bombardment characteristics has not been well studied so far.

In our previous work, we have shown that the flux and energy of ions impinging upon an exposed surface can be selectively controlled in the MW/RF mode.[36,97,106] In addition, we have frequently used both the single-mode MW and the dual-frequency MW/RF plasmas for surface modification of polymers for adhesion enhancement.[94,108,109] In the present work, we study the effect of pulse frequency and pulse length on the IEDF in such MW plasmas at the discharge conditions similar to those used for surface

treatment of polymers. We further discuss a method to obtain characteristic plasma transition times from the analysis of the measured IEDFs.

5.2.2 Experimental methodology

The experiments were performed in a MW plasma system consisting of a cylindrical stainless steel vacuum chamber (30 cm in diameter), equipped with a grounded aluminum substrate holder (18 cm in diameter) and a fused silica window (30 cm in diameter).[94-96] MW (2.45 GHz) power was applied from a periodic slow-wave applicator (25 cm long), using either one of two different MW power supplies: (i) a Muegge (model M1200) generator, operating in continuous wave (cw) or pulsed modes, with the pulse frequency, f_p, varied from 1 to 10 kHz; (ii) a Hüttinger (IGM1/2450) "high-ripple" generator, with a fixed pulse frequency of 60 Hz. Prior to the experiments, the vacuum chamber was turbo-molecularly pumped to 1×10^{-4} Torr, following which a gas flow of 5 – 20 sccm was introduced, and a pressure between 50 and 200 mTorr was adjusted. Most of the results reported here were obtained with argon, but data for nitrogen and helium are also presented.

A differentially pumped, retarding field ion energy analyzer (Figure 5.3) was placed in the center of the substrate-holder electrode. The entrance orifice (250 μm in diameter), drilled in a stainless steel foil (140 μm thick), combined with an effective pumping speed of 18 l/s in the analyzer section, assured a three orders of magnitude lower pressure in the analyzer zone, compared with that in the reactor. This provided a collision-free passage of ions through the analyzer (~1 cm) for all the reactor pressures investigated. The analyzer consists of three parallel nickel grids, and a Faraday cup as the collector. Each grid comprises 90 lines per inch, and has a transparency of 88%. All analyzer electrodes are separated by 2 mm gaps. Negative potentials, V_1, applied to the first grid, and V_3, applied to the third grid, form a potential barrier for plasma electrons and for secondary electrons, respectively. A positive scanning potential, V_s, is applied to the central grid, allowing only ions with energy higher than ZeV_s to be collected, where

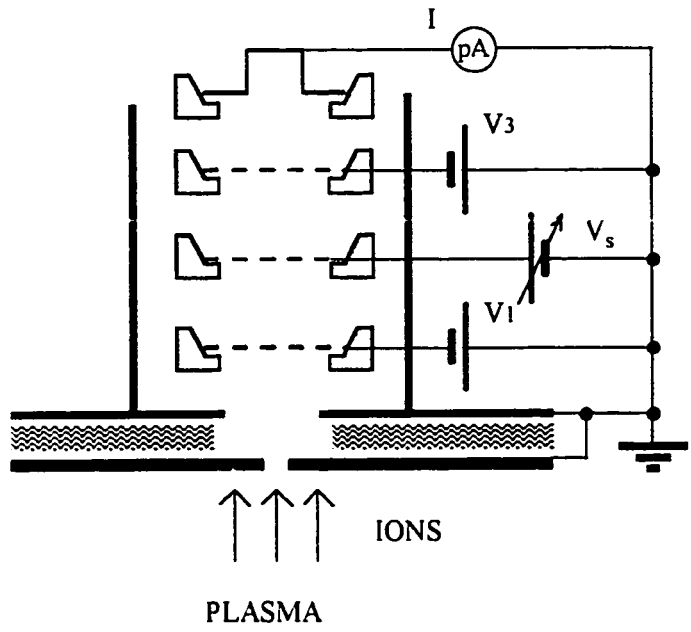

Figure 5.3 Schematic illustration of the ion energy analyzer.

Ze is the ion charge. A computer-controlled voltage source / picoammeter (Keithley 487) was used to measure the collector current *I*. First derivative of the $I(V_s)$ dependence gives the ion energy distribution:[80]

$$f(E) = \frac{M_i}{A_a T_a Z e^2} \frac{dI(V_s)}{dV_s} \tag{5.1}$$

where M_i is the ion mass, A_a is the entrance orifice area, and T_a is the total transparency of the analyzer. The integration time of the picoammeter was 16.7 msec for each reading, and 12 measurements were averaged to obtain one I-V curve. For example, in the case of f_p = 1 kHz, each point on the IEDF curve represents averaging over about 200 discharge pulses. This maintains a low signal/noise ratio, and it makes the synchronization of measurements with power pulses unnecessary.

The floating potential was measured by an electrostatic probe formed by a 1 cm long, 0.5 mm diameter tungsten wire placed in the central region of the plasma. The probe was connected to a Kikusui 20 MHz oscilloscope (1 MΩ, 25 pF entrance).

5.2.3 Experimental results and discussion

5.2.3.1 IEDFs in the MW plasma exited by a low-ripple generator

The form of the pulsed MW power signal is schematically illustrated in Fig. 5.4(a). Rectangular MW pulses are characterized by a pulse frequency $f_p = 1/(T_{on}+T_{off})$. During the time T_{on} , the MW power attains its maximum value P_{on}, while during the time T_{off} the power delivered is zero. The duty cycle D is defined as $T_{on}/(T_{on}+T_{off})$, and the average power, P_{av}, can be calculated as $P_{on}D$. The floating potential, V_{float}, measured by the electrostatic probe, is depicted in Figure 5.4(b). It has a constant value V_{on} during the period T_{on} (after a short transient spike period, T_s, of about 20 μs), then it drops sharply to V_{off} at the end of the pulse, and it further decreases very slowly. The ion current, $I(t)$, increases during the T_{on} period with a characteristic time constant τ_1 to a value I_{max}, and then decreases to I_{min} during the T_{off} period with a characteristic time τ_2. I_{cw} is the value corresponding to a saturated ion current for infinite T_{on} (*cw* mode).

IEDFs measured in pulsed MW plasma in argon are shown in Figure 5.5. Ion energies do not exceed 10 eV for all presented spectra. We found that the IEDF for the *cw* MW plasma consists of a single peak, with a characteristic low-energy tail. The "tail" feature is due to ion-neutral collisions in the sheath. The shape of the distribution changes substantially when pulsed MW power is used. A second peak appears on the low-energy side of the IEDF when D is decreased. As this peak becomes more pronounced for low values of D, we associate it with ions arriving during the T_{off} period. Low energies of ions forming this peak reflect the low plasma potential in the post discharge. In addition, a weak feature appears on the high-energy side of the distribution, presumably due to the ions formed during the period of the transient spike, T_s. Such spike was observed by oscilloscope measurements of V_{float}. Similar three-peak structure of IEDF was also described by Charles and Boswell[93] for a pulsed helicon RF plasma.

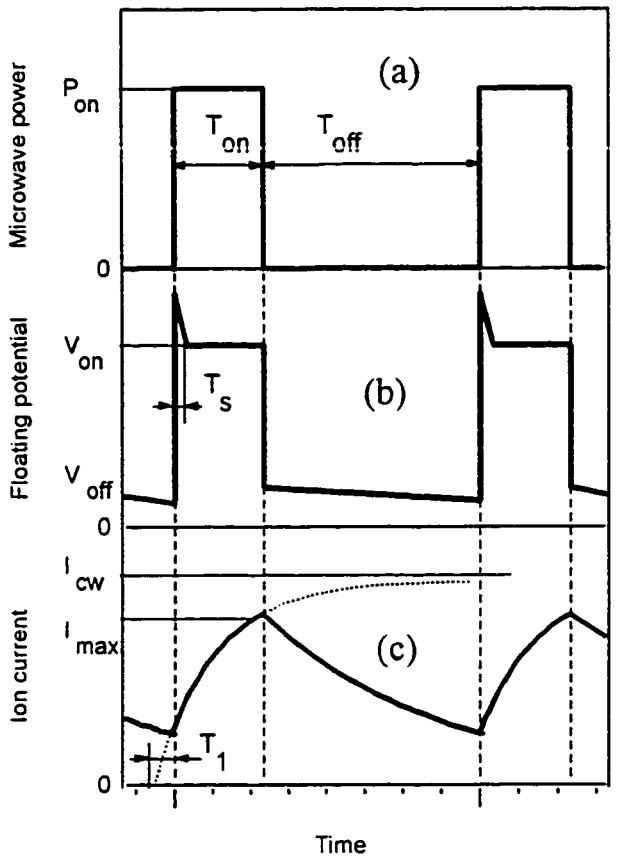

Figure 5.4 Schematic illustration of the time evolution of plasma parameters in the pulsed MW discharge: a) transmitted MW power, b) floating potential, c) ion current on the grounded substrate holder.

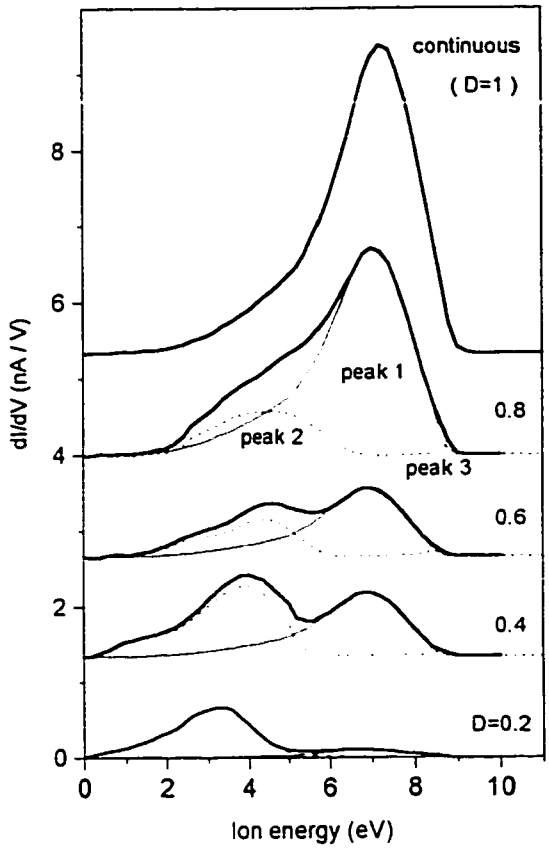

Figure 5.5 Ion energy distribution function (IEDF) from a pulsed MW plasma in argon for different values of duty cycle, D. The Ar pressure was 100 mTorr, the MW peak power 960 W, and the pulse frequency 1 kHz. The curves are shifted for clarity.

One can deduce the intensity of the low-energy peak by subtracting the *cw* mode peak, normalized to the maximum intensity, from the overall distribution in the pulsed mode. In so doing, we suppose that the conditions for ion extraction during the T_{on} period are the same as in the *cw* mode. The procedure is the following: The high-energy peak is fitted by a curve with a shape corresponding to the *cw*-mode IEDF of an appropriate height (peak 1 in Figure 5.5). This curve is then subtracted from the total IEDF, resulting in the peak 2 in Figure 5.5. Integration of these curves gives the number of ions arrived at the collector per pulse:

$$N_i = \frac{T_{on} + T_{off}}{Ze^2} \int \frac{dI_i}{dV} dE, \tag{5.2}$$

where the index $i = on$, *off*, or *tot* for peak 1, peak 2, or the entire IEDF, respectively.

Analysis of the IEDFs, presented in Figure 5.5, shows that N_{tot} (integrated area under the entire IEDF) and the intensity of the high-energy peak (N_{on}, peak 1) monotonically increase with D, while the low-energy peak area (N_{off}, peak2) exhibits a maximum around $D = 0.5$ (Figure 5.6). The intensity of peak 1 is lower than what one would expect from the simple $I_{cw}D$ product. The reason is that during a transition time, required to reach the saturation, the ion current is lower than I_{cw} [Figure 5.4(c)]. On the other hand, addition of low-energy ions during the time T_{off} contributes to the total flux, N_{tot}, which is higher than $I_{cw}D$, while $\tau_1 < \tau_2$. As a consequence, for $D \sim 0.5$ the total flux in Figure 5.6, normalized to the same average power (simply divided by D), is higher than that for the cw mode. A similar effect was also observed by Ashida et al.[104] for the inductively coupled RF plasma.

The mean energy of each peak and for the total IEDF were calculated using the relationship:

$$\bar{E}_i = \frac{\int E \cdot f_i(E) dE}{\int f_i(E) dE}. \tag{5.3}$$

As illustrated in Figure 5.7, the mean ion energy corresponding to the T_{on} period, $\bar{E}_{on}$, only slightly rises with D. This indicates that the plasma potential rapidly saturates, and

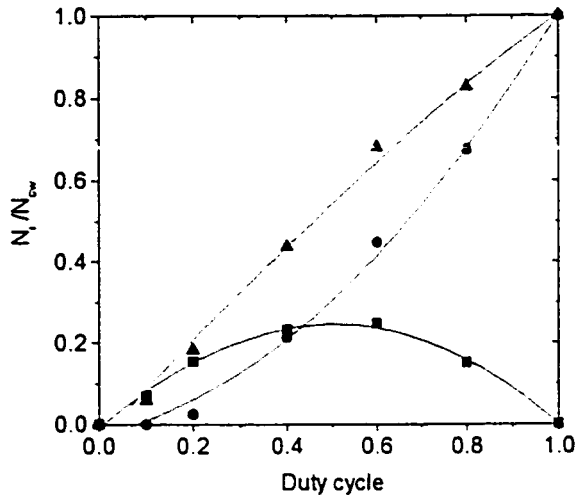

Figure 5.6 Normalized number of ions N_{on}/N_{cw} (●), N_{off}/N_{cw} (■), and N_{tot}/N_{cw} (▲) as a function of duty cycle for the IEDFs from Figure 5.5.

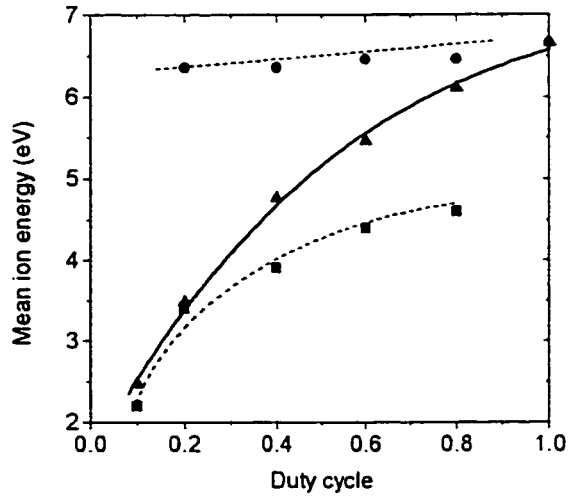

Figure 5.7 Mean ion energies $\bar{E}_{on}$ (●), $\bar{E}_{off}$ (■), and $\bar{E}_{tot}$ (▲) as functions of duty cycle for the IEDFs from Figure 5.5.

remains constant during T_{on}. The $\bar{E}_{off}$ values increase with D. This is in agreement with the fact that V_{float} decreases slightly during the T_{off} period; as a consequence, the average V_{float} value is lower when T_{off} is longer. The total average ion energy, $\bar{E}_{tot}$, determined from the complete IEDF (Figure 5.7), decreases with decreasing D, as peak 2 becomes more pronounced (see Figure 5.5).

We found a relatively small effect of f_p on the IEDF within the range from 1 to 5 kHz (see Figure 5.8). The main changes in the IEDFs are the presence of a more pronounced high-energy tail at high f_p values, and a slight shift of $\bar{E}_{off}$.

We have seen above that in the pulsed mode in argon plasma, the IEDF can be deconvoluted into three contributions, namely the central peak due to the ions arriving during the T_{on} period (peak 1), the low-energy peak associated with the ions arriving during the T_{off} period (peak 2), and the high-energy contribution (peak 3) due to the initial spike. This behavior holds for all gases we have investigated, however, several differences have been noted. The floating potential in nitrogen plasma is generally higher than that in argon (12 V and 7.5 V, respectively, at 200 mTorr). Furthermore, peak 3 is more pronounced in N_2 under the same nominal plasma conditions (see Figure 5.9). A very low T_{on} value (low D) leads to a substantial intensity decrease of peak 1 around 12 eV, indicating that only ions from the initial spike (peak 3) and from the plasma decay period (peak 2) are the main contributors to the energy spectrum. This effect is related to a longer initiation time for nitrogen, confirmed by oscilloscope measurements. Peak 2 shows the same behavior as in argon, becoming more pronounced when D decreases. The observed negative values of ion energy probably result from parasitic charges, which may have accumulated on the oxidized orifice and grid surfaces.

As shown above, the shape of the IEDF can be controlled by the pulsed-plasma characteristics, and the mean ion energy can be adjusted by an appropriate choice of the duty cycle. This type of approach appears attractive for selective surface treatment of polymers, for which the typical bond energies (3-6 eV) are situated in the same range.

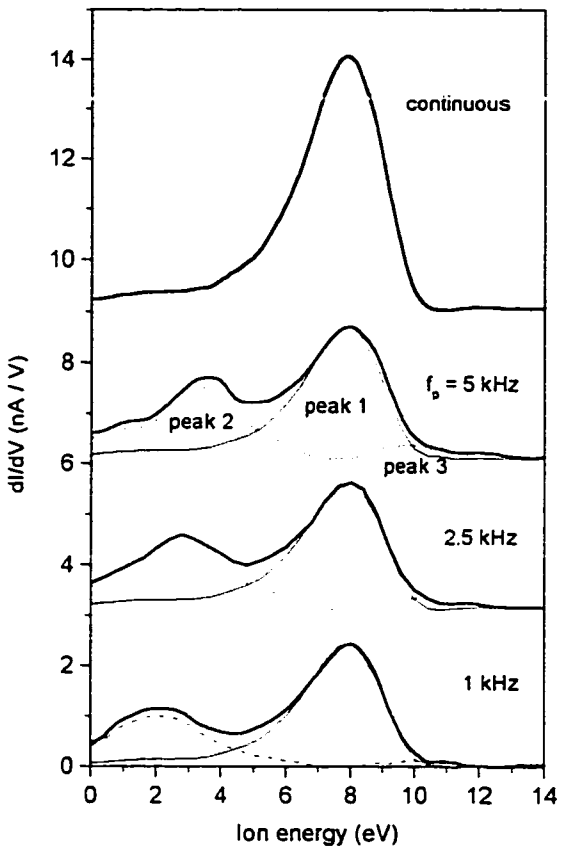

Figure 5.8 IEDFs from argon plasma for different pulse frequencies, f_p. The duty cycle was 0.5, Ar pressure 200 mTorr, peak power 700 W. The curves are shifted for clarity.

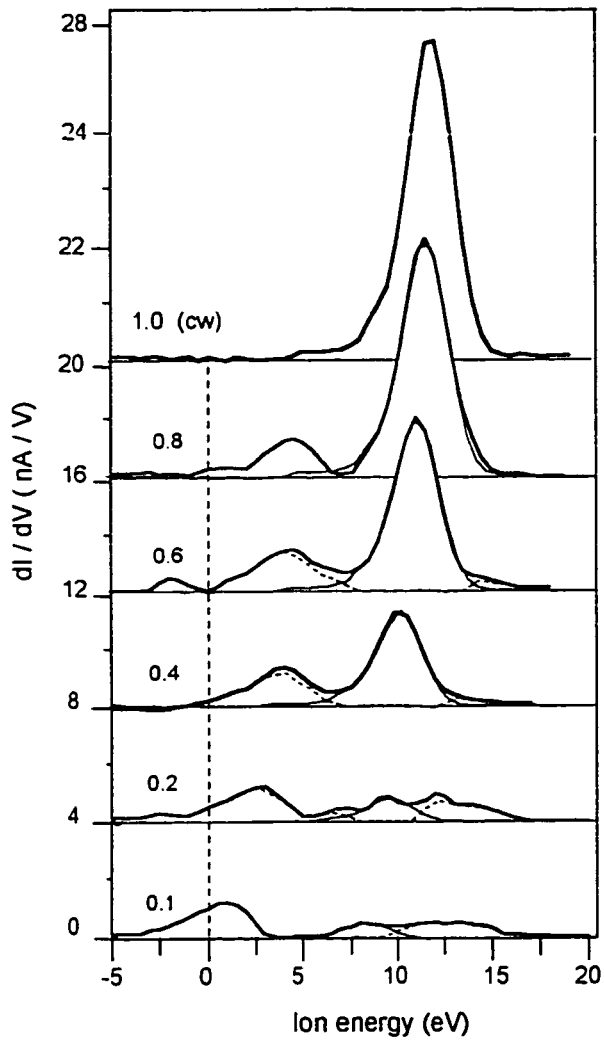

Figure 5.9 IEDFs from nitrogen plasma for different values of duty cycle. N_2 pressure was 100 mTorr, MW peak power 1200 W, pulse frequency was 1 kHz. The curves are shifted for clarity.

Indeed, we have recently reported a stronger effect on surface restructuring of polymers for the case of higher D values.[107]

5.2.3.2 IEDFs in the MW plasma exited by a high-ripple generator

The high-ripple MW generator (Hüttinger) provides a "rectangular" MW pulse, possessing a rounded top [see Figure 5.10(b)]. This leads to a modulation of the floating potential during the T_{on} period. This particular power supply did not allow independent control of D or P_{on}, since both these parameters increase with increasing power. In this set of experiments, D ranges from 10% to 15%, while the f_p is fixed at 60 Hz. This power supply was used in most of our earlier studies on polymer surface treatment and plasma depositions,[36,95-97] and similar power sources are frequently used in industry. Based on the foregoing, the pulse mode of this generator can explain the bimodal shape of the IEDFs observed in our earlier work.[97]

Using this high-ripple generator, we studied the behavior of V_{float} in different gases, namely Ar, N_2, and He [see Figure 5.10(a)]. For T_{on} of about 2 ms, the floating potential decays for 3-4 ms. The resulting IEDFs were found comparable with those obtained for the first (Muegge) generator, when D=0.4 was adjusted. All measured IEDFs possess a bi-modal structure, and their typical forms are shown in Figure 5.11. Similar to the results described above, the $\bar{E}_i$ values are higher in nitrogen than in its counterparts, but the current is generally lower, due to a lower plasma density. This lower density can be explained by the presence of additional channels of non-ionizing electron energy loss in a molecular gas discharge (dissociation, vibration etc.).[55] The plasma potential in He plasma is slightly higher than in Ar, and the small mass of He ions gives rise to the observed higher ion flux compared with argon.

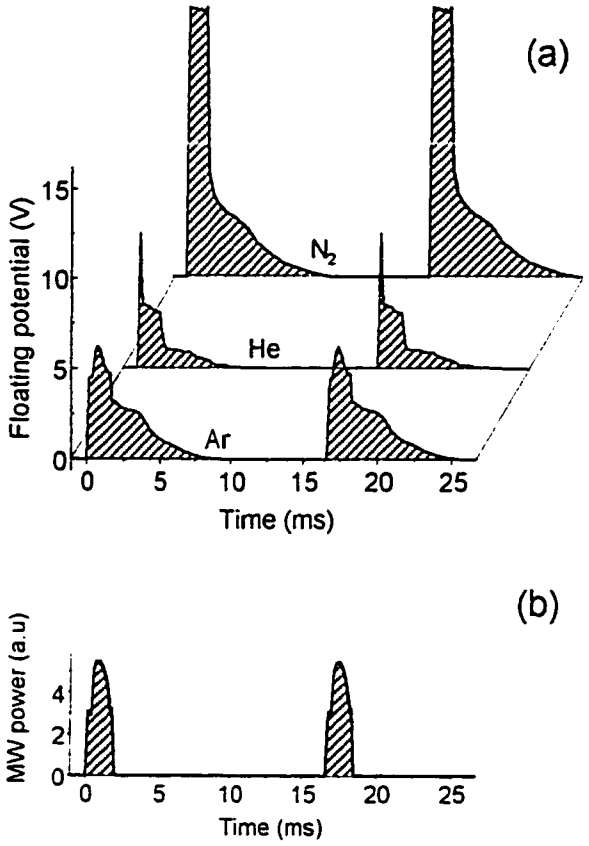

Figure 5.10 a) Floating potential vs. time in different gases at nominally identical conditions: pulse frequency 60 Hz, MW power 200 W, pressure 200 mTorr. b) Microwave pulse shape.

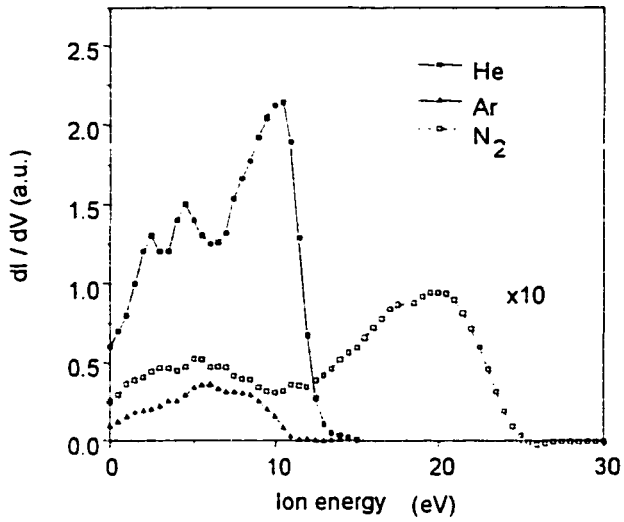

Figure 5.11 IEDFs for different gases. Plasma conditions are the same as in Figure 5.10

5.2.4 Global model analysis of the IEDFs

We have used the global (volume-averaged) model[105] approach to analyze the IEDFs obtained for different modes of operation. In the following, we describe a simple model which allows one to determine the characteristic rise time, τ_1, and decay time, τ_2, from a set of time-averaged IEDFs.

For f_p = 1 kHz, the time over which of the electron temperature stabilizes is much smaller than the pulse period; we can consider that changes in the electron temperature intimately follow the MW power pulses. The ion current $I(t)$ arriving at the orifice is given by:[105]

$$I(t) = en_s u_B A_a = en_s(t)(eT_e(t)/M)^{1/2} A_a, \tag{5.4}$$

where n_s is the ion density at the sheath edge, u_B is the Bohm velocity, T_e is the electron temperature, and M is the ion mass. Consequently, in the case of a constant electron temperature (e.g. during the T_{on} period), the ion current depends only on the plasma density. Therefore, exponential growth and decay of the plasma density[104] are followed by proportional changes in the ion current. The ion current during the T_{on} period, $I_{on}(t)$, can be described by an exponential relationship:

$$I_{on}(t) = I_{cw}(1 - e^{-\frac{t}{\tau_1}}), \tag{5.5}$$

as can the decay current during the T_{off} period:

$$I_{off}(t) = I_{max} e^{-\frac{t}{\tau_2}}, \tag{5.6}$$

where the symbols have been defined earlier. The time constants τ_1 and τ_2 characterize a balance between the creation of charged particles (ionization), and their loss (volume and surface recombination) during the corresponding period of time.

The total number of ions, N_{on}, which arrive at the collector during the time T_{on} can be expressed as:

$$N_{on} = \frac{1}{Ze}\int_{T_1}^{T_1+T_{on}} I_{on}(t)dt\,, \tag{5.7}$$

where T_1 is defined in Figure 5.4(c).

One can express the normalized number of ions arrived at the collector during the time $T_{on}+T_{off}$, using equation (5.5), and $N_{cw} = I_{cw}(T_{on}+T_{off})/e$:

$$\frac{N_{on}}{N_{cw}} = D - \frac{\tau_1}{T_{on}+T_{off}} \frac{\left(1-\exp(-\frac{T_{on}}{\tau_1})\right)\left(1-\exp(-\frac{T_{off}}{\tau_2})\right)}{1-\exp(-\frac{T_{on}}{\tau_1}-\frac{T_{off}}{\tau_2})}. \tag{5.8}$$

Similarly, during the T_{off} period

$$N_{off} = \frac{1}{Ze}\int_{T_{on}}^{T_{on}+T_{off}} I_{off}(t)dt\,, \tag{5.9}$$

which leads to

$$\frac{N_{off}}{N_{cw}} = \frac{\tau_2}{T_{on}+T_{off}} \frac{\left(1-\exp(-\frac{T_{on}}{\tau_1})\right)\left(1-\exp(-\frac{T_{off}}{\tau_2})\right)}{1-\exp(-\frac{T_{on}}{\tau_1}-\frac{T_{off}}{\tau_2})}. \tag{5.10}$$

The total yield, N_{tot}, is then determined as the sum of N_{on} and N_{off}:

$$N_{tot} = N_{on} + N_{off} = DN_{cw} + (1-\frac{\tau_1}{\tau_2})N_{off}\,. \tag{5.11}$$

Equation (5.11) shows that for the same average MW power, the total ion flux is higher in the pulsed mode than in the continuous mode when $\tau_1 < \tau_2$. In the case of very low f_p values, when $T_{on} >> \tau_1$, and $T_{off} >> \tau_2$, expressions (5.7) and (5.9) reduce to the obvious relations $N_{on} = DN_{cw}$ and $N_{off} = 0$.

The values on the left side of equations (5.8) and (5.10) are experimentally accessible, and they can be obtained from the measured IEDFs as described in Section 5.3.2.1. Now, by fitting the N_{on}/N_{cw} and N_{off}/N_{cw} data for known T_{on} and T_{off} with equations (5.8) and (5.10), we obtain the τ_1 and τ_2 values. The solid lines in Figure 5.6

represent such a fit, that yields $\tau_1 = 330$ μs and $\tau_2 = 410$ μs. We conclude from this that the characteristic times for plasma initiation and decay can be deduced without applying time-resolved techniques for measuring plasma parameters. However, our model does not take into account processes during the initial spike; we assume that T_{on} is much longer than T_s, which is the case for the range of f_p and D values studied here. Other simplifications are the following: (i) the electron temperature during the T_{off} period is assumed constant, while in reality it drops slowly but continuously. T_{off} is longer than the period of the fast decay of the electron temperature, but it is short enough so that the temperature changes during the slow decay are negligible; (ii) only one single type of ion is taken into account by the model, while in the real plasma several ionic species should be considered.

In general, the τ_1 and τ_2 values determined in this work are substantially larger than those reported in recent literature for RF plasmas.[103,105,110] Presumably, differences in experimental conditions are the main reason. The relatively high pressure in our case leads to a slower diffusion of charged species. Furthermore, the possible presence of impurities, such as oxygen and water vapor, contributes to the creation of negative ions by electron attachment, especially during the T_{off} period, when the electron temperature drops.[110] As a result, the characteristic times will be substantially longer than the values of $\tau_1 = 30$ μs and $\tau_2 = 61$ μs for argon at 5 mTorr in a RF plasma in a cylindrical reactor (radius = 15 cm, length = 7.5 cm) determined by Lieberman and Ashida.[105] In fact, $\tau_2 =$ 400 μs was reported for a helicon RF discharge using 2 mTorr of oxygen, where negative ions are responsible for reduced ambipolar diffusion.[93] We conclude that our model gives acceptable characteristic times; however, we plan to confirm our results by detailed time- and mass-resolved measurements.

5.2.5 Conclusions

In the present work we have successfully tested a three-grid ion energy analyzer for the evaluation of the ion energy distribution functions (IEDFs) in continuous and

pulsed microwave plasma, under conditions frequently used for materials processing. We found that pulsed-mode IEDFs consist of three distinct features: (i) a central peak, due to ions originating from the "power-on" period; (ii) a low-energy peak, due to ions arriving during the "power-off" period; and (iii) a weaker high-energy contribution due to ions generated during the short initial spike at the leading edge of each pulse. The relative ion current associated with these individual features depends on the duty cycle D and on the pulse frequency f_p. The results show that the mean ion energy increases with increasing D, and that the total ion flux, normalized to the same average power, is higher for the pulsed mode than for the *cw* mode. Similar behavior has been observed for different working gases, namely Ar, N_2, and He.

Global model approach has been used to analyze the measured IEDFs, from which we obtained the characteristic times of plasma ignition and decay, namely τ_1 = 330 μs and τ_2 = 410 μs respectively for argon at 100 mTorr.

Control of f_p and D can be used for a fine adjustment of the average energy of ions impinging upon an exposed surface. Such control can lead to a selective modification of the polymer surface structure, for example, for enhanced adhesion. These studies are presently carried out in our laboratory,[107] and they are being extended to the dual-mode pulsed microwave/radiofrequency plasma and to time- and mass-resolved analysis.

Acknowledgments

The authors wish to thank Professor M.R. Wertheimer, Dr. A. Hallil and Mrs. J.E. Klemberg-Sapieha for numerous fruitful discussions. We also acknowledge the expert technical assistance of Mr. G. Jalbert. This work was supported in part by grants from the Natural Sciences and Engineering Research Council (NSERC) of Canada and the Fonds pour la Formation de Chercheurs et Aide à la Recherche (FCAR) of Québec.

CHAPTER 6. IEDFs in dual frequency MW/rf plasma

The goal of the present chapter is to provide a complete analysis of ion bombardment in the complex scenario, namely the pulsed MW/rf plasma where time resolved measurements point to a time evolution of the discharge impedance (section 6.2). Before we do that, however, we first discuss our rf plasma measurements in comparison with other published work and we use them as a basis for understanding the fundamental processes in cw MW/rf plasma, for similar p and V_b values (section 6.1). The results presented in this chapter were obtained in the system II.

6.1 IEDFs in cw rf and MW/rf plasmas

6.1.1 IEDF structure in argon

In Fig. 6.1(a), we show the IEDFs of Ar^+ ions, measured at the rf-powered electrode in pure rf discharge for different p values. At high p, the high-energy portion of the distributions is depleted, due to increased ion collisions in the sheath. The IEDFs are structured, with multiple peaks, indicating significant charge-exchange collisions of the Ar^+ ions, while crossing the rf-modulated sheath. In a charge-exchange collision process, an ion transfers charge and a small amount of momentum to a neutral, creating a new (slow) ion with little energy normal to the electrode, and an energetic (fast) neutral from the original ion. Wild and Koidl[69] associated the peaks observed across the energy spectra to different phases of the rf cycle and ion positions in the sheath [see also Fig. 3.9(b)]. They also correlated the number of peaks in the energy distribution to the transit times of ions (the number of rf cycles required to reach the cathode).

In the dual mode MW/rf plasma, very high ion fluxes and energies can be achieved; this is to be expected from the high ionization rate of MW excitation, and high V_b values due to the rf excitation. In Fig. 6.1(b), the Ar^+ IEDFs, measured at the rf-powered electrode are depicted for different p values; they are seen to exhibit higher

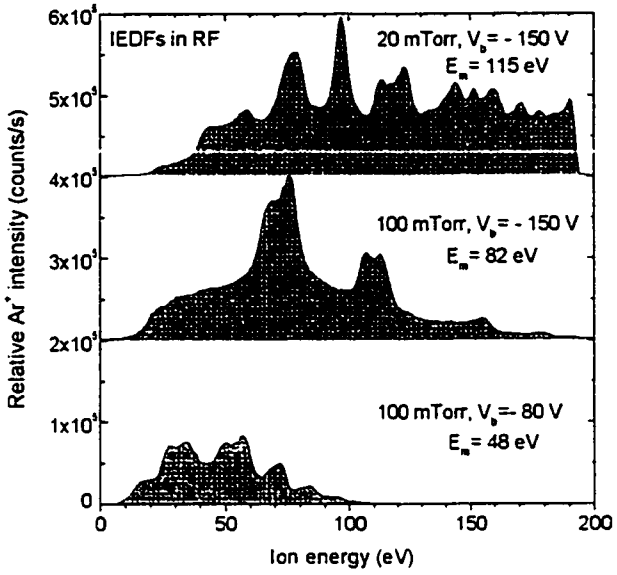

(a)

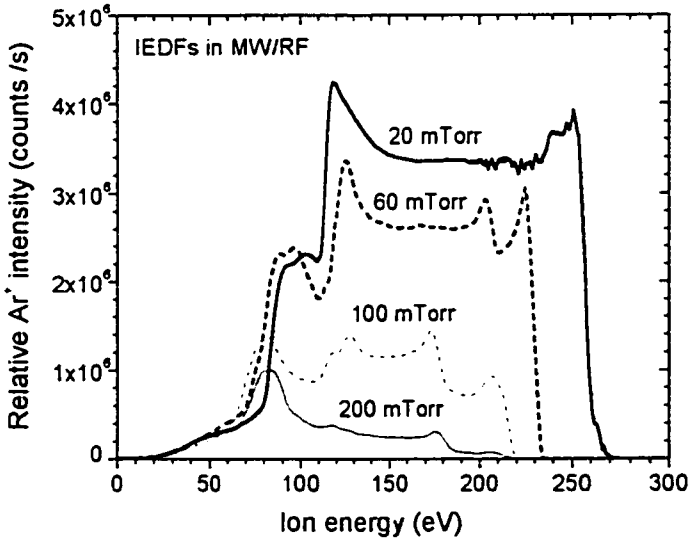

(b)

Figure 6.1 IEDFs of Ar^+ ions at the rf-powered electrode in argon: (a) in pure rf discharge, at different V_b and p values, and (b) in MW/rf plasma, using a MW power of 200 W and V_b = -150 V.

amplitudes than their simple rf counterparts. Their structured shapes are an indication of rf-controlled behavior of the MW/rf sheath. Notice here the clear saddle-Ar^+ structure at 20 mTorr, which is characteristic of a collisionless sheath (see Fig. 3.9a); for all examined pressures, the IEDFs contain more high-energy ions than in pure rf, and they are less structured, indicating a less collisional sheath.

The observed energy range of the IEDFs in MW/rf plasma is not simply $e|V_b|+eV_p$, as it usually considered for rf, but one must take into account the additional half width, $\Delta E/2$ determined by Eq. 3.29; this value is quite large due to the narrower sheath in high density MW/rf plasma (Eq. 3.21). The maximum ion energy, E_{max}, may then be expressed as follows:

$$E_{max} = e|V_b| + eV_p + \Delta E/2. \tag{6.1}$$

For comparison, in argon at p = 20 mTorr and V_b =-150 V, E_{max} = 170 eV in rf plasma, and 270 eV in MW/rf.

From the observed IEDF shapes, it is clear that the MW/rf plasma is not a simple superposition of the MW and rf components taken separately, but it posses new properties described above such as high ion bombardment energies. In the next section we continue to report our results from IEDF measurements, obtained now in nitrogen plasma for two most abundant ion species, namely N_2^+ and N^+.

6.1.2 IEDF structure in nitrogen

In nitrogen rf plasma, the IEDFs at the rf-powered electrode for the main ionic species, N_2^+ and N^+, are shown in Fig. 6.2(a). The N_2^+ IEDF is seen to exhibit similar features as its Ar^+ counterpart, indicating many charge-exchange collisions in the sheath between N_2^+ and N_2 species. On the other hand, the N^+ IEDF shows a simple saddle structure, characteristic of a collisionless rf sheath. Since N^+ ions undergo fewer collisions in the sheath than N_2^+ ions, the N^+ IEDF is depleted at low energy. Evidently, the observed differences in behavior between N^+ and N_2^+ ions result from the smaller

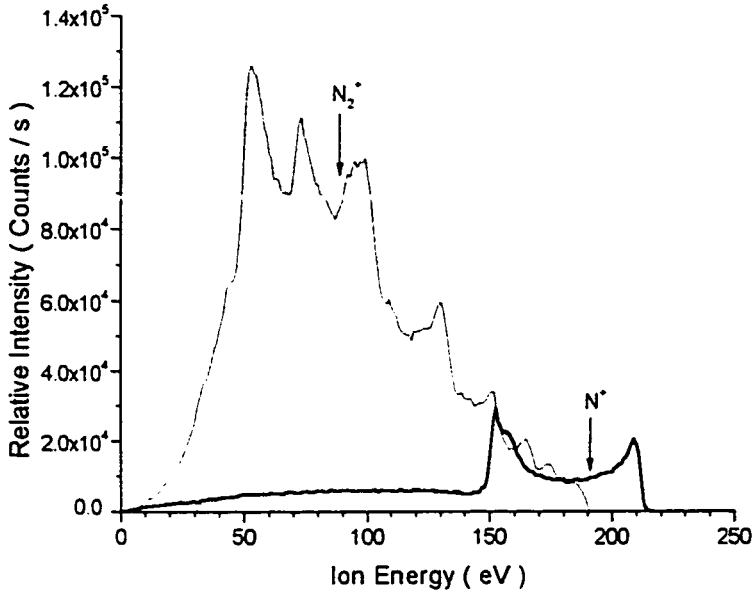

(a)

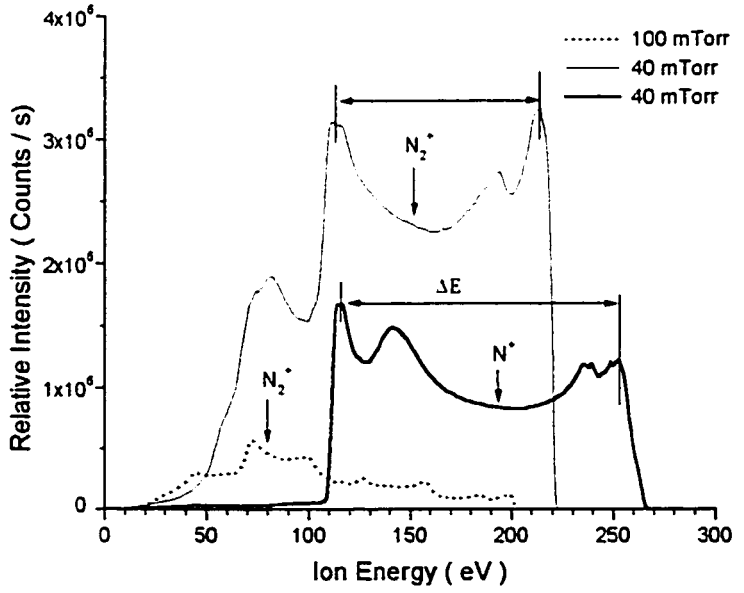

(b)

Figure 6.2. IEDFs of N^+ and N_2^+ ions at the rf-powered electrode in nitrogen: (a) rf-only discharge at a pressure of 40 mTorr and V_b = -150 V, (b) in MW/rf plasma, using a MW power of 300 W and V_b = -150 V.

probability of charge-exchange collisions between N^+ and the abundant N_2 molecules, compared with the relatively high probability of symmetric charge-exchange collisions for N_2^+ and N_2 pairs, the respective cross sections being 5×10^{-20} m^2 and 4×10^{-19} m^2 in the 1 to 10^3 eV ion energy range.[57]

At the grounded electrode in pure rf discharge, the IEDFs of N_2^+ and N^+ ions, depicted in Fig. 6.3, are seen to be single peaks with V_p (the peak center) in the range 14-16 V. The N_2^+ IEDFs show an extended tail of low-energy ions, in comparison with the N^+ counterparts, which result from collisions in the sheath. Again, due to the smaller probability of asymmetric collisions between N^+ and N_2, the N^+ IEDF is narrower and centered at V_p. In rf an extended tail of low-energy ions exists for the same gas pressure; this indicates higher s values in rf sheath mostly due to a lower n_e value (Eqs. 3.21 and 3.9).

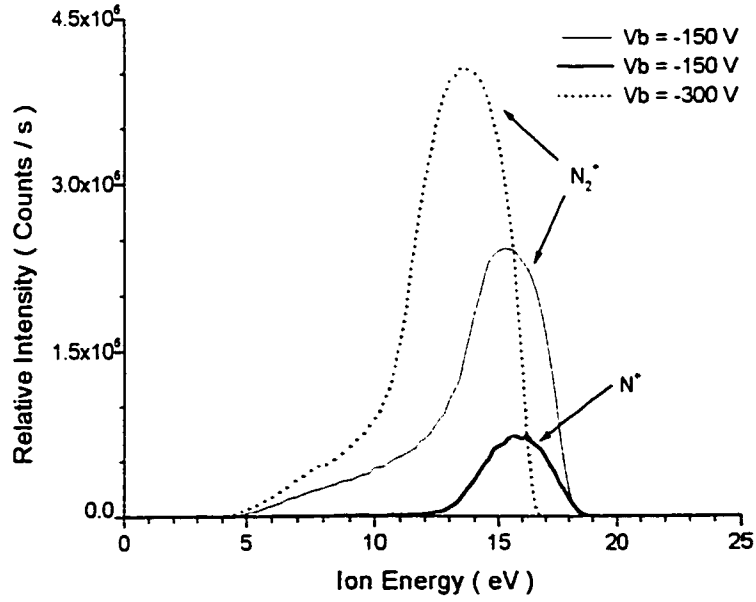

Figure 6.3. IEDFs of N^+ and N_2^+ ions at the grounded electrode in an rf nitrogen discharge at a pressure of 20 mTorr and for different V_b values.

Similar to the argon plasma, the N_2^+ and N^+ IEDFs in the dual-mode MW/rf plasma, (Fig. 6.2(b)) at the rf-powered electrode, for different p values but at a similar V_b parameter, show more high-energy ions than in "pure" rf, while the low-energy part is less structured. Higher ion energy is due to a narrower sheath, which results in fewer collisions and higher modulation during transit (see Eq. 3.29). Changes in sheath thickness can be anticipated from Eq. (6.1), considering the very large energy spread ΔE of N^+ ions in the MW/rf case.

6.1.3 Ion flux and mean ion energy

From the measured IEDFs we have obtained ϕ_i values by direct integration of IEDFs and $\langle E \rangle$ values from Eq. (5.3). Due to the similarities in the trends of Ar^+, N_2^+ and N^+ ions, and for simplicity, we discuss only one type of ion, Ar^+. From Fig. 6.4(a), ϕ_i at the electrode is seen to decrease steadily with increasing p for all plasma excitation modes, but the ϕ_i value is much higher in the MW/rf case than in rf, at the same p and V_b values.

The ϕ_i behavior in MW plasma can be explained if one takes into account the trends of kT_e and n_s, related to ϕ_i by Eq. (3.19). Using V_p (the center peak from Fig. 5.1) and Eq. (3.19), kT_e is estimated to decrease from 1.7 eV at 20 mTorr to 1.3 eV at 100 mTorr, contributing clearly to the ϕ_i decrease with rising p.

The value of n_s is expected to decrease with rising p, since the n_e gradient is higher at high pressure due to reduced diffusion. Indeed, n_s can be obtained using the solution of diffusion equation in the form:[55]

$$n_s \approx n_0\, 0.86(3 + d/\lambda_i)^{-1/2} \qquad (6.2)$$

where n_0 is a density near the quartz window, and $d \approx 10$ cm is a distance between the quartz window and the rf electrode. For Ar^+ the λ_i value varies between 1.5 mm at 20 mTorr to 0.3 mm at 100 mTorr [Eq. (3.8), $\sigma \approx 10^{-14}$ cm^{-2} (Ref. 55)]. Clearly, n_s becomes

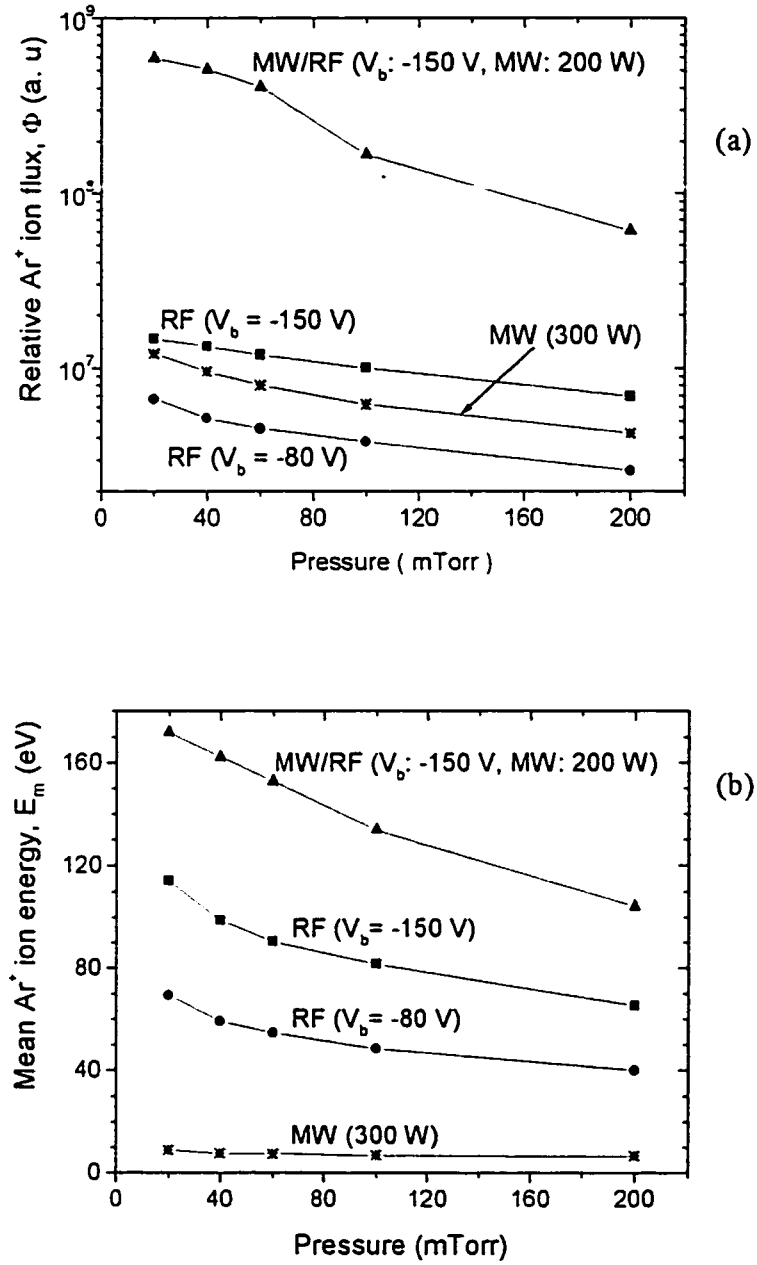

Figure 6.4. Relative Ar^+ ion flux, Φ, (a), and mean ion energy, E_m, (b) versus pressure in rf, MW and MW/rf plasmas.

two times lower at 100 mTorr compared to 20 mTorr, which is related to a decrease in ϕ_t with rising p. The value of n_0 may increase slightly with p, but as the MW power was kept constant near the quartz window, we believe that such change is less important in comparison with changes in spatial distribution of n_e.

In rf plasma, the measured ϕ_t values also decrease with pressure. In contrast to the MW plasma this is not due to the changes in n_s. In fact we found that n_s increases with p [111] as the ionization zone becomes localized near the rf electrode. We believe that such increase cannot be compensated by changes in kT_e alone, to yield the observed decrease of ϕ_t. Here, as in any collisional sheath, we must take into account the change in ion angular distribution due to collisions. As the acceptance angle of the EQP decreases with ion energy and becomes quite small (less than 3° for 30 eV ions),[112] only a small fraction of the total ion flux is analyzed at high pressure, where the ion angular distributions are broader. Thus, the measured decrease of ϕ_t does not mean the total ion flux reduction, but it represents the tendency for the ions with normal angle of incidence. Since in MW and MW/rf plasmas the sheath is almost collisionless, this effect is less important.

The $<E>$ parameter decreases with p for all plasma excitations, as depicted in Fig. 6.4(b). In rf and MW/rf modes this is due to the increase of collisions in the sheath at high p values, as shown by the IEDFs, which are rich in low energy ions. For similar p and V_b values, $<E>$ is much higher in MW/rf, due to the decrease of s, leading to less energy lost by ions during transit.

In MW plasma, the slight decrease of $<E>$ is mainly linked with changes in kT_e but not with sheath collisions, which are believed to be insignificant, considering the symmetrical shape of the IEDFs (see Fig. 5.1).

As a consequence, the MW/rf plasma, possessing simultaneously high ion fluxes and energies, is a very suitable plasma source for hardening and densification of deposited coatings,[35] due to the ion-induced effects described in Chapter 1.

In the next section we present an article submitted to the Journal of Applied Physics, where we study effect of pulsing of the MW signal on the properties of MW/rf plasma.

6.2 Time-resolved measurements of ion energy distributions in dual-mode pulsed-microwave/radio frequency plasma

O. Zabeida, A. Hallil, M. R. Wertheimer, and L. Martinu*

Groupe des Couches Minces (GCM) and Department of Engineering Physics and Materials Engineering, Ecole Polytechnique, Montreal, QC H3C 3A7, Canada.

Article submitted to
Journal of Applied Physics
August 25, 1999

* Author to whom the correspondence should be addressed:

E-mail address: lmartinu@mail.polymtl.ca

Abstract

In the present work we systematically study the ion energy distribution functions (IEDFs) in argon discharges produced by a combination of pulsed (1-2 kHz) microwave (MW) and continuous wave (cw) radio frequency (rf) excitations. We show that the IEDFs for the pulsed MW discharges are structured, with individual features originating from different periods of the pulse. In the dual-mode MW/rf discharge, significant modulation of the self-bias voltage, V_b, during the MW pulse cycle is observed, which we attribute to changes in the plasma's impedance: We demonstrate that in the pulsed-MW / cw-rf mode the plasma impedance is highly resistive when the MW signal is on, while it is predominantly capacitive during the period between individual pulses. Using the measured time-evolution of V_b in combination with time-resolved measurements of individual ion species, IEDFs at the rf powered electrode at each instant of the MW pulse have been obtained. This approach is then used to reconstruct the total IEDF in such a pulsed-MW / cw-rf plasma in order to obtain the total energy delivered by the impacting ions.

6.2.1 Introduction

High frequency plasmas, namely radio frequency (rf, $f \geq 1$ MHz) and microwave (MW, $f \geq 300$ MHz) discharges, are frequently used in low-pressure plasma processing, such as in plasma-enhanced chemical vapor deposition (PECVD), reactive ion etching (RIE), and in surface modification[95,96]. Precise control of ion bombardment in such plasmas is increasingly important for optimizing the quality of materials and devices. In this respect, it is very important to be able to independently vary the ion energy (E_i) and the ion flux (Φ_i), in order to tailor the density, hardness, and stress of thin films[9,17,18,113], or the form of etched patterns[113], for example. To ensure such a selective control of E_i and Φ_i values, two approaches appear very attractive: (i) pulsed plasma, in which the ions originating from different periods of the pulse (time-on and time-off) possess different ion

energy distribution functions (IEDFs);[93,101,114] or (ii) dual-mode microwave / radio-frequency (MW/rf) plasma, in which MW excitation supplies a high-density plasma, while capacitively coupled rf power provides the desired ion bombardment energy[34,35,96,115-117].

Recently, pulsed low-pressure discharges have attracted a growing interest in the plasma processing community. Power modulation strongly diminishes powder formation in rf silane plasmas and has been shown to be beneficial for film quality[99,118]. Enhanced selectivity of SiO_2 etching on Si was obtained by controlling the duty cycle in CHF_3 pulsed plasma, generated by an electron cyclotron resonance (ECR) source[98]. Samukawa and Mieno[38] also reported highly selective, anisotropic, notch- and charge-free polycrystalline silicon etching, when using a Cl_2 pulsed ECR discharge. In our laboratory, pulsed MW plasma has frequently been used for the surface treatment of polymers for improved adhesion[94,95]. Charles and Boswell[93] used a pulsed helicon diffusion plasma to control the deposition rate of SiO_2. These latter authors reported a three-peak structure in the IEDFs of the pulsed rf helicon discharges, in contrast with a single-peak IEDF in cw plasma, where the two additional peaks were attributed to ions arriving during the instant of an initial "spike" in electron temperature (high energy peak), and during the period of plasma decay (low energy peak). Such behavior has also been observed by Zeuner et al.[101], who measured time-resolved IEDFs in pulsed, capacitevely coupled, rf plasma. More recently, Zabeida and Martinu reported similarly structured IEDFs, measured with a multigrid ion energy analyzer in a large volume pulsed MW plasma[114].

The MW/rf plasma approach has been used extensively for the fabrication of functional coatings (optical-, protective-, barrier-, and hard films)[17,35,43,44,119], and for etching polymers[120]. However, only few studies have so far focused on plasma diagnostics and ion behavior in such discharges[36,97]. In most of the previous experiments, ion bombardment effects were simply interpreted in terms of the substrate bias voltage[35], or the mean ion energy, determined using a multigrid ion energy analyzer[97]. When the MW discharge is pulsed, the characteristics of MW/rf plasma, such as the plasma impedance, the difference between the plasma potential (V_p) and the self-bias potential

(V_b), and hence the IEDF, strongly vary with time. As a consequence, evaluations based on average ion flux and ion energy delivered to the exposed surface may become inaccurate.

Objectives of the present work, are twofold: (i) to perform a detailed study of time- and mass- resolved ion energy distributions in pulsed-MW/cw-rf discharges frequently used for materials processing; (ii) to propose a methodology which allows one to determine the total energy delivered to the surface by ions originating from a pulsed plasma in which the plasma impedance and the sheath potential vary with time. We use an equivalent circuit model of the discharge[90] to help interpret the observed self-bias modulation, and finally, to reconstruct the total IEDF in this type of plasma. In this work, all experiments were performed in argon, so as to avoid possible complications arising from plasma chemistry, and to make a link with our previous measurements[97,114]. It should be noted, however, that the presented methodology is not limited to noble gases or one-ion-dominated plasmas; on the contrary, one can independently follow each of the ion species arriving at the surface from complex gas mixtures such as those used in modern plasma processing[99,121].

6.2.2 Experimental methodology

The experiments were performed in a dual-mode MW/rf plasma reactor, schematically represented in Fig. 6.5(a). The system was turbomolecularly pumped to a base pressure below 10^{-4} Torr, following which argon gas was introduced at a constant flow of 20 sccm. The gas pressure (fixed at 100 mTorr) was measured with a capacitive gauge (MKS Baratron) and controlled with an electronic throttling valve.

Pulsed or cw MW (2.45 GHz) power (from a Muegge model M1200 generator) was applied using a 20 cm long MW slow wave structure, through a 30 cm diameter quartz window. Two crystal power monitors were used to measure the forward and reflected power values (the average value, in the case of pulsing). In addition, the signal from the forward power meter was used to monitor the MW pulse shape with an

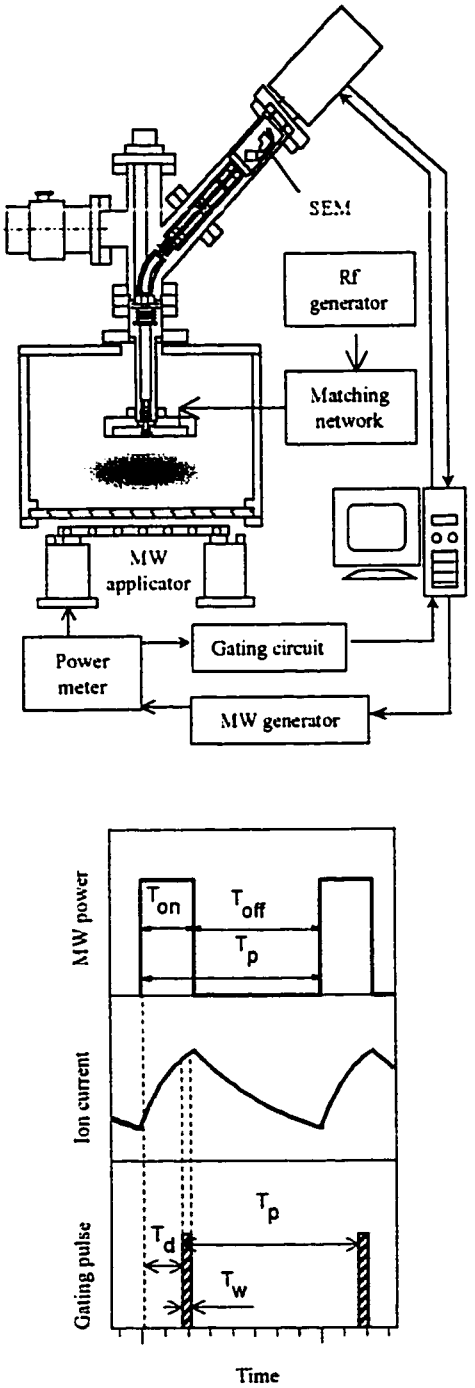

Figure 6.5. a) Schematic representation of the dual mode MW/rf reactor including the mass-spectrometer; b) illustration of the pulse gating.

oscilloscope, and as a reference for a gating pulse in the time-resolved measurements described below.

Cw rf power (13.56 MHz, 0 - 100 W) from the rf generator (Advanced Energy model RF-600) was applied to the top electrode to sustain the capacitively coupled discharge, the electrode being fixed at a distance of 10 cm from the quartz window The value of the negative self-bias potential (V_b) was measured by the voltmeter incorporated into the power supply. The shape and value of the V_b signal were also independently monitored with an oscilloscope, for the case of pulsed MW/rf plasma. An automatic L-type matching unit (Advanced Energy) was placed as close as possible to the reactor, in order to minimize power losses in the cables. A combined rf current- and voltage-probe (ENI), inserted between the matching unit and the vacuum feed-through, was used to carry out detailed plasma impedance and power dissipation measurements.

The IEDFs were measured using a Hiden EQP-1000 plasma probe, which consists of a quadrupole mass-spectrometer in tandem with an ion energy analyzer. Differential pumping allowed us to maintain the pressure inside the probe below 10^{-6} Torr during all experiments, which ensured collision-free transit of ions, and a proper functioning of the secondary electron multiplier (SEM). The ions, entering through a 50 μm diameter orifice in the center of the rf electrode, are selected by energy in the electrostatic deflector, then by mass in the quadrupole, following which they are counted by the SEM. The distance between the rf electrode and the extractor (the first electrode of the spectrometer, facing the rf electrode) was 5 mm.

Time-resolved measurements were accomplished by incorporating a gating circuit which supplies pulses of selected width and time-delay with respect to the MW pulse front [Figure 6.5(b)]. Only those ions arriving during the gating pulse were counted, and to assure adequate signal-to-noise ratio, counts were accumulated over a period of about 200 pulses. The time required for an ion to transit from the entrance orifice to the SEM (about 100 μs for Ar^+ ions) was taken into account when referring the IEDFs to the MW pulse front.

Two modes of scanning the ion energy are available on the EQP-1000 system: (i) the "energy potential" mode has a limited range (from -90 to +90 V) and minimum increments of 0.05 V; and (ii) the "reference potential" mode has a range of ± 1000 V, but with minimum steps of 1 V. We used mode (i) in pure MW plasma measurements (Section 6.2.3.1), while mode (ii) was selected in the MW/rf mode, where ion energies are considerably higher (Section 6.2.3.2). In the latter case, a negative potential of - 300 V was applied on the extractor, in order to ensure efficient sampling of low-energy ions. Since the "reference potential" is measured with respect to the system's ground, the measured distributions were shifted by an appropriate V_b value in order to obtain IEDFs on the negatively biased rf electrode.

6.2.3 Results and discussion

6.2.3.1. Pulsed MW plasma

Typical IEDFs measured in pulsed MW plasma in Ar are shown in Fig. 6.6 The IEDFs exhibit three specific features: (i) a central peak due to ions arriving during the MW pulse [T_{on} period, see Fig. 6.5(b)]; (ii) a peak at low energies due to ions arriving between individual pulses (T_{off} period); and (iii) a high-energy tail due to a short (~20 μs) initial spike of the plasma potential at the beginning of each pulse[93]. This structure agrees with our previous results, obtained with a mutigrid ion energy analyzer[114]. From Fig. 6.6, it is clear that this behavior is not particular to one type of ion, but it is common to all ion species arriving from the pulsed plasma.

One can note certain differences in ArH^+ (41 a.m.u.) and SiH^+ (29 a.m.u.) distributions, compared with those of the dominant Ar^+ ions: the IEDFs of the scarcer ion types are narrower, their two peaks are better resolved, and the maximum of the central peak is shifted to slightly higher energies. We attribute these differences to the fact that ArH^+ and SiH^+ ions undergo fewer collisions in the sheath than Ar^+ ions, which possess a large cross-section for the symmetrical charge-exchange interactions with neutral Ar

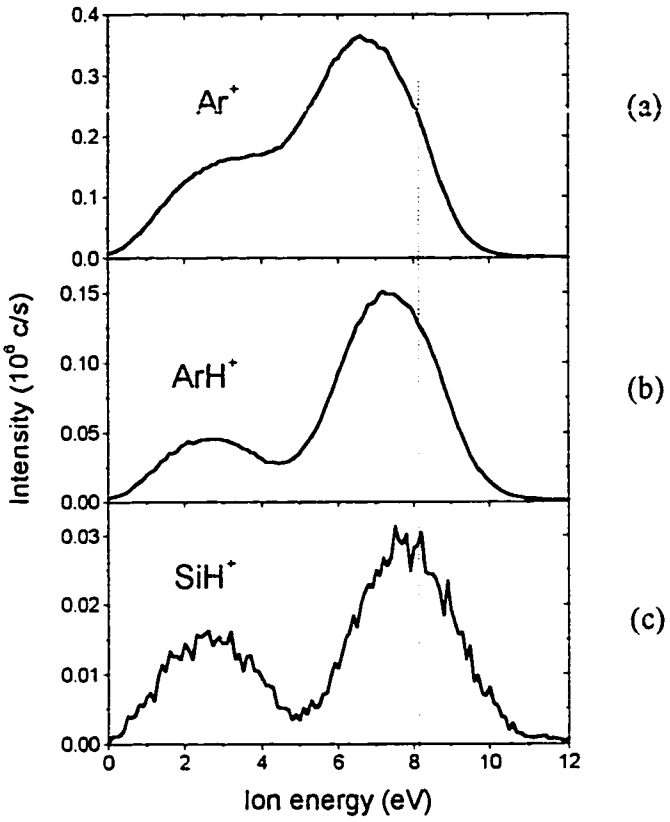

Figure 6.6 Time-averaged IEDFs from argon plasma for three different ion species: (a) Ar^+, (b) ArH^+, and (c) SiH^+ (M=29 m.a.u.). Peak MW power was 200 W, pulse frequency was 1 kHz, duty cycle was 0.3, and the Ar pressure was 100 mtorr.

atoms[57]. From this point of view, the plasma potential value of 8 V (position of the main peak maximum), obtained from the distributions of minority ions, would appear to be closer to reality than the 6.7 V value determined from the Ar^+ IEDF. We also observe different intensity ratios of low- to high-energy portions of the IEDFs among the different species, which may be due to differences in their creation and loss mechanisms.

In order to determine the time evolution of the IEDFs in pulsed MW plasma, we have sampled the ion flux at different moments of the MW pulse cycle. The results are shown in Fig. 6.7(a) for a pulse frequency of 2 kHz and a duty cycle of 0.3, the width of the gating pulse being 50 μs. Each of the IEDFs shown represents a measurement with a particular time delay between 0 and 450 μs, in steps of 50 μs. The IEDFs obtained during T_{on} (the first three from the top) have a single peak with a mean ion energy of 8.5 eV, and their shapes are very similar to that in the cw MW mode. At the end of the MW pulse (i.e. during T_{off}) the mean ion energy drops sharply to about 3 eV, and then remains constant, while the ion flux slowly decreases, as shown in Fig. 6.8 The experimental data points are shown fitted with two exponential functions, which represent the plasma build-up and decay[11], with respective time constants of 30 and 180 μs. These values are in good agreement with those reported by Boswell et al.[110], by Mieno et al.[103], and with those predicted by a global model of low-pressure discharges[105]. However, they are lower than those we determined earlier from time-averaged IEDFs (300 and 400 μs, respectively) in the pulsed MW plasma, when using our multigrid ion energy analyzer[114]. The differences may be due to changes in system geometry and, possibly, different impurity levels.

In order to obtain the time-averaged IEDF, we have summed the distributions over the entire MW pulse cycle [Fig. 6.7(a)], normalizing each contribution with respect to measurement duration. In Fig. 6.7(b) we compare this sum with the IEDF obtained from a single 100 ms measurement, of much longer duration than the MW pulse cycle (500 μs); the amplitudes and shapes of the two curves are seen to be very similar. This result confirms the validity of our time-resolved measurements, and our earlier-published

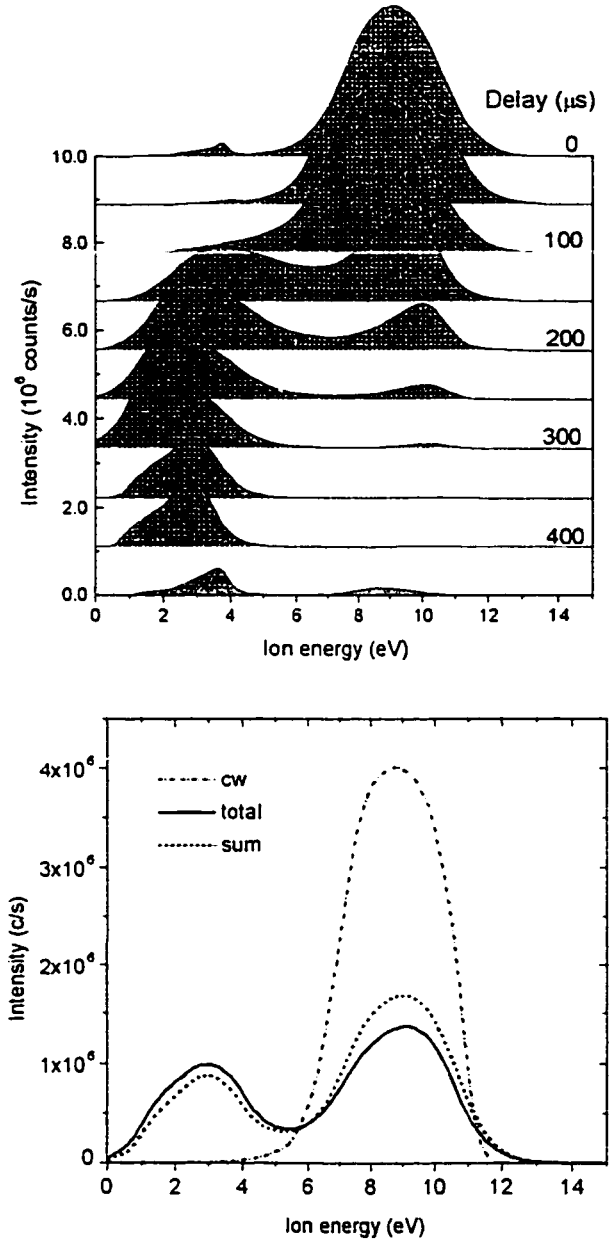

Figure 6.7 IEDFs of Ar^+ ions from MW plasma in argon: (a) time-resolved measurements; (b) cw (dash-dot line) and pulsed MW plasmas: the thin solid line represents time-averaged measurements and the dashed line is a sum of the distributions from (a). Gas pressure was 100 mtorr, pulse frequency was 2 kHz, duty cycle was 0.3.

interpretations of the IEDF structure[114].

Some of the distributions shown in Fig. 6.7(a) exhibit deviations from the expected single peak structure, namely a simultaneous contribution from the second peak, which we attribute to the noise in the gating circuit. Even if the time resolution of our setup was not high enough to clearly distinguish ions arriving from the initial spike, they are still seen to contribute to the high energy tail, as expected[114], when one compares the IEDFs from the cw and the pulsed plasmas [see Fig. 6.7(b)].

To summarize, the time-resolved measurements confirm that the double-peak structure of the IEDFs in pulsed plasma results from a superposition of (at least) two distinct contributions, one by ions arriving during the T_{on} period of MW pulses, the other by ions arriving between individual pulses. In section 6.2.3.2. we examine a more complicated plasma, in which pulsed MW and cw rf excitations are superimposed.

6.2.3.2 Pulsed MW/rf discharge

a. Self-bias modulation

A negative self-bias voltage, V_b, develops on the top electrode when rf power is superimposed on the MW discharge. In order to obtain the IEDFs at this electrode, measured distributions must be shifted by V_b. We found, however, that V_b is strongly modulated by MW pulsing, so that it is important to investigate its time evolution.

Figure 6.9 is an oscilloscope trace showing the variation of V_b during the MW pulse cycle. V_b rises to a high value (|-300| V) between MW pulses (i.e. during T_{off}), and drops to a low value (|-12| V) during the MW pulse (T_{on}). To clarify this, we have performed rf-probe measurements and impedance analysis, presented in Appendix 6.2.5. These show that when the MW power is switched on and off (at 1 kHz), the plasma impedance changes dramatically. However, since the automatic matching network is not fast enough to follow these changes, the circuit remains untuned part of the time, during which a substantial portion of the rf power is reflected back to the generator.

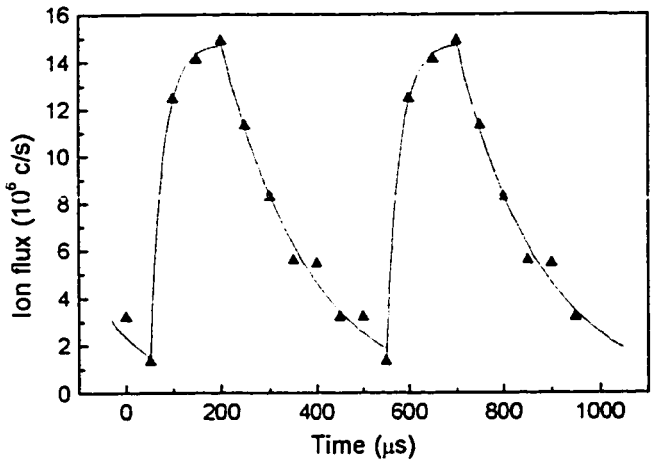

Figure 6.8 Time evolution of the ion flux. The points represent the experimental data from Figure 6.7, the lines are a result of fitting with exponential functions.

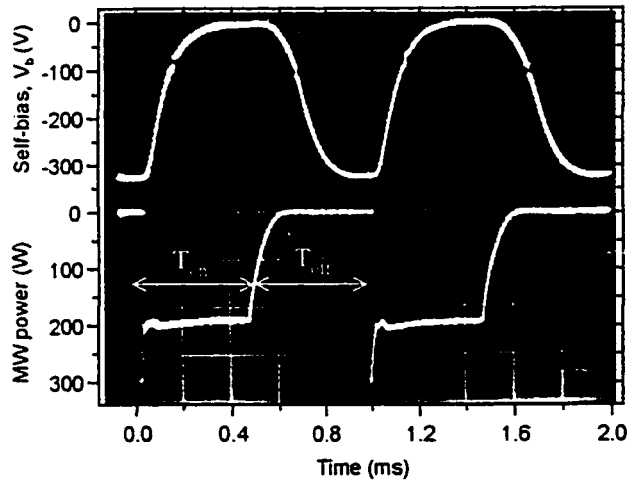

Figure 6.9 Rf self-bias evolution during the MW pulse (photo). The gas pressure was 100 mTorr, peak MW power was 300 W, pulse frequency was 1 kHz, and duty cycle was 0.5.

This finding is supported by other experimental observations: During all cw-mode measurements (rf or MW/rf) the impedance was automatically tuned by the matching network, resulting in an apparent reflected power below 5%. In contrast, in pulsed MW/rf plasma with the best possible matching, the reflected power (under the same conditions as in Fig. 6.9) was about 40% of the total rf power. For comparison, we have performed a series of rf-measurements when the pulsed and cw plasmas were matched manually, during which we noticed that in the automatic regime, the network matches the impedance only during T_{off}. Therefore, during T_{on} just a small part of the rf power is delivered to the discharge, resulting in a low rf peak-to-peak voltage, hence in the significant V_b modulation illustrated in Fig. 6.9. Obviously, this strongly affects the measured IEDFs at the rf electrode, the subject of the next section.

Additional comments are useful at this point: (i) Even if the matching network were fast enough to follow the MW pulse frequency, it would not totally eliminate the V_b oscillation, but would only reduce its amplitude: From Fig. 6.13(a) (Appendix 6.2.5) one notes that V_b is 3-4 times lower in the cw MW/rf mode than in a cw rf discharge at the same delivered power, as a result of the lower plasma impedance (but not 20 times lower, as observed in pulsed MW/ rf plasma). (ii) The oscillation is smoother at higher pulse frequencies (>10 kHz), when T_{off} is small compared with the plasma decay time. (iii) The average value of V_b measured by the generator (-150 V for the example shown in Fig. 6.9) gives no useful information about ion energy values.

b. IEDF measurements

The technique of time-resolved IEDF measurements can now be applied to characterize pulsed MW/rf plasma, for which the V_b evolution has just been discussed (section 6.2.3.2.a). Time-resolved scans of ion current vs. "reference potential" for such plasma, presented in Fig. 6.10(a), permit one to clearly distinguish two different types of

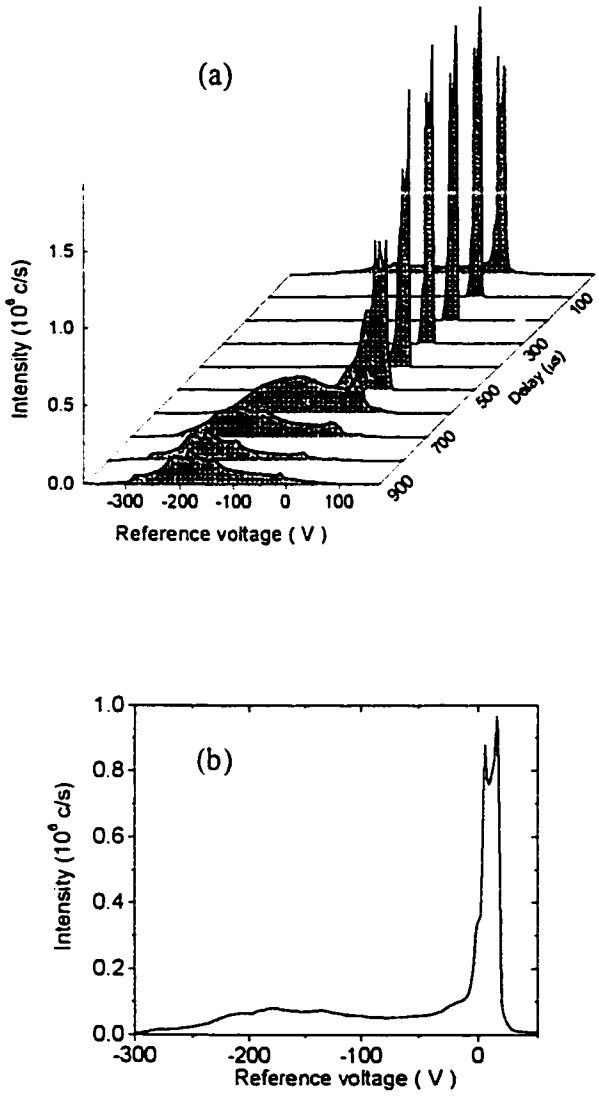

Figure 6.10 Ar^+ signal in pulsed MW/rf plasma as a function of "reference" potential: a) time-resolved distributions, b) averaged signal. Plasma parameters were the same as in Figure 6.9.

distribution: (i) a narrow, intense, saddle-shaped structure during T_{on} (delay times from 0 to 400 μs), and (ii) a broader, multi-peak distribution, due to ions arriving between two MW pulses (T_{off}, time delays 500-900 μs). Since V_b varies during the pulse cycle, the distributions shown in Fig. 6.10(a) must be shifted by the corresponding V_b value at any given time, in order to obtain the energy of ions impinging on the rf electrode surface at that time. We have used the data from Fig. 6.9 to do this: Figure 6.11(a) presents the instantaneous IEDF during T_{off}, along with that for cw rf plasma having the same V_b (-330 V), for comparison. The similarity in the the number of peaks and their amplitudes for the two distributions indicates that the sheath conditions (ions undergo the same number of collisions and gain the same energy) and plasma densities must be identical. This also proves that the choice of V_b value for the time-resolved IEDF is appropriate.

Figure 6.11(b) compares an IEDF taken during T_{on} with that of the cw MW/rf plasma, with V_b = -12 V. Both distributions are seen to have the same single saddle-shape peak, which indicates a collision-free transit of ions through the rf-modulated sheath[68], in contrast with the case depicted in Fig. 6.11(a). Once again, the same ion energies and peak amplitudes point to near-identical plasma parameters. We therefore conclude that the pulsed MW/rf plasma possesses the characteristics of a cw MW/rf discharge during T_{on}, and of a cw rf discharge during T_{off}. The transition periods between these two states may be more or less important, depending on the pulse frequency.

The instantaneous distributions were shifted by the appropriate corresponding V_b value, and resulting IEDFs are shown in Fig. 6.12(a): In the time-averaged IEDF [Fig. 6.12(b)] the contribution of ions arriving during MW pulses is easily distinguishable as an intense peak at a low energy, superimposed with a broad distribution from the cw rf part. Distributions in Fig. 6.12 allow us to evaluate the effect of ion bombardment at each moment of the MW pulse in MW/rf discharge, as well as the total effect. Some distributions in Fig. 6.10(a) (e.g. at zero delay) exhibit the features of different periods of the pulse (with different V_b) at the same time. Such mixed distributions were divided in two parts and each of these parts was shifted by an appropriate V_b value; these

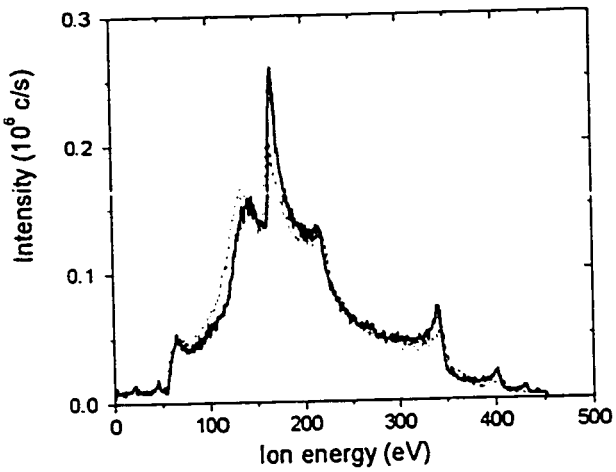

(a)

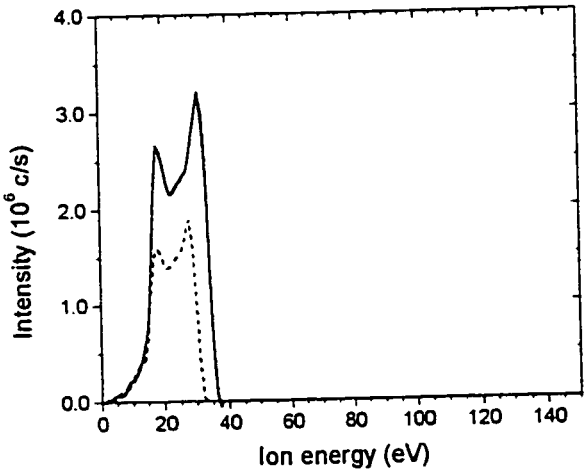

(b)

Figure 6.11 Comparison of instantaneous IEDFs from pulsed plasma (dashed lines) vs. cw plasma (solid lines): a) IEDF at a delay of 900 μs (see Fig. 6.10a) compared with an IEDF from cw rf plasma (V_b = -330 V); b) IEDF at a delay of 200 μs compared with an IEDF from cw MW/rf plasma (V_b = -12 V, MW power was 300 W).

(a)

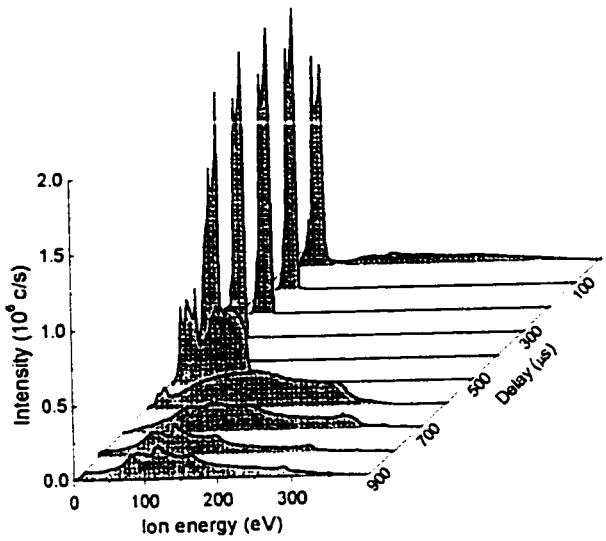

(b)

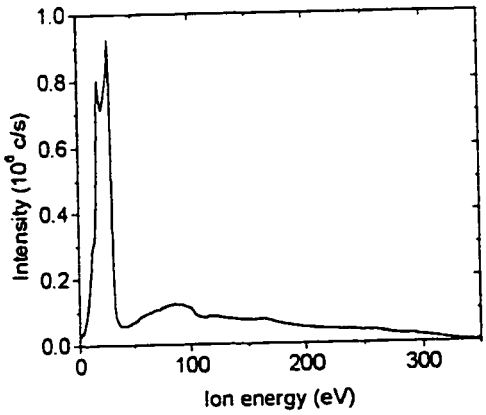

Figure 6.12 IEDFs in pulsed MW/rf plasma: a) time-resolved distributions, b) averaged signal. Plasma parameters were the same as in Figure 6.9.

manipulations are necessary in order to obtain the real IEDFs.

To summarize, systematic time-resolved measurements and evaluations of V_b are essential to avoid erroneous interpretations: for example, in our previous work[97], measured distributions equivalent to that in Fig. 6.10(b) neglected the effect of MW pulsing and V_b modulation.

6.2.4 Conclusions

We have systematically studied ion energy distributions in pulsed MW and MW/rf plasmas using time- and mass-resolved ion energy analysis. The main conclusions are as follows:

a) Two distinct IEDF features are clearly observed in pulsed MW plasma, namely (i) a peak with higher mean ion energy (6-8 eV) during the MW pulse (T_{on}), and (ii) a peak with lower mean ion energy (2-3 eV) during the period between pulses (T_{off}). The intensity of the latter decreases with time after extinction of the MW pulse. These observations confirm our previous assumptions about the origin of the structured shape of total (time-averaged) IEDFs in such plasmas[114].

b) Low self-bias voltage (V_b) values are observed in MW/rf plasma during T_{on}, while V_b sharply increases between pulses (T_{off}). This is believed to result from changes in the plasma impedance; equivalent rf circuit analysis supports this interpretation.

c) The ion energy in pulsed MW/rf plasma is modulated by oscillations of V_b. The IEDFs possess a narrow, low energy (a few tens of eV) saddle-shaped peak during the MW pulse (T_{on}), and they are much broader (several hundreds of eV), with multiple peaks, during the T_{off} period, as in the cw rf mode. The time-averaged IEDFs were obtained, which enable one to evaluate the total ion bombardment effects at the surface of an rf electrode.

The effect of V_b modulation, hence of the time-dependent IEDFs, is expected to occur also in other configurations of high-density, low-pressure pulsed plasma reactors, for example in inductively coupled plasma (ICP) systems, where pulsed rf power is

applied to the coil and cw rf power is applied to the substrate holder. These modulation effects must be considered when performing accurate ion flux and ion energy analyses.

Acknowledgments

The authors wish to acknowledge the expert technical assistance of Mr. G. Jalbert. This work was supported in part by grants from the Natural Sciences and Engineering Research Council (NSERC) of Canada.

6.2.5 Appendix: Impedance, and efficiency of rf power dissipation in MW/rf discharges

First, we address the electrical characteristics of continuous (non-pulsed) rf and MW/rf plasmas. A plot of V_b as a function of the applied rf power, P_{rf}, is presented in Fig. 6.13(a). For both plasma types $|V_b|$ is seen to increase quasi-linearly with P_{rf}, but its value is much lower in the case of the MW/rf plasma. The difference in slopes can be explained in terms of impedance; Figs. 6.13(b) and 6.13(c) summarize the results of rf probe measurements. The value of the reactor impedance, Z_R, [Fig. 6.13(b)] is very different for the two plasmas, the resistive component being higher and the capacitive one lower in the MW/rf plasma. Phase angle measurements provide further confirmation, as shown in Fig. 6.13(c): the phase angle has an almost purely capacitive nature for rf plasma (-89°) for all rf power values; in the MW/rf case it is lower, and varies strongly with rf power. This, of course, requires an appropriate tuning of the matching network in both cases.

As pointed out in Section 6.2.3.2.a, high reflected rf power, P_{ref}, (40%) is systematically observed in the case of pulsed MW/rf plasma. This is further clarified by an rf circuit analysis, comprising both the matching unit and the plasma reactor (Fig. 6.14). The matching network is represented by an inductor and a capacitor with pure reactive components X_L and X_C, respectively. The reactor impedance Z_R has a real (resistive) part, R_R, and a reactance X_R; it is composed of the plasma impedance, Z_P, and a stray

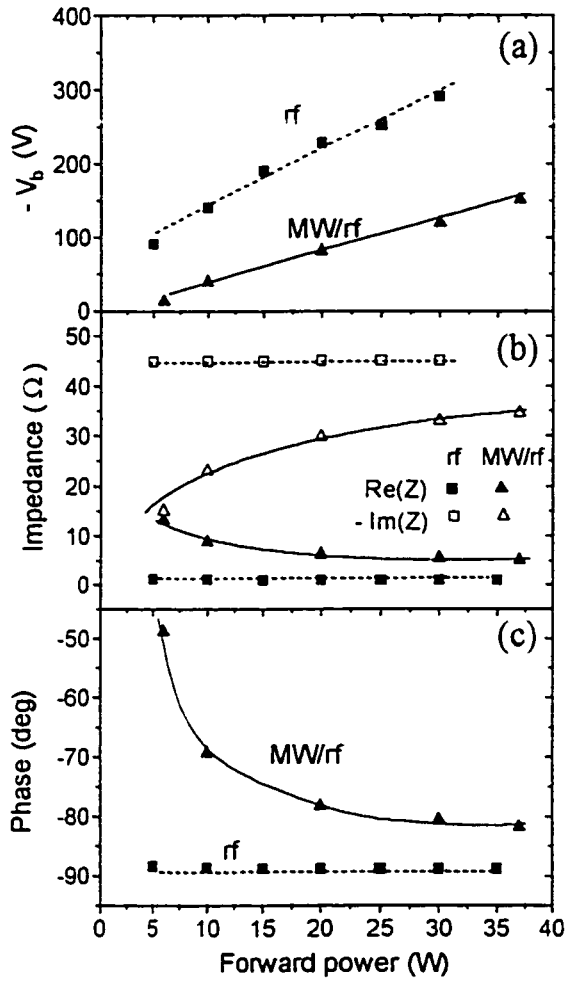

Figure 6.13 Electrical characteristics of the plasma reactor as a function of rf forward power in the cw rf (squares) and cw MW/rf (triangles) plasmas: (a) V_b, (b) reactor impedance, and (c) rf phase. The gas pressure was 100 mTorr, MW power was 300 W.

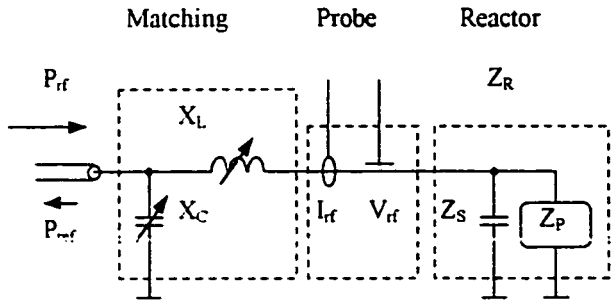

Figure 6.14 Rf circuit representing the matching network and the reactor impedance.

impedance, Z_S, in parallel:

$$Z_R = R_R + jX_R = (Z_P^{-1} + Z_S^{-1})^{-1} \tag{6.2}$$

The circuit performance can be evaluated in terms of the power reflection coefficient, Π:

$$\Pi \equiv P_{ref}/P_{rf} = \Gamma\Gamma^*, \tag{6.3}$$

where $\Gamma = (Z-R_0)/(Z+R_0)$ is a voltage reflection coefficient, $R_0 = 50\ \Omega$ is the line impedance to be matched, and Z is the impedance of the complete circuit (matching unit, reactor and plasma). For each value of Z_R, the X_L and X_C values necessary for perfect matching ($\Pi = 0$) are obtained from the following equations[122]:

$$(X_L + X_R)^2 = R_R(R_0 - R_R) \tag{6.4}$$

$$X_C = R_R R_0 (X_L + X_R)^{-1}. \tag{6.5}$$

Equations (6.3)-(6.5) enable us to calculate Π for the case when the network is tuned for a known value of Z_R, and following which Z_R is rapidly changed, the situation we believe to occur in the case of pulsed MW/rf plasma. This calculation is necessary, since our rf-probe does not permit direct time-resolved measurements of P_{ref}. As indicated by the IEDF measurements in Section 6.2.3.2.b, we suppose that during T_{on} the discharge has the characteristics (including the impedance) of a cw MW/rf plasma, while during T_{off} it behaves like a pure cw rf discharge. As an example, we select two extreme values of V_b in Fig. 6.9, and determine the corresponding Z_R^{rf} and $Z_R^{rf/mw}$ values from Figs. 6.13(a) and 6.13(b), the X_C and X_L values necessary for ideal matching being

calculated with Eqs. (6.4) and (6.5). To simulate pulsing conditions, we use the X_L and X_C values for the cw rf case, and replace Z_R^{rf} by $Z_R^{mw/rf}$. The power reflection coefficient in this case is obtained from Eq. (6.1); the same procedure is performed with the network impedance tuned to match $Z_R^{mw/rf}$, but coupled with Z_R^{rf}.

The results are represented in Table 6.1.: Z_P was calculated with the assumption that $Z_S = 0.2 - 50.8j\ \Omega$, obtained from rf probe measurements in the absence of plasma (at base pressure), does not change when plasma is ignited. This simplification appears justified, based on equivalent circuit models of rf plasma in the recent literature[23]. The

Table 6.1 Electric characteristics of the plasma reactor.

Excitation	Vb, [V]	Z_R, [Ω]	Z_P, [Ω]	X_C, [Ω]	X_L, [Ω]	Π (matching rf)	Π (matching MW/rf)
cw rf	-300	1-45j	96-430j	7.0	7.0	0	0.95
cw MW/rf	-12	13-15j	23-13j	2.2	2.9	0.92	0

results in Table 6.1. clearly indicate that when the matching network is well-tuned for cw rf plasma, it gives very poor performance (more than 90% of reflected power) for MW/rf plasma. Similarly, a well-tuned network for MW/rf plasma becomes inefficient in cw rf operation. In pulsed MW/rf plasma, this leads to poor rf power coupling during part of the MW pulse cycle, as we set out to prove.

CHAPTER 7. Ion energy characteristics in the cold cathode ion source system

In previous sections we descried the methodology of using the IEA and the EQP plasma probe for the characterization of complex high frequency discharges. In this chapter, we benefit from the ease of manipulating the IEA, and test it in a commercial IBAD system. In addition, we evaluate the effect of the derived ion energy characteristics on the properties of surface treated polymers or deposited optical coatings. This work was performed at Denton Vacuum LLC, Moorestown, NJ, on their Integrity-29 reactor during a short visit of the candidate. The dependence of the IEDFs on different working regimes of this ion source are important for determining its suitability for various process demands. From our point of view it was a good opportunity to test our IEDF measurement methodology in a completely different environment. Since in the IBAD reactor the ions are provided by a remote source, the effect of ion bombardment was expected to be separated from the effects of UV radiation and radicals, in contrast to direct plasma exposures.

This chapter consists of two published articles. Section 7.1 gives a comparison of the results for polymer treatment in the plasma and in the IBAD reactor, while Section 7.2 deals with the deposition of optical films and the variation of their properties with the ion bombardment energetics.

7.1 Effect of ion bombardment in polymer surface modification: comparison of pulsed high frequency plasma and ion beam

O. Zabeida*, J.E. Klemberg-Sapieha*, L. Martinu*, and D. Morton**

*Groupe des Couches Minces (GCM) and Engineering Physics and Materials Engineering Department, Ecole Polytechnique, Montreal, H3C 3A7 Canada.

**Denton Vacuum LLC, Moorestown, NJ 08057.

Article published in

Plasma deposition and treatment of polymers

Materials Research Society Symposium Proceedings, Vol. **544**,

(Materials research Society, Warrendale, PA, 1999), pp. 233-238.

Submitted December 1998, accepted February 1999.

Abstract

The energy and the flux of impinging ions are important factors which determine the properties of deposited films and of exposed surfaces (microstructure, density, hardness, roughness, stress, chemical structure, adhesion etc.). In the present work, we use a multigrid retarding field analyzer to study ion bombardment characteristics in two different systems: a pulsed microwave plasma reactor, and a cold cathode ion source. We have found that the ion energy distribution functions (IEDF) possess specific features for each mode of operation: we evaluate the shape and the maximum and the mean ion energies of the IEDF for different gases such as Ar and N_2. These ion characteristics are correlated with surface restructuring of differently treated polymers (polycarbonate and polyethylene terephthalate), analyzed by XPS.

7.1.1 Introduction

The effect of ion bombardment during thin film deposition is well known and widely reported[9,25]. Selective control of the ion-to-deposited-atom flux ratio and of the ion energy allows one to optimize the film microstructure and properties such as density, stress, refractive index, moisture stability, and others. Two deposition techniques use ion bombardment as the main variable for film quality control, namely plasma enhanced chemical vapor deposition (PECVD) and ion assisted physical vapor deposition (IAPVD). In PECVD of dielectric materials, capacitively-coupled RF power, with a blocking capacitor, is frequently used to control the ion energy, while the ion flux and density of active species are governed by the same RF power, or by an additional source of excitation, for example inductively-coupled RF plasma, electron cyclotron resonance plasma, or microwave plasma (the latter, in the so-called dual-frequency MW/RF plasma system[35,96]). In IAPVD, the films are fabricated by evaporation, while energetic ions are provided from an ion source (so-called ion plating).

In polymer processing, the adhesion of a deposited film to a polymer surface is a critical issue: plasma pretreatment of the polymer surface prior to deposition has been proven to mechanically stabilize the surface, and to control the surface chemistry, both effects leading, in synergy, to adhesion enhancement (for a review, see, for example, Refs. 17 and 94). The radicals and VUV radiation originating from the plasma are very important contributors to surface restructuring and to the formation of an "interphase"[94]. Ion bombardment plays a substantial role in the modification of the very first atomic layers on the surface, and its control is crucial for process optimization.

In the present work we have used a multigrid ion energy analyzer to evaluate ion bombardment characteristics in two reactor systems: a pulsed MW plasma reactor, and an ion plating reactor. Polymer samples were exposed to the plasma or ion beam under conditions frequently used for polymer pretreatment, and changes in the surface structure were examined by XPS analysis.

7.1.2 Experimental

In the first set of experiments, a low pressure plasma was excited in a microwave-powered (MW, 2.45 GHz) reactor, described in more detail elsewhere[96,109]. The plasma system consists of a cylindrical stainless steel vacuum chamber (30 cm in diameter), equipped with a grounded aluminum substrate holder (18 cm in diameter) facing a fused silica window (30 cm in diameter). The MW power was applied from a periodic slow-wave applicator (25 cm long), using a power source (Muegge, model M1200), operating in continuous wave (cw) or pulsed modes, with the pulse frequency, f_p, varied from 1 to 10 kHz.

In the second set of experiments, we used a broad-beam ion source (CC-105, Denton Vacuum, LLC) installed in a 75 cm diameter, stainless steel ion plating system ("Integrity-29"). This ion source is a smaller variant of the cold cathode ion source described earlier[123]. The ion beam characteristics are controlled by the discharge current

(drive current), and by the potential between the ring anode and the grounded cathode (drive voltage), which creates the electric field necessary to ionize various gas species. A magnetic field from permanent magnets improves the electron confinement, and allows one to ignite the discharge at relatively low pressures. A hot filament neutralizer was used to avoid surface charging and arcing, and it also served as an additional source of electrons to stabilize the discharge. A pumping speed of 1500 l/s allowed us to maintain the reactor pressure at 0.1-0.4 mTorr, while using gas flow rates of 10-50 sccm, required for proper functioning of the ion source.

Ion energy distribution functions (IEDFs) were measured with a retarding field, three-grid ion energy analyzer[107,114]. In the MW plasma system, the analyzer was differentially pumped and its entrance orifice was located in the center of the substrate-holder electrode, in a close vicinity of the polymeric substrates to be treated. In the ion plating reactor, no differential pumping was necessary; the ion energy analyzer and the samples were placed in three different positions (0°, 22.5° and 45°) with respect to the ion source axis, at a distance of 0.5 m from the source.

In both systems, we used argon and nitrogen as feed gases, in order to modify polyethylene terephthalate (PET) and polycarbonate (PC) substrates. The surface chemical structure was examinated by X-ray photoelectron spectroscopy (XPS) in a VG-ESCALAB MK II surface instrument.

7.1.3 Results and discussion

7.1.3.1 Ion Energy Analysis

In the MW plasma system, the IEDFs on the substrate holder were evaluated under the plasma conditions usually employed for surface modification of polymers, particularly those required for enhanced adhesion[94,124]. The IEDFs measured for pulsed MW plasma in argon are illustrated in Fig. 7.1, where ion energies are seen not to exceed 10 eV under any of the conditions. We note that the IEDF for the *cw* MW plasma consists

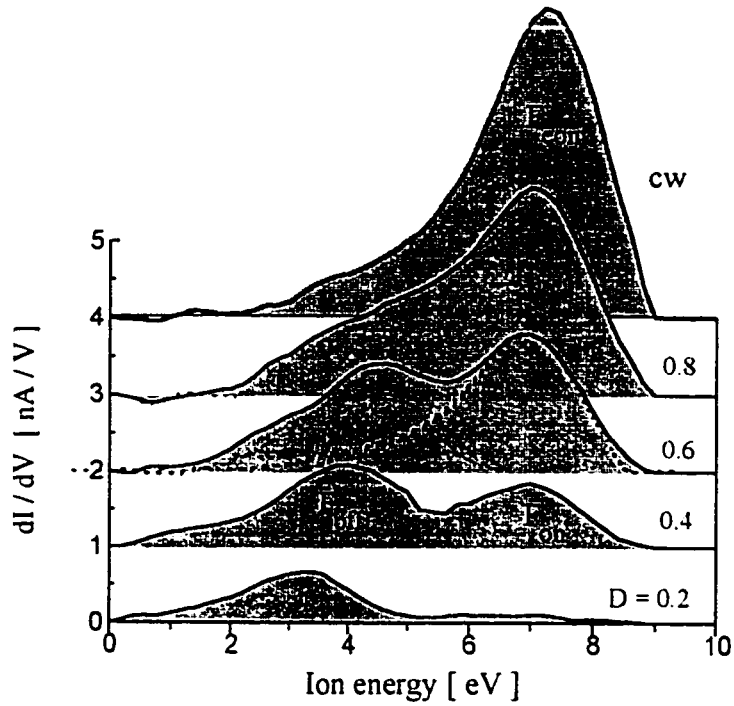

Figure 7.1. Ion energy distribution function (IEDF) in a pulsed argon MW plasma, for different values of duty cycle, *D*. The Ar pressure was 200 mTorr, the MW peak power 700 W, and the pulse frequency 1 kHz. F_{on} is the intensity (flux) similar to the cw regime, and F_{off} is the intensity (flux) of the low energy peak.

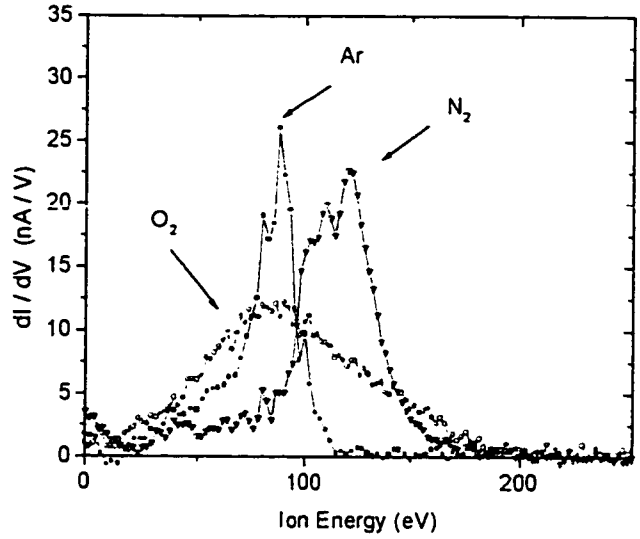

(a)

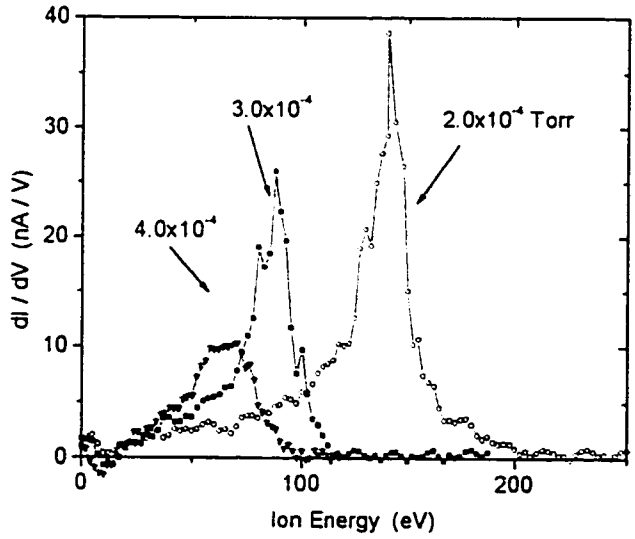

(b)

Figure 7.2. IEDFs of the broad ion beam, measured at an angle of 22.5° from the source axis: a) effect of different feed gases at a pressure of 0.3 mTorr; b) effect of argon pressure. The drive current was 2 A.

of a single peak, with a characteristic low-energy tail due to ion-neutral collisions in the sheath. The shape of the distribution changes substantially when a pulsed mode is used: a second peak appears on the low-energy side of the IEDF as the duty cycle, D, is decreased. Since this peak becomes more pronounced for low D values, we attribute it to ions arriving during the period between successive pulses, T_{off}. The low energy of ions contributing to this peak reflects the low plasma potential during the post-discharge period. In addition, a weak feature appears on the high-energy side of the distribution, presumably due to ions formed during the period of the transient spike at the beginning of each pulse[93]. The average total ion energy, determined from the complete IEDF, decreases with decreasing D, as the low-energy peak becomes more pronounced (see Fig. 7.1).

In the ion plating reactor, the IEDFs were measured for the three most frequently used gases, namely argon, nitrogen, and oxygen. Figure 7.2a represents the IEDFs at a pressure of 0.3 mTorr, and a drive current of 2 A. Increasing the drive current leads only to a slight increase of the mean ion energy, while the ion current density increases substantially. For lower pressures, this increase is even more significant. The drive current allows one to control the ion flux during deposition or polymer treatment, while keeping ion energies essentially the same. The IEDFs measured for different angles with respect to the ion source were very similar in shape and intensity, which confirms that the broad ion beam has a good uniformity.

The IEDFs of argon ions at different pressures in the ion plating reactor are presented in Fig. 7.2b, where two effects are seen to occur with increasing pressure. First, the ionization rate (hence, the plasma density) in the source increase, which results in a decrease of the drive voltage, to keep the drive current constant. This explains the observed drop in the mean ion energy with rising pressure. The ion current drops rapidly, in agreement with the Child-Langmuir law, but this effect is also enhanced by changes in the plasma geometry. Another phenomenon we observe is broadening of the IEDF, which may be attributed to increased ion-neutral collisions. The latter effect is expected

to lead to increased bombardment of the surface by fast neutrals, but this has not been investigated in the present work. Similarly, we cannot distinguish singly- or doubly-charged ions, nor species with different masses. This lack of information somewhat complicates the interpretation of molecular gas IEDFs. Even in the case of argon, for which Ar^+ ions dominate, the presence of ions with higher energies than that corresponding to the drive voltage, points to charge transfer in which doubly-charged ions participate.

7.1.3.2 Analysis of Polymer Surfaces

The effect of treatment on polymer surface restructuring was evaluated by high resolution XPS. As an example, the chemical structure and a typical C(1s) spectrum of untreated PET is shown in Fig. 7.3. The curve-fitted peaks C1–C4 correspond to C–C and C-H bonds (285.0 eV), C–O (286.5 eV) and O=C-O (288.9 eV) groups, and to shake-up (291.4 eV), respectively, where the latter peak is associated with the benzene ring. After treatment in argon or nitrogen, the C(1s) peak is substantially modified, due to contributions of O- and N-containing bonds. Changes in the shake-up peak bear witness to opening of the benzene rings (E_B = 5.4 eV), an effect that cannot be produced by thermal atomic nitrogen, but rather by energetic bombardment.

The effect of duty cycle on the surface chemical structure of PET, using nitrogen and argon MW plasmas, is illustrated in Fig. 7.4 in terms of the relative area of the shake-up peak, and of nitrogen incorporation. In all treatments, the samples were exposed to the plasma for the same total value of plasma "on" time. The peak MW power also remained constant (1200 W for nitrogen, and 720 W for argon), in order to maintain the same power delivered during the treatment. The intensity of the shake-up peak is seen to decrease with increasing D, an effect which is more pronounced in the case of argon plasma, presumably on account of the heavier Ar^+ ions.

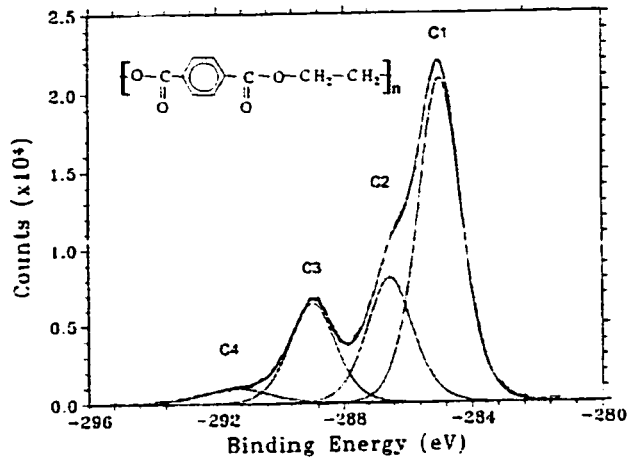

Figure 7.3. C(1s) XPS spectrum of untreated PET.

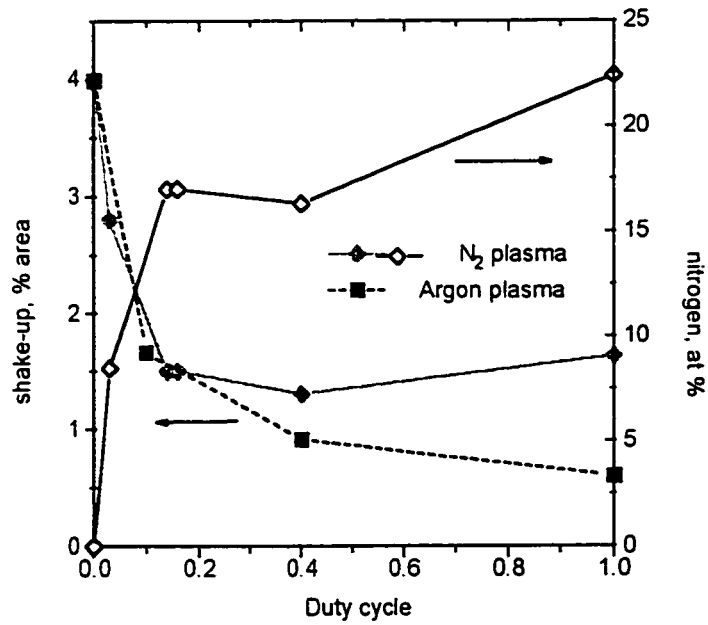

Figure 7.4. Nitrogen concentration and shake-up relative area on the surface of PET, treated in the pulsed MW plasma, as a function of duty cycle.

We also note that the concentration of incorporated nitrogen increases with D, first very fast for low D values, but then saturating for D close to 1 (see Fig. 7.4). There may be several reasons for this: (i) the mean energy of ions, mostly N_2^+ in nitrogen plasma, arriving at the surface is significally higher for high D values than for low ones. This higher energy results in a more pronounced surface restructuring, and in possible dissociation of the N_2^+ ions (E_d = 8.7 eV); (ii) the total energy absorbed by the surface during each plasma treatment is the same for all samples, but the substrate has less time to dissipate this energy in the case of high D values. Therefore, the surface temperature rises with increasing D, and this may enhance the surface chemical activity; finally, (iii) the concentration of nitrogen atoms, which can react with polymers, increases with rising plasma density, which, in turn, is higher at high D values. This also applies to plasma emitted UV radiation, which acts in synergy.

Figures 7.5 and 7.6 present the results of treatment by argon and nitrogen ions in the ion plating reactor. For both gases, the surface composition is independent of the substrate position; a 10 second exposure, which corresponds to a total fluence of $\sim 5 \cdot 10^{15}$ ions/cm^2, is enough to cause pronounced surface restructuring in all cases, while a six-fold longer treatment duration with Ar ions apparently leads to a complete breakup of benzene rings within the XPS sampling depth, for both PC and PET surfaces. In the case of nitrogen ions, longer exposure does not further change the surface structure. The maximum nitrogen uptake was about 12 at.%, which is expected to be sufficient for significant adhesion improvement, as suggested by our earlier measurements[124].

7.1.4 Conclusions

A retarding multigrid ion energy analyzer has been successfully used to evaluate the ion energy characteristics in two different reactor systems, applied for polymer treatments. Structured, bimodal IEDFs have been observed in pulsed MW plasma, and the relative intensities of the two constituent peaks are found to depend on the duty

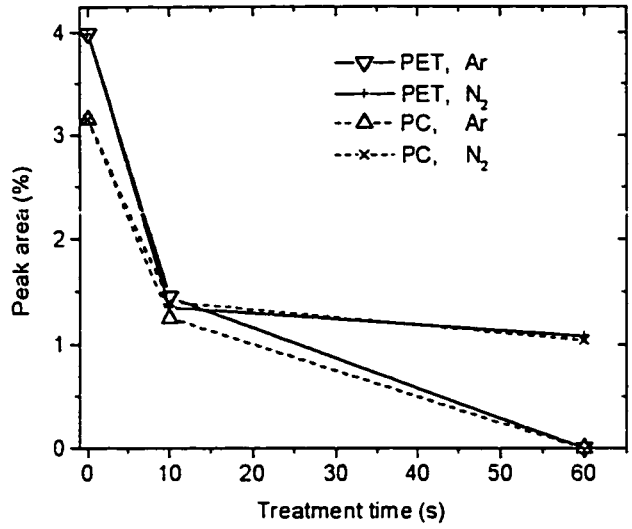

Figure 7.5. Shake-up relative area on the surface of PET and PC, exposed to ion beam in N_2 and Ar, as a function of treatment time.

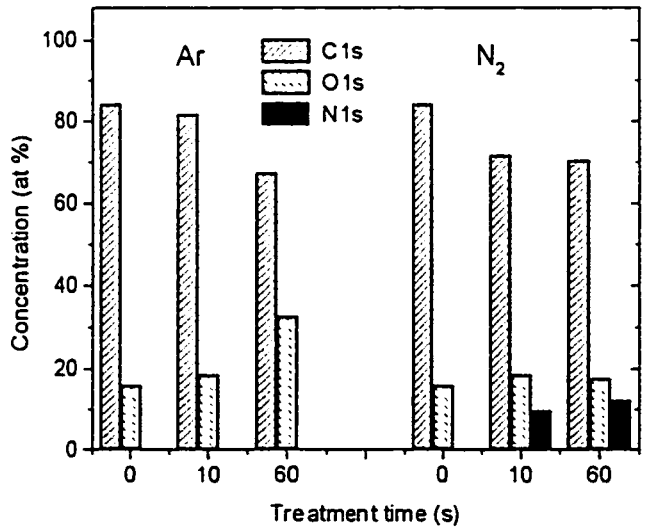

Figure 7.6. Effect of ion beam treatment using Ar and N_2 on the surface chemical composition of PET.

cycle, D. It was found that the mean ion energy rises with increasing D, and that this rise contributes to more pronounced restructuring of exposed polymer surfaces, the ion flux being kept constant. Similar surface restructuring effects were also observed when the polymers were treated with a broad-beam, cold cathode ion source. Both approaches, namely the pulsed plasma and the ion beam, allow one to selectively control the energy and flux of impinging ions, in a manner which is complementary to the dual frequency (MW/RF) technique described earlier[35,96]. Additional time- and energy-resolved mass spectrometry measurements are now in progress in our laboratory.

Acknowledgments

The authors wish to thank Professor M.R. Wertheimer for numerous fruitful discussions. We also acknowledge the expert technical assistance of Mr. G. Jalbert. This work was supported by grants from the Natural Sciences and Engineering Research Council (NSERC) of Canada.

7.2 Ion bombardment characteristics during the growth of optical films using a cold cathode ion source

O. Zabeida, J.E. Klemberg-Sapieha, and L. Martinu

Ecole Polytechnique, Department of Engineering Physics and Materials Engineering, Montreal, Quebec, H3C 3A7, Canada;

and D. Morton,

Denton Vacuum LLC, Moorestown, NJ

published in

42nd Annual Technical Conference Proceedings

(Society of Vacuum Coaters, Chicago), 267-272 (1999).

Abstract

In the present work, the energy and flux of impinging ions are evaluated in the context of ion-assisted deposition of optical films and ion-induced modification of polymer surfaces for improved adhesion. The experiments were performed in a vacuum system equipped with a broad beam cold cathode ion source. The ion energy distribution functions were measured using a multigrid retarding field analyzer for discharges excited in different gases such as O_2, Ar, and N_2. The ion beam characteristics, namely the maximum ion energy, the mean ion energy, and the ion flux, were correlated with the properties of Ta_2O_5 and TiO_2 layers deposited by e-beam evaporation assisted by an oxygen ion beam. These different materials were analysed by spectroscopic ellipsometry, spectrophotometry, and profilometry. Their optical and mechanical behaviour, such as refractive index and stress, are correlated with the evolution of the film microstructure.

7.2.1 Introduction

Ion bombardment is very important in the growth of films and modification of surfaces; it leads to resputtering, knock-in effects, subplantation, breakage of chemical bonds in polymers, etc.[9,18,95] We have recently constructed and tested a versatile multigrid retarding field ion energy analyzer (IEA) for the determination of ion energy distribution functions (IEDFs) in vacuum processing systems: It has been applied for the characterization of microwave (MW) (pulsed and continuous), radio-frequency (rf), and dual mode MW/rf plasmas,[107,114] as well as for a magnetron sputtering system.[125] IEDFs of nitrogen ions for the cold cathode ion source were also analysed in the context of polymer treatment (Section 7.1). In the present work we systematically evaluate, using the IEA, the ion characteristics of a broad beam cold cathode ion source, and we relate them to the properties of optical coatings such as TiO_2 and Ta_2O_5, fabricated by ion beam assisted deposition (IBAD).

7.2.2 Experimental setup

A broad-beam ion source (CC-105, Denton Vacuum, LLC) was installed in a 75 cm diameter stainless steel ion plating system ("Integrity-29", Denton Vacuum, LLC). This ion source is a smaller variant of the cold cathode ion source described earlier.[123] The ion beam characteristics are controlled by the discharge current (drive current), I_D, and by the potential between the ring anode and the grounded cathode (drive voltage), V_D; the latter parameter creates an electric field necessary to ionize the gas species. The magnetic field from permanent magnets improves the electron confinement, and it allows one to ignite the discharge at relatively low pressures in the reactor. A hot-filament neutralizer was used to avoid surface charging and arcing, and it also served as an additional source of electrons to stabilize the discharge. A pumping speed of 1500 l/s (cryopump) allowed us to maintain the reactor pressure between $1 \cdot 10^{-4}$ and $4 \cdot 10^{-4}$ Torr, while using gas flow rates of 10-50 sccm of Ar, O_2, and N_2, required for proper functioning of the ion source.

The IEDFs were measured with a retarding field, three-grid ion energy analyzer[114] illustrated in Figure 7.7. For the pressure range used in this work no differential pumping was necessary. The IEA was placed at a distance of 0.5 m from the source in three different positions (0°, 22.5° and 45°) with respect to the ion source axis. The IEDFs were obtained by derivation of the $I(V_s)$ characteristic, where I is the collector current (see Figure 7.7) and V_s is the scanning potential (both of them were controlled by a computer).[114] Energy resolution of the IEA is about 2 eV.

Thin titanium oxide and tantalum oxide films were deposited by electron beam evaporation of the respective metals in an oxygen atmosphere, assisted by oxygen ion bombardment from the cold cathode ion source.

The refractive index and thickness of films were determined from the measurements using a variable angle spectroscopic ellipsometer (VASE, J.A. Woollam Co., Inc.) and a spectrophotometer (Lambda 9000, Perkin Elmer). The film stress was determined by a

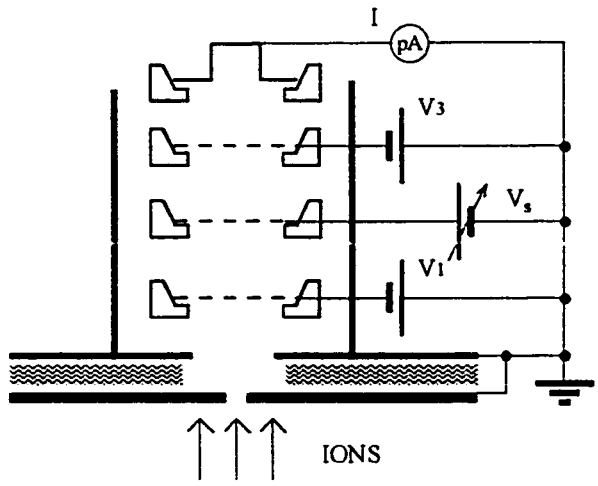

Figure 7.7 Schematic representation of the ion energy analyzer

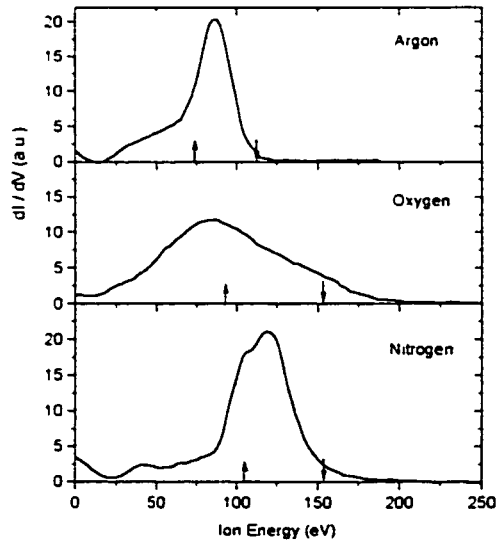

Figure 7.8 IEDFs measured for different working gases. I_D is 2 A , pressure is $3 \cdot 10^{-4}$ Torr and the angle from the source axis is 22.5° for all presented curves. Here and in all other IEDFs in this article, upward and downward pointing arrows indicate $\langle E_i \rangle$ and V_D, respectively.

curvature method using laser interferometry (Flexus, Tencor). In order to evaluate the film structural stability, selected specimens were annealed to 400 °C and 800 °C in laboratory air.

7.2.3 Results and discussion

7.2.3.1 Ion energy distributions

Typical IEDFs, measured for three frequently used gases, namely argon, nitrogen, and oxygen, at the same pressure of 0.3 mTorr and I_D = 2 A are shown in Figure 7.8. Depending on the gas nature, the distributions exhibit different shapes. One should keep in mind that the process conditions for each gas slightly varied: in the case of argon, a lower drive voltage, 115 V, is applied, compared to 155 V for oxygen and nitrogen, as a consequence of a higher ionization rate in argon compared to molecular gases. On the other hand, in the case of nitrogen and oxygen all external parameters were almost identical; nevertheless, the IEDF for oxygen is much broader and it is shifted to lower energies. This difference can be attributed to negative ion formation in oxygen plasma that changes the plasma potential distribution in the source. Access to the IEDF allowed us to evaluate for each set of experimental conditions an important process parameter, namely the mean ion energy, $\langle E_i \rangle$, using the following expression:

$$\langle E_i \rangle = \frac{\int E \cdot f_i(E) dE}{\int f_i(E) dE}. \tag{7.1}$$

Here $f_i(E)$ represents the specific IEDF.

Since oxygen is frequently used in the fabrication process of optical coatings, we particularly focused on the ion characteristics in this gas. Figure 7.9 represents the IEDFs for oxygen at a pressure of 0.2 mTorr but at different I_D values. Increasing I_D leads to broadening of the IEDF, while the ion current density increases substantially. $\langle E_i \rangle$ is shown in Figure 7.10 as a function of I_D for different angles with respect to the

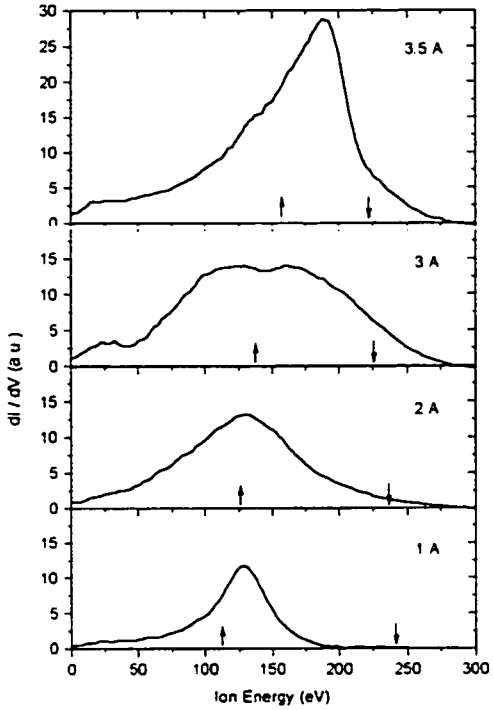

Figure 7.9 IEDFs for different I_D values at an oxygen pressure of $2 \cdot 10^{-4}$ Torr.

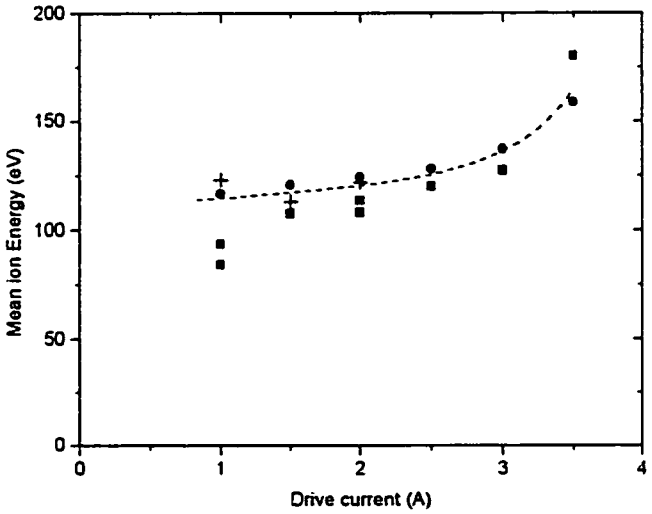

Figure 7.10 Mean ion energy as a function of drive current for different angles with respect to ion source axis: triangles- 0°, squares - 22.5°, and circles- 45°.

source axis. $\langle E_i \rangle$ values monotonously increase; less variation in $\langle E_i \rangle$ was observed for I_D between 1.5 and 2.5 A. We conclude that the drive current allows one to control the ion flux during deposition while keeping the mean ion energy essentially the same. The IEDFs measured for different angles with respect to the ion source axis yield $\langle E_i \rangle$ values and intensities very close to each other, which confirms a beam uniformity of about 10% over the measured area (~0.5 m^2 assuming axial symmetry).

The effect of pressure on the IEDFs of oxygen ions is shown in Fig. 7.11. Two effects are observed to occur when the pressure increases: (i) the drive voltage decreases leading to the observed drop in $\langle E_i \rangle$ as illustrated in Figure 7.12; (ii) the ion current (area under the curves) drops, in agreement with the Child-Langmuir law ($I \propto U^{3/2}$). It is believed that this effect interferes with changes in the shape of the plasma edge, from which the ions are extracted (plasma expansion at lower pressure). In contrast to nitrogen ions (Section 7.1) no IEDF broadening due to ion-neutral collisions has been observed here.

In the case of oxygen, IEDFs are narrower, which may also be attributed to geometrical changes of the extraction zone. It is intuitively expected that V_D is a parameter most closely related to the ion energy. Indeed, as one can see in Fig. 7.13, the $\langle E_i \rangle$ values derived from almost all IEDFs obtained over a large range of drive currents (0.5-4 A) and gas pressures ($1.5\text{-}4.0 \cdot 10^{-4}$ Torr) lie between $0.4 \cdot eV_D$ and $0.7 \cdot eV_D$. Therefore, a value of $0.5 \cdot eV_D$ can serve as a good approximation of $\langle E_i \rangle$ for the ion source studied in this work.

Due to principal limitations of our IEA, we cannot distinguish either single- or double-charged ions, or ions with different masses. This lack of information somewhat complicates the interpretation of the IEDFs in molecular gases. Presence of ions with higher energies than those corresponding to the drive voltage (see Figures 7.8, 7.9, and 7.11), points to charge transfer in which double-charged and molecular ions can participate. Our recent mass-resolved measurements of IEDFs in nitrogen rf and MW plasmas clearly prove this statement.[121]

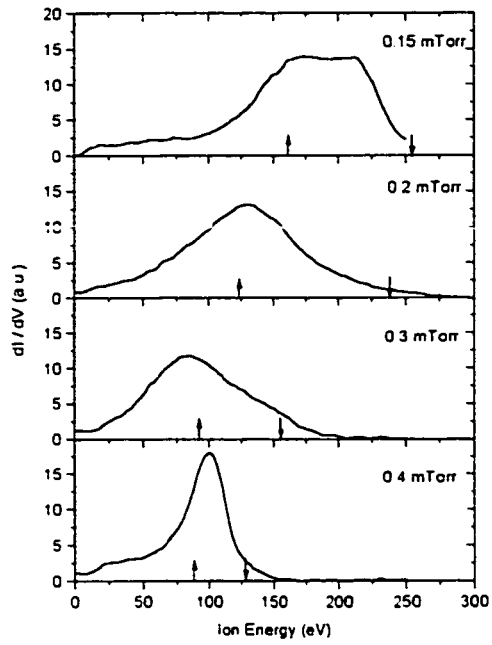

Figure 7.11 IEDFs for different oxygen pressure values at I_D = 2 A.

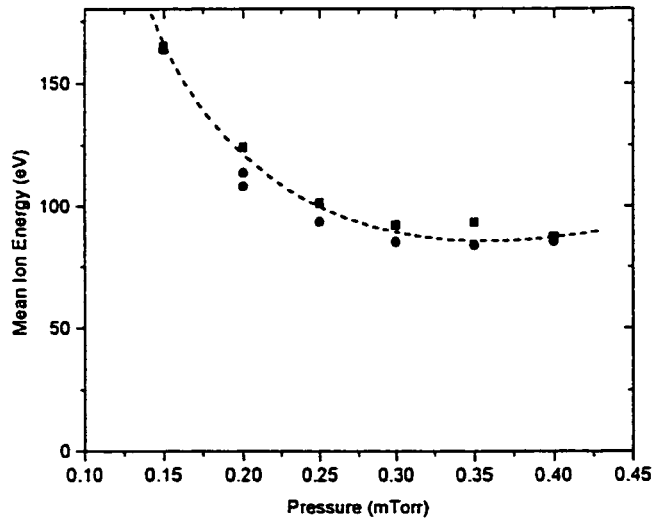

Figure 7.12 Mean ion energy as a function of pressure for different angles with respect to ion source axis: squares - 22.5°, circles- 45°.

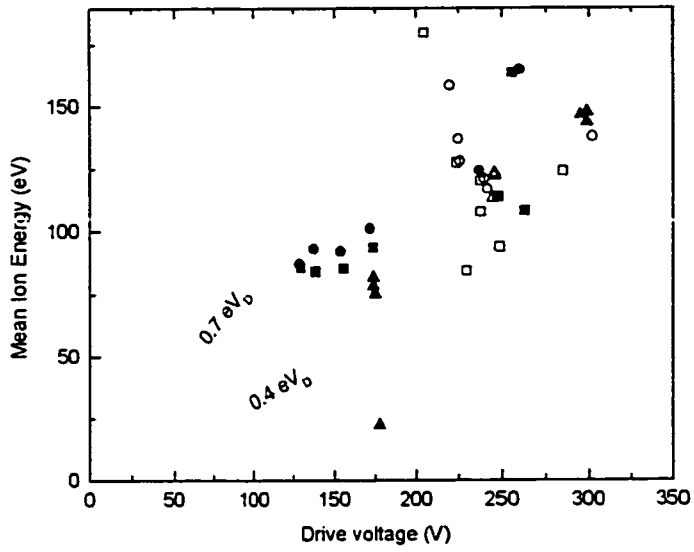

Figure 7.13. Mean ion energy as a function of drive voltage for different angles with respect to ion source axis: triangles- 0°, squares - 22.5°, circles- 45°.

7.2.3.2 Film analysis

We studied the effect of ion energy and ion flux on the refractive index, the deposition rate and the internal stress of TiO_2 and Ta_2O_5 films, and the results are summarized in Table 7.1. Clearly, a higher ion flux gives rise to material densification, accompanied by a decrease of the deposition rate and an increase of the refractive index, in agreement with an abundant literature on this subject (e.g., Ref.18).

As discussed in Ref. 95, the effect of ion bombardment on the evolution of the film microstructure can be described by a single parameter, E_p, namely the energy delivered to the film per deposited atom:

$$E_p = \langle E_i \rangle \cdot \Phi_i / \Phi_n \qquad (7.2)$$

Table 7.1. Conditions of film deposition and film characteristics.

Film	I_D (A)	V_D (V)	$\langle E_i \rangle$ (eV)	I ($\mu A/cm^2$)	$\langle E_i \rangle$ x I(mW/cm^2)	Film thickness (nm)	n (at 600 nm)	Stress (MPa)
Ta_2O_5	0	0	0	0	0	396	2.09	1
	1	224	115	28	3.2	341	2.07	99
	2	284	126	57	7.2	322	2.12	98
	3	264	138	90	12.3	306	2.16	78
TiO_2	0	0	0	0	0	418	2.15	176
	1	244	115	28	3.2	365	2.26	214
	2	308	126	57	7.2	305	2.39	183
	3	278	138	90	12.3	297	2.44	-391

Here Φ_i is the ion flux and Φ_n is the flux of condensing atoms. Equation 7.2 is a simplified version of a more complex description of ion-assisted phenomena.[17]

Evolution of the TiO_2 and Ta_2O_5 film characteristics is shown plotted in Figure 7.14 as a function of E_p. The results indicate that the deposition rate for both films decreases with E_p as a consequence of densification at higher energy fluxes toward the film. The stress is relatively low (0 - 200 MPa), and it is tensile for lower E_p values, while one measurement suggests its conversion to a compressive one. The effect of E_p appears to be more significant on the evolution of n values for TiO_2 than for Ta_2O_5. TiO_2 is therefore more sensitive to the E_p variations in the present range of conditions, in agreement with the structure-zone model.[31-33]

Selected samples, namely those deposited at the highest and the lowest ion flux and E_p values for both materials, were annealed for one hour at 400 and 800 °C. The effect on the film thickness, the refractive index and the surface roughness is illustrated in Table 7.2. Systematically higher thickness stability has been found for both materials for the films deposited at high E_p values as expected. It should be mentioned, however, that annealing at 800 °C was accompanied by a strong increase in surface roughness that may have partially affected the accuracy in determining the refractive index and thickness. Modification of surface morphology appears to be related to a transition from an amorphous to partially crystalline microstructure upon annealing between 400 °C and 800 °C, as indicated by our preliminary X-ray diffraction measurements, and also reported by other authors.[126] A more detailed study of structural stability of these films is presently in progress in our laboratory.

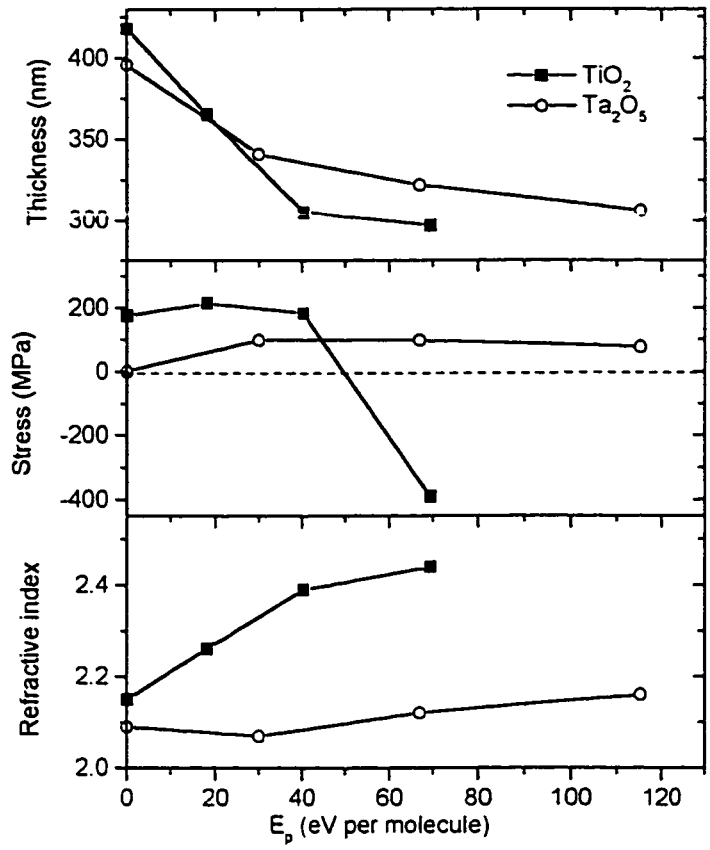

Figure 7.14. Film characteristics as a function of total ion energy per deposited molecule

Table 7.2 Effect of annealing temperature on the optical properties of deposited films.

Film	I_D (A)	Temperature (°C)	Thickness (nm)	Roughness (nm)	n (at 600 nm)	Mean Squa Error
TiO_2	0	20	396	0	2.15	
		400	390	0	2.25	10
		800	382	0	2.26	21
	3	20	306	0	2.44	
		400	298	4.2	2.47	16
		800	282	7.4	2.62	19
Ta_2O_5	0	20	418	0	2.09	
		400	331	2.0	2.09	5
		800	302	15.3	2.20	66
	3	20	297	0	2.16	
		400	302	2.2	2.15	5
		800	282	4.8	2.28	50

7.2.4 Conclusions

The present work has been performed as part of our continued interest in the analysis and control of ion bombardment effects in the growth of thin films. We describe a simple three-grid electrostatic ion energy analyzer we have used for the evaluation of ion energy distribution functions in an IBAD system, equipped with a cold cathode broad beam ion source. Systematic measurements of the IEDFs over a large range of process conditions were performed to determine the mean ion energy and the total ion flux. These values were used to calculate an important process parameter, namely the ion energy per deposited atom, which should be optimized in order to obtain the desired performance of deposited films. Such an approach has been illustrated by the measurements of the characteristics of TiO_2 and Ta_2O_5 optical films.

Acknowledgements

The authors wish to thank Mr. G. Jalbert for his expert technical assistance, Mr. P. Bellerose for the stress measurements, and Mr. D. Dalacu and Mr. D. Poitras for the evaluation of optical characteristics.

CHAPTER 8. Conclusions and proposed future work

8.1 Conclusions

As described in Chapter 1, the energetic interactions due to ions are very important in the processing of materials. This aspect is particularly significant in the context of PECVD and surface modification of materials, a subject of great importance in materials science in general and in our Plasma Processing Laboratory in particular. In response to the objectives of this work outlined in Chapter 2, the main conclusions may be summarized as follows:

1. A methodology for evaluating ion bombardment energetics has been developed, which is suitable for different plasma processing systems. Two instruments, namely the multigrid retarding field ion energy analyzer and the Hiden EQP-1000 plasma probe were applied for the analysis of ion energy distribution functions in complex plasma environments such as rf, MW and dual-mode MW-rf discharges in both the continuous wave and pulsed modes. The former instrument (the IEA) was constructed, fully characterized, and optimized for its versatile use in different reactors including the IBAD system.

   Detailed analysis of the IEDFs based on the IEA measurements allowed us to characterize the features of pulsed discharges using a global model approach. These results were then confirmed by time- and mass-resolved IEDF evaluations.

2. We systematically studied the effect of external parameters such as pressure, power, excitation mode, and pulsing on the ion bombardment characteristics within a process window generally used for materials processing. The main attention was paid to the dual-frequency and pulsed regimes. It was found, using time-resolved measurements, that in the pulsed MW/rf plasma the ion energies are strongly affected by V_b modulation. It was confirmed that MW/rf plasma is not a mere superposition

of the rf and MW discharges, but the two act in synergy, giving rise to an independent control of the ion flux and ion energy, which is very important for tailoring the materials microstructure.

Two distinct features in the IEDFs in pulsed MW plasmas were observed, namely a bimodal peak in the distribution. We associated the high energy part with the ions arrived during the time-on period, while the low energy one was related to the time-off interval of the pulse cycle. We showed that the pulsing parameters such as the duty cycle and the pulse frequency in MW plasma can be also applied for an energy-selective control of the ion bombardment characteristics.

3. Rf probe measurements were used as a complementary technique to characterize the plasma impedance and rf power dissipation. These measurements allowed us to explain the effect of V_b modulation in the pulsed MW/rf plasma, namely to demonstrate its fully capacitive character during the MW-off period, and a partially resistive character when MW pulse is on. Such measurements were then used to reconstruct the total IEDF from individual time-resolved features. The conclusions about plasma density and sheath thickness obtained from plasma impedance measurements were found to be in full agreement with the data generated by IEDF processing. This approach is an essential technique in order to determine the ion bombardment parameters, for example the energy delivered per deposited atom in controlled film growth experiments.

4. The effect of energetic ions on the properties of plasma treated surfaces and deposited films was studied. Preliminary semiquantitative measurements on polymers exposed directly to a plasma or to an ion beam exhibited similar surface restructuring effects, namely the benzene ring opening and nitrogen incorporation. It was found that in the pulsed MW plasma the pulse parameters such as the duty cycle affect the level

of surface reorganisation. This was correlated with the ion bombardment energy which in such experiments is comparable with the binding energy in organic molecules.

2. Future work

This work is the first one in our laboratory devoted to a systematic study of ion characteristics in high frequency and the dual-frequency plasma reactors operating in different excitation modes. It concentrated primarily on the methodological and general plasma diagnostics issues. Some subjects, for example, the correlation between ion characteristics and film properties, were just touched, while they evidently require a deeper and more complex study. One can separate the possible future studies in four principal directions:

1. Versatile IEA for the optimization of plasma processing conditions

There exists a great practical interest to evaluate the IEDFs in PECVD and other plasma reactors, in particular to compare the ion characteristics in the different processing systems. For this purpose the small, easy-to-manipulate and reliable ion energy analyzer is very helpful. Such work is already being planned in the PPL.

2. The effect of external parameters on the IEDF and rf impedance

Since the precise IEDF measurements present certain problems in industrial reactors, it is important to determine the correlation with the external, easily accessible parameters, which can be used to evaluate the plasma characteristics in general, and the ion characteristics in particular. One of such parameters, V_b, is well-known to be a key characteristic, but in complex configurations, such as MW/rf plasma, it is not fully reliable. It appears that the plasma impedance measurements may give additional key information. Such evaluations in different plasma reactors are proposed and will be subsequently performed in different systems.

3. Other plasma parameters

Ion bombardment is only one part of the PECVD or IBAD processes. Other important characteristics include the flux and energy of neutrals, radicals, and photons. All of them are complex functions of gas composition, plasma density, electron energy distribution and other parameters. This necessitates a combined multi-technique diagnostic study of the process. Mass spectrometry, Langmuir probe measurements, optical emission (including VUV) spectroscopy, laser induced fluorescence are possible complementary techniques to be used.

4. Synergetic effect on the surface

The specific effect of each process involved in plasma-surface interactions as well as their synergy still call for more detailed studies; unfortunately, it is difficult to decouple them in the complex plasma environment. One may use an ion beam to simulate directly the ion bombardment generated by plasma, UV lamps (one is already in the process of being acquired) to study the effect of photons, mass-separated molecular beams to understand the role of different radical species, etc. Multiple techniques for the characterization of the surface chemical composition, and of the optical, mechanical, and electrical properties are already in use in our laboratory. The work to correlate the surface properties with processes in the plasma volume and with the sheath parameters appears to be very important in order to predict the microstructure of deposited materials, and to be able to generate new materials with specially designed characteristics. For example, evaluations of more complex plasma environments considering chemically active gases combined with the optimization of ion bombardment in order to obtain high temperature structural phases appears to be very important for the fabrication of nanocomposite materials, another on-going project in our laboratory. It should be mentioned at this point that the results generated in this work will become an important experimental input parameter in the theoretical studies of the film growth under energetic conditions,

such as in the molecular dynamics simulations of the growth of Si–compound films (on-going Ph.D. project of A. Lefevre).

REFERENCES:

1. O. Meyer, G. Linker, and F. Kappeler, (Eds.) "Ion beam surface layer analysis", Plenum Press, New York, 1976.
2. T. G. Finstad and W.-K. Chu, "Rutherford backscattering spectrometry on thin solid films", in "Analytical techniques for thin films", Eds. K. N. Tu and R. Rosenberg, (Academic Press, San Diego, CA) pp.392-449.
3. L. C. Feldman, "Applications of ion beams to materials science" in "Interaction of Charged Particles with Solids and Surfaces", Eds. A. Gras-Marti, H. M. Urbassek, N. R. Arista, and F. Flores, (NATO ASI series B. Physics, v. 271, Plenum Press, New York, 1991) pp. 309-312.
4. R. Kelly, "Implantation, recoil implantation and sputtering", in "Ion Bombardment Modification of Surfaces", Eds. O. Auciello and R. Kelly, (Elsevier, New York, 1984) pp. 27-78.
5. J. F. Ziegler, "Ion implantation: science and technology", Academic Press, Orlando, 1984.
6. A. C. Adams, in "VLSI Technology", S. Sze, Editor, Chap. 3, McGraw-Hill, New York, 1983.
7. D. Briggs, "Surface analysis of polymers by XPS and static SIMS", Cambridge University Press, New York, 1998.
8. H. Oechsner, "Secondary neutral mass spectrometry (SNMS) and its application to depth profile and interface analysis", in "Depth profile analysis", Ed. H. Oechsner, (Springer-Verlag, Berlin, 1984) pp. 63-84.
9. S. M. Rossnagel, J. J. Cuomo, and W. D. Westwood (Eds.), "Handbook of Plasma Processing Technology", (Noyes Publications, Park Ridge, NJ, 1990).
10. G. S. Oehrlein, "Reactive ion etching", pp. 196-232 in Ref. 9.

11. R. Reif, "Plasma Enhanced Chemical Vapour Deposition of Thin Films for Microelectronics", pp. 260-284 in Ref. 9.

12. J. J. McNally, "Ion assisted deposition", pp. 448-465 in Ref. 9.

13. D. M. Mattox, "Ion plating", pp. 338-355 in Ref. 9.

14. I. Yamada, "Ionized cluster beam (ICB) deposition techniques", pp. 356-369 in Ref. 9.

15. M. R. Wertheimer, L. Martinu, J. E. Klemberg-Sapieha, G. Czeremuszkin, "Plasma treatment of polymers to improve adhesion", in "Adhesion promotion techniques: Technological applications", Eds. K. L. Mittal and A. Pizzi, Marcel Dekker, New York (1999), 139-173.

16. M. R. Wertheimer and L. Martinu, "Ion bombardment effects in dual microwave / radio frequency plasmas", in "Microwave Discharges: Fundamentals and Applications", Eds. C. M. Ferreira and M. Moisan, NATO ASI Series B, vol. **302**, (Plenum Press, New York, 1993) pp. 465-481.

17. L. Martinu, "Plasma deposition and testing of hard coatings on plastics", in "Plasma Processing of Polymers", Eds. R. d'Agostino, F. Fracassi, and P. Favia, (Kluwer Academic Publishers, Netherlands, 1997) pp. 247-272.

18. J. J. Cuomo, S. M. Rossnagel, and G. R. Kaufman, (Eds.), "Handbook of ion beam processing technology", (Noyes Publications, Park Ridge, NJ, 1989).

19. H. F. Winters, "Elementary processes at solid surfaces immersed in low pressure plasmas", in "Topics in Current Chemistry **94**, Plasma Chemistry III", Eds. S. Veprek and M. Venugopalan, (Springer-Verlag, Berlin, 1980) pp. 69-125.

20. J. M. E. Harper, J. J. Cuomo, R. G. Gambino, H. R. Kaufman, "Modification of thin film properties by ion bombardment during deposition", in "Ion Bombardment Modification of Surfaces", Eds. O. Auciello and R. Kelly, (Elsevier, New York, 1984) pp. 127-162.

21. J. J. Cuomo and S. M. Rossnagel, Nucl. Instrum. Meth. in Phys. Res. B **19**, 963 (1987).

22. E. Taglauer, W. Heiland, and U. Beitat, Surf. Sci. **89**, 710 (1979).

23. R. A. Roy and D. S. Yee, "Control of film properties by ion-assisted deposition using broad beam sources", in Ref. 18, pp. 194-218.

24. P. Ziemann and E. Kay, "Correlation between the ion bombardment during film growth of Pd films and their structural and electrical properties", J. Vac. Sci. Technol. A **1**(2), 512-516 (1983).

25. E. Kay and S. M. Rossnagel, "The modification of films by ion bombardment", in Ref. 18, pp.170-193.

26. J. Musil and S. Kadlec, "Reactive sputtering of TiN films at large substrate to target distances", Vacuum **40**, 435-444 (1990).

27. J. Musil, "Inter-relationships process parameters/microstructure/film properties a key to new materials and applications" in Proc. of the Int. Symp. on "Elementary Processes and Chemical Reactions in Low Temperature Plasma", Casta, Slovakia, 1992, p. 177.

28. I. Petrov, F. Adibi, J. E. Greene, W. D. Sproul, and W.-D. Munz, "Use of an externally applied axial magnetic field to control ion/neutral flux ratios incident at the substrate during magnetron sputter deposition", J. Vac. Sci. Technol. A **10**(5), 3283-3287 (1992).

29. K. Ino, T. Shinohara, T. Ushiki, and T. Ohmi, J. Vac. Sci. Technol. A **15**, 2627 (1997).

30. P. J. Kelly and R. D. Arnell, "Development of a novel structure zone model relating to the closed-field unbalanced magnetron sputtering system", J. Vac. Sci. Technol. A **16**(5), 2858-2869 (1998).

31. B. A. Movchan and A. V. Demchishin, "Investigation of the structure and properties of thick vacuum-deposited films of nickel, titanium, tungsten, alumina, and zirconium dioxide", Fiz. Metallov Metalloved. **28,** 653-660 (1969).

32. J. A. Thronton, "Influence of apparatus geometry and deposition conditions on the structure and topography of thick sputtered coatings", J. Vac. Sci. Technol. **11**, 666-670 (1974).

33. R. Messier, A. P. Giri, and R.A. Roy, "Revised structure zone model for thin film physical structure", J. Vac. Sci. Technol. A **2**(2), 500-503 (1984).

34. L. Martinu, J. E. Klemberg-Sapieha, and M. R. Wertheimer, "Dual-mode microwave/radio frequency plasma deposition of dielectric thin films", Appl. Phys. Lett. **54**(26), 2645-2647 (1989).

35. L. Martinu, J. E. Klemberg-Sapieha, O. M. Küttel, A. Raveh, and M. R. Wertheimer, "Critical ion energy and ion flux in the growth of films by PECVD", J. Vac. Sci. Technol. **A 12**(4), 1360-1364 (1994).

36. O. M. Kuttel, J. E. Klemberg-Sapieha, L. Martinu, and M. R. Wertheimer, "Energy fluxes in mixed microwave-rf plasma", Thin Solid Films **193/194**, 155-163 (1990).

37. Watanabe, M. Shiratani, Y. Kubo, I. Ogawa, and S. Ogi, "Effects of low-frequency modulation on rf discharge chemical vapor deposition", Appl. Phys. Lett. **53**, 1262 (1988).

38. S. Samukawa and T. Mieno, "Pulse-time modulated plasma discharge for highly selective, highly anisotropic and charge-free etching", Plasma Sources Sci. Technol. **5**, 132-138 (1996).

39. L. J. Overzet and J. T. Verdeyen, "Enhancement of the plasma density and deposition rate in rf discharges", Appl. Phys. Lett. **48**(11), 695-697 (1986).

40. N. Ahn, K. Nakamura, and H. Sugai, "Negative ion measurements and etching in a pulsed-power inductively coupled plasma in chlorine", Plasma Sources Sci. Technol. **5**, 139-144 (1996).

41. L. Martinu and M. R. Wertheimer, "Ion assisted thin film growth in dual microwave/radio frequency plasmas", Materials Sci. Forum **140-142**, 405-420 (1993).

42. J. E. Klemberg-Sapieha, L. Martinu, M. R. Wertheimer, P. Gunther, R. Schellin, C. Thielemann, and G. M. Sessler, "Plasma deposition of low-stress electret films for electroacoustic and solar sell applications", J. Vac. Sci. Technol. A **14**(5), 2775-2779 (1996).

43. D. Poitras, P. Leroux, J. E. Klemberg-Sapieha, S. C. Gujrathi, L. Martinu, "Characterization of homogeneous and inhomogeneous Si-based optical coatings deposited in dual-frequency plasma", Opt. Eng. **35**(9), 2693-2699 (1996).

44. A. S. da Silva Sobrinho, M. Latreche, G. Czeremuszkin, J. E. Klemberg-Sapieha, and M. R. Wertheimer, "Transparent barrier coatings on polyethylene terephthalate by single- and dual-frequency PECVD", J. Vac. Sci. Technol. A **16**(6), 3190-3198 (1998).

45. S. Vepřek, "The search for novel, superhard materials", J. Vac. Sci. Technol. A **17**(5), 2401-2420 (1999).

46. U. J. Gibson, "Ion-beam processing of optical thin films", in "Physics of Thin Films: Advances in Research and Development", vol. 13, Eds. M. H. Francombe and J. L. Vossen, (Academic Press, San Diego, CA, 1987) pp. 109-147.

47. K.-H. Muller, "Film growth modification by concurrent ion bombardment: theory and simulation", in Ref. 18, pp.241-278.

48. S. C. Brown, "A Short History of Gaseous Electronics", in "Gaseous Electronics", Eds. M. N. Hirsh and H. J. Oskam, Vol 1, (Academic Press, New York, 1978) Chapter 1, pp. 1-18.

49. F. F. Chen, "Introduction to Plasma Physics", (Plenum Press, New York, 1974).

50. J. R. Roth, "Industrial Plasma Engineering", Vol. 1, (Institute of Physics Publishing, London, 1995).

51. V. A. Godyak, R. B. Piejak, and B. M. Alexandrovich, "Measurements of electron energy distribution in low-pressure rf discharges", *Plasma Sources Sci. Technol.* **1,** 36-58 (1992).

52. S. Vepřek, "Applications of Low Pressure Plasmas in Materials Science: Especially Chemical Vapor Deposition," *Current Topics in Materials Science* **4**(4), 151 (1980).

53. J. van Roosmalen, J. A. G. Baggerman, and S. J. H. Brader, "Dry Etching for VLSI", (Plenum Press, New York, 1991).

54. J. L. Cecchi, "Introduction to Plasma Concepts and Discharge Configurations", in Ref. 9, pp. 14-69.

55. M. A. Lieberman and A. J. Lichtenberg, "Principles of Plasma Discharges and Materials Processing", (Wiley, New York, 1994).

56. F. V. Sears and G. L. Salinger, "Thermodynamics, Kinetic Theory, and Statistical Thermodynamics", (Addison-Wesley, Reading, MA, 1975).

57. V. Phelps, "Cross Sections and Swarm Coefficients for Nitrogen Ions and Neutrals in N_2 and Argon Ions and Neutrals in Ar for Energies from 0.1 eV to 10 keV", *J. Phys. Chem. Ref. Data* **20**(3), 557-573 (1991).

58. V. A. Godyak and N. Sternberg, "Smooth plasma-sheath transition in a hydrodynamic model", *IEEE Trans. Plasma Sci.* **18**, 159-168 (1990).

59. K-U. Riemann, *J. Phys. D: Appl. Phys.* **24**, 493 (1990).

60. A. Manenschijn and W. J. Goedheer, "Angular ion and neutral energy distribution in a collisional rf sheath", J. Appl. Phys. **69**(5), 2923-2930 (1991).

61. J. C. Moreno-Marin, I. Abril, and R. Garcia-Molina, "Radial profile of energetic particles bombarding the substrate in a glow discharge", J. Vac. Sci. Technol. A, **17**(2), 528-534 (1999).

62. A. Metze, D. W. Ernie, and H. J. Oscam, "Application of the physics of plasma sheaths to the modeling of rf plasma reactors", J. Appl. Phys. **60**, 3081 (1986).

63. P. A. Miller and M. E. Riley, "Dynamics of collisionless rf plasma sheath", J. Appl. Phys. **82**(8), 3689-3709 (1997).

64. T. Panagopoulos and D. J. Economou, "Plasma sheath model and ion energy distribution for all radio frequences", J. Appl. Phys. **85**(7), 3435-3443 (1999).

65. J. Ero, Acta Phys. Acad. Sci. Hung. **5**, 391, (1956); J. Ero, Nucl. Instrum. **3**, 303 (1958).

66. P. Benoit-Cattin and L.-C. Bernard, "Anomalies of the energy of positive ions extracted from high-frequency ion sources. A Theoretical Study", J. Appl. Phys. **39**(12), 5723-5726 (1968).

67. J. W. Coburn and E. Kay, "Positive-ion bombardment of substrates in rf diode glow discharge sputtering", J. Appl. Phys. **43**(12), 4965-4971, (1972).

68. J. Liu, G. L. Huppert, and H. H. Sawin, "Ion bombardment in rf plasmas", J. Appl. Phys. **68**(8), 3916-3934 (1990).

69. C. Wild and P. Koidl, "Ion and electron dynamics in the sheath of radio-frequency glow discharges", J. Appl. Phys. **69**(5), 2909-2922 (1991).

70. E. Kawamura, V. Vahedi, M. A. Lieberman, and C. K. Birdsall, "Ion energy distributions in rf sheaths; review, analysis and simulation", Plasma Sources Sci. Technol. **8**(3), Aug99.

71. J. Perrin, "Mass spectrometry of reactive plasmas", in "Plasma Processing of Semiconductors", Ed. P. F. Williams, Kluwer Academic Publishers, Amsterdam, 397-431 (1997).

72. A. D. Kuypers and H. J. Hopman, "Measurement of ion energy distributions at the powered rf electrode in a variable magnetic field", J. Appl. Phys. **67**(3) 1229-1240 (1990).

73. M. A. Sobolewski, J. K. Olthoff, and Y. Wang, "Ion energy distributions and sheath voltages in a radio-frequency-biased, inductively coupled, high-density plasma reactor", J. Appl. Phys. **85**(8), 3966-3975 (1999).

74. H. R. Koenig and L. I. Maissel, "Application of rf discharge to sputtering", IBM J. Res. Dev., **14**, 168-171 (1970).

75. J. S. Logan, "Rf diode sputter etching and deposition", in Handbook of Plasma Processing Technology, Eds. S. M. Rossnagel, J. J. Cuomo, and W. D. Westwood, (Noyes Publications, Park Ridge, 1989) pp. 140-159.

76. D. E. Morton and A. Dinca, "Ion-Assisted Deposition of E-Gun Evaporated ITO Films at Low Substrate Temperatures", 42nd Annual Technical Conference Proceedings, Society of Vacuum Coaters, **250-254** (1999).

77. D. E. Morton and V. Fridman, "Measurement and Correlation of Ion Beam Current Density to Moisture Stability of Oxide Film Stacks Fabricated by Cold Cathode Ion Assisted Deposition", 41nd Annual Technical Conference Proceedings, Society of Vacuum Coaters, **297-301** (1998).

78. B. Singh and P. Denton, "Cold Cathode Ion Beam Source," United States Patent #4 710 283 (Dec. 1, 1987).

79. C. Bohm and J. Perrin, "Retarding-field analyser for measurements of ion energy distributions and secondary electron emission coefficients in low-pressure radio frequency discharges", Rev. Sci. Instrum. **64**(1), 31-44 (1993).

80. U. Kortshagen and M. Zethoff, "Ion energy distribution functions in a planar inductively coupled rf discharge", Plasma Sources Sci. Technol. **4**, 541-550 (1995). We note here that the definition of the ion energy distribution used in this work is different from that usually used in studies of ion energies in the plasma volume [for example see Hopwood et al. J. Vac. Sci. Technol. A8(4), 3103 (1990)]. The difference is in the normalization factor: our IEDF is normalized by the ion flux on the surface, not the ion density in the plasma volume. Consequently, Eq. 5.3 gives

the mean energy that ion brings to the surface (i.e. the parameter which affects surface properties), not the mean ion energy in the volume near the surface.

81. N. J. Taylor, Rev. Sci. Instrum. **40,** 792 (1969).

82. A. Roth, "Vacuum technology", 3rd Ed., Elsevier, Amsterdam, 1990.

83. J. W. Coburn and E. Kay, "Pressure considerations associated with ion sampling from glow discharges", J. Vac. Sci. Technol. **8**(6), 738-743 (1971).

84. J. Janes, "Angular impact energy distributions of argon ions at the powered electrode of a helicon plasma source", J. Vac. Sci. Technol. A **12**(1), 97-105 (1994).

85. J. R. Woodworth, M. E. Riley, D. C. Meister, B. P. Aragon, M. S. Le, and H. Sawin, "Ion energy and angular distributions in inductively coupled radio frequency discharges in argon", J. Appl. Phys., **80**(3), 1304-1311 (1996).

86. J. I. Ulacia F. and J. P. McVittie, "A two-dimentional computer simulation for dry etching using Monte-Carlo techniques", J. Appl. Phys. **65**(4), 1484-1491 (1989).

87. B. E. Thompson, H. H. Sawin, and D. A. Fisher, "Monte-Carlo simulation of ion transport through rf glow-discharge sheaths", J. Appl. Phys. **63**(7), 2241-2251 (1988).

88. Anon., "EQP/EQS analyser operator's manual", Issue B, Hiden Analytical Ltd., Warrlington, England, 1997.

89. Anon., "Hiden technical data sheet", #149, Hiden Analytical Ltd., Warrlington, England, 1998.

90. P. J. Hargis Jr., K. E. Geenberg, P. A. Miller, J. B. Gerardo, J. R. Torczynski, M. E. Riley, G. A. Hebner, J. R. Roberts, J. K. Olthoff, J. R. Whetstone, R. J. Van Brunt, M. A. Sobolewski, H. M. Anderson, M. P. Spichal, J. L. Mock, P. Bletzinger, A. Garscadden, R. A. Gottscho, G. Selwyn, M. Dalvie, J. E. Heidenreich, J. W. Butterbaugh, M. L. Brake, M. L. Passow, J. Pender, A. Lujan, M. E. Elta, D. B. Graves, H. H. Sawin, M. J. Kushner, J. T. Verdeyen, R. Horwath, and T. R. Turner,

"The Gaseous Electronics Conference radio-frequency reference cell: A defined parallel-plate radio-frequency system for experimental and theoretical studies of plasma-processing discharges", Rev. Sci. Instrum. **65**(1), 140-154 (1994).

91. N. Spiliopoulos, D. Mataras, and D. E. Rapakoulias, "Power dissipation and impedance measurements in radio-frequency discharges", J. Vac. Sci. Technol. A **14**(5), 2757-2765 (1996).

92. D. A. Shirley, Phys. Rev. B **5**, 4709 (1972).

93. C. Charles and R.W. Boswell, "Breakdown, steady state and decay regimes in pulsed oxygen helicon diffusion plasmas", J. Appl. Phys., **78**(2), (1995), 766.

94. E.M. Liston, L. Martinu, and M.R. Wertheimer, "Plasma surface modification of polymers for improved adhesion: a critical review", J. Adhesion Sci. Technol., 7(10), 1091 (1993).

95. M.R. Wertheimer and L. Martinu, "Plasma sources for the treatment of polymers", chapter E3.0 in "Handbook of Thin Film Process Technology", (IOP, Bristol, 1996) pp. 1-38.

96. M.R. Wertheimer, L. Martinu and M. Moisan, "Microwave and dual-frequency plasma processing", in "Plasma Processing of Polymers", R. d'Agostino et al., eds., Kluwer Academic Publishers, Dordrecht, 1997, p.101.

97. P. Reinke, S. Bureau, J.E. Klemberg-Sapieha, and L. Martinu, "Ion energy distributions in dual- and single-mode microwave/radiofrequency plasma", J. Appl. Phys., **78** (1995) 260.

98. S. Samukawa, "Pulse-time-modulated electron cyclotron resonance plasma etching for highly selective, highly anisotropic, and notch-free polycrystalline silicon patterning", Appl. Phys. Lett., **64**, 3398 (1994).

99. A.A. Howling, L. Sansonnes, J.-L. Dorier, and Ch. Hollenstein, "Time-resolved measurements of highly polymerized negative ions in radio frequency silane plasma deposition experiments", J. Appl. Phys., **75**(3) 1340 (1994).

100. J.P. Booth, G. Cunge, N. Sadeghi, and R.W. Boswell, "The transition from symmetric to asymmetric discharges in pulsed 13.56 MHz capacitively coupled plasmas" J. Appl. Phys. **82**(2), 552-560, (1997).

101. M. Zeuner, H. Neumann, and J. Meichsner, "Ion energy distribution in oxygen and argon in a pulsed mode RF discharge", Vacuum, **48**(5), 443-447 (1997).

102. G.A. Hebner and C.B. Fleddermann, "Characterisation of pulse-modulated inductively coupled plasmas in argon and chlorine", J. Appl. Phys., **82**(6), 2814-2821, (1997).

103. T. Mieno and S. Samukawa, "Generation and excitation characteristics of negative ions in pulse-time-modulated electron cyclotron resonance chlorine plasma", Plasma Sources Sci. Techol., **6**, 398-404, (1997).

104. S. Ashida, M.R. Shim, and M.A. Lieberman, "Measurements of pulsed-power modulated argon plasmas in an inductively coupled plasma source", J. Vac. Sci. Technol. A, **14**(2), 391-397, (1996).

105. M.A. Lieberman and S. Ashida, "Global models of pulse-power-modulated high-density, low-pressure discharges", Plasma Sources Sci. Techol., **5**, 145-148 (1996).

106. P. Reinke, O. Zabeida, B. Andreani, S. Bureau, and L. Martinu, "Ion energy distribution functions in microwave and radio frequency plasmas", Proceedings of 12th International Symposium on Plasma Chemistry, vol. **1**, 499 (1995).

107. O. Zabeida, J.E. Klemberg-Sapieha, and L. Martinu, "Effect of pulse mode on the plasma characteristics and on the treatment of polymers", Proceedings of 41st SVC meeting (1998) 336-341.

108. M.K. Shi, A. Selmani, L. Martinu, E. Sacher, M.R. Wertheimer, and A. Yelon, "Fluoropolymer surface modification for enhanced metal adhesion" J. Adh. Sci. Technol., **8** (1994) 1129-1141.

109. J.E. Klemberg-Sapieha, O.M. Küttel, L. Martinu, and M.R. Wertheimer, "Dual-frequency N_2 and NH_3 plasma modification of polyethylene and polyimide", J. Vac. Sci. Technol. A, **9** (6), 2975-2981 (1991).

110. R. Boswell and D. Vender, "Simulation of pulsed electropositive and electronegative plasmas", IEEE Trans. Plasma Sci., **19**(2), 141-143 (1991).

111. A. Hallil, O. Zabeida, M. R. Wertheimer, and L. Martinu, "Mass-resolved ion energy distributions in continuous dual mode microwave/radio frequency plasmas in argon and nitrogen", J. Vac. Sci. Technol., submitted in December 1999.

112. J. K. Olthoff, R. J. Van Brunt, S. B. Radovanov, J. A. Rees, and R. Surowiec, J. Appl. Phys. **75**, 115 (1994).

113. O. Auciello and R. Kelly, eds., "Ion Bombardment Modification of Surfaces", (Elsevier, Amsterdam, 1984).

114. O. Zabeida and L. Martinu, "Ion energy distributions in pulsed large area microwave plasma", J. Appl. Phys. **85**(9), 6366-6372, (1999). (Section 5.2 of this thesis).

115. K. A. Buckle, K. Pastor, C. Constantine, and D. Johnson, "Parametric evaluation of electron cyclotron resonance deposited SiO2 using a multicusp plasma applicator", J. Vac. Sci. Technol. B **10**(3), 1133- 1138 (1992).

116. H. Shirai, J. Hanna, and I. Shimizu, Jpn. J. Appl. Phys. 1 **30**, L679 (1991).

117. R. Etemadi, C. Godet, J. Perrin, B. Drevillon, J. Huc, J. Y. Parey, J. C. Rostaing, and F. Coeuret, "Dual-plasma reactor for low temperature deposition of wide band-gap silicon alloys", J. Vac. Sci. Technol. A **15**, 320 (1997).

118. Y. Watanabe, M. Shiratani, Y. Kubo, I. Ogawa, and S. Ogi, "Effects of low-frequency modulation on rf discharge chemical vapor deposition", Appl. Phys. Lett. **53**(14), 1263-1265 (1988).

119. J. E. Klemberg-Sapieha, O. M. Küttel, L. Martinu, and M. R. Wertheimer, Thin Solid Films **193/194**, 965, (1990).

120. B. Lamontagne, O. M. Küttel, and M. R. Wertheimer, Can. J. Phys. **69**, 202 (1991).

121. A. Hallil, O. Zabeida, J. E. Klemberg-Sapieha, M. R. Wertheimer, and L. Martinu, *Mass-resolved ion energy distributions in dual-mode microwave/radio frequency plasma*, 42nd Annual Technical Conference Proceedings (Society of Vacuum Coaters, Chicago), (1999), p. 311-315.

122. W. H. Hayward, "Introduction in Radio Frequency Design", (Prentice-Hall, Englewood Cliffs NJ, 1981), p. 138.

123. P.R. Denton, J. Lee and A. Musset, "A large area cold cathode ion source for use in vacuum chambers", Proc. 28 Ann. Tech. Meeting (Society of Vacuum Coaters, Albuquerque, 1985) 53-68.

124. J.E. Klemberg-Sapieha, D. Poitras, L. Martinu, N.L.S. Yamasaki, and C.W. Lantman, "Effect of interface on the characteristics of functional films deposited on polycarbonate in dual-frequency plasma", J. Vac. Sci. Technol. A **15**, 985-991 (1997).

125. Unpublished results from our laboratory.

126. R. Rujkoran, L. S. Hsu, and C. Y. She, "Crystallisation of titania films by thermal heating", NBS Special Publication **727**, 253-261 (1985).

Appendix A. Choice of the ion mobility

We have used the data for the drift velocity, W_+, of Ar^+ ions in argon gas (Ref. 57) to obtain the ion mobility and the thickness of highly collisional dc sheath with the potential drop of V_0 =100 V. The results are presented in Table A.1. Several values of μ_i and s, corresponding to different values of the electric field, E, have been calculated for each plasma condition. The values of s, for which corresponding E is close to V_0/s are then chosen and used in Table 3.2.

Table A.1. Ion mobility for the different plasma conditions.

n_s 10^9 cm^{-3}	p mTorr	n 10^{21} m^{-3}	E/n $10^{-21}Vm^2$	W_+ m/c	E V/cm	μ_i m^2/Vc	s mm	V_0/s V/cm
6.1	20	0.64	30000	10730	192	0.56	3.1	323
			50000	14400	**320**	0.45	2.9	**347**
			100000	21600	640	0.34	2.6	380
6.1	100	3.22	10000	5780	320	0.18	2.2	454
			20000	8550	640	0.13	2.0	506
0.6	20	0.64	10000	5780	64	0.9	8.4	118
			20000	8550	**128**	0.67	7.4	**135**
			30000	10730	192	0.56	6.9	143
0.6	100	3.22	5000	3960	**160**	0.25	6.1	**165**

Note: Ar^+ ion with an energy of 1 eV moves at a speed ~2200 m/s, hence the W_+ values (W_+<14400 m/s) correspond to $E_i < 3$ eV.